

The APM Galaxy Survey III: An Analysis of Systematic Errors in the Angular Correlation Function and Cosmological Implications

S.J. Maddox¹, G. Efstathiou, and W.J. Sutherland

Department of Physics,
Nuclear and Astrophysics Laboratory,
Keble Road, Oxford,
OX1 3RH, England

ABSTRACT

We present measurements of the angular two-point galaxy correlation function, $w(\theta)$, from the APM Galaxy Survey. The performance of various estimators of $w(\theta)$ is assessed by analyzing simulated galaxy catalogues. We use these tests, and analytic arguments, to select estimators which are least affected by large-scale gradients in the galaxy counts correlated with the survey boundaries. An error analysis of the plate matching procedure in the APM Galaxy Survey shows that residual plate-to-plate errors do not bias our estimates of $w(\theta)$ by more than $\sim 1 \times 10^{-3}$. A direct comparison between our photometry and external CCD photometry of over 13,000 galaxies from the Las Campanas Deep Redshift Survey shows that the *rms* error in the APM plate zero points lies in the range 0.04–0.05 magnitudes, in agreement with our previous estimates. The comparison with the CCD photometry sets tight limits on any variation of the magnitude scale with right ascension. We find no evidence for any systematic errors in the survey correlated with the date of scanning and exposure. We estimate the effects on $w(\theta)$ of atmospheric extinction and obscuration by dust in our Galaxy and conclude that these are negligible. There is no evidence for any correlations between the errors in the survey and limiting magnitude except at the faintest magnitudes of the survey, $b_J > 20$, where star-galaxy classification begins to break down introducing plate-to-plate variations in the completeness of the survey. We use our best estimates of the systematic errors in the survey to calculate corrected estimates of $w(\theta)$. Deep redshift surveys are used to determine the selection function of the APM Galaxy Survey, *i.e.* the probability that a galaxy at redshift z is included in the sample at a given magnitude limit. The selection function is applied in Limber's equation to compute how $w(\theta)$ scales as a function of limiting magnitude. Our estimates of $w(\theta)$ are in excellent agreement with the scaling relation, providing further evidence that systematic errors in the APM survey are small. We explicitly remove large-scale structure by applying filters to the APM galaxy maps and conclude that there is still strong evidence for more clustering at large scales than predicted by the standard scale-invariant cold dark matter (CDM) model. We compare the APM $w(\theta)$ and the three dimensional power spectrum derived by inverting $w(\theta)$, with the predictions of scale-invariant CDM models. We show that the observations require $\Gamma = \Omega_0 h$ in the range 0.2–0.3 and are incompatible with the value $\Gamma = 0.5$ of the standard CDM model.

¹ Present address: The Royal Greenwich Observatory, Madingley Road, Cambridge, CB3 0EZ, UK

1. Introduction

The APM Galaxy Survey is a machine measured survey of over 2 million galaxies in the southern sky to a magnitude limit $b_J = 20.5$. It was constructed by scanning 185 UK Schmidt telescope (UKST) survey plates, covering 4300 square degrees, with the Automatic Plate Measuring (APM) machine at Cambridge. The construction of the survey and the star-galaxy separation algorithm have been described in Paper I of this series (Maddox *et al.* 1990a). The photometric accuracy and plate matching algorithm have been described in Paper II (Maddox *et al.* 1990b).

One of the main aims in constructing the APM Galaxy Survey has been to determine the two-point galaxy correlation function $\xi(r)$, or equivalently the power spectrum $P(k)$ (see Baugh and Efstathiou 1993, 1994), at large spatial scales. The two-point spatial correlation function is the Fourier transform of the power spectrum

$$\xi(r) = \frac{V}{(2\pi)^3} \int P(k) e^{-i\mathbf{k}\cdot\mathbf{r}} d^3k, \quad (1)$$

where for a point process of mean density \bar{n} ,

$$P(k) = \langle |\delta_{\mathbf{k}}|^2 \rangle - \frac{1}{\bar{n}V}, \quad (2)$$

and $\delta_{\mathbf{k}}$ is the Fourier transform

$$\delta_{\mathbf{k}} = \frac{1}{\bar{n}V} \sum_i e^{-i\mathbf{k}\cdot\mathbf{r}_i}, \quad (3)$$

where the sum in equation (3) extends over all points located at positions \mathbf{r}_i (see Peebles 1980 §41). In equations (1)-(3) we assume that the distribution is periodic in a large box of volume V . For a Gaussian random field, phases of different Fourier modes are uncorrelated (*ie* $\langle \delta_{\mathbf{k}} \delta_{\mathbf{k}'} \rangle = P(\mathbf{k}) \delta(\mathbf{k} - \mathbf{k}')$) and so the two-point correlation function provides a *complete* statistical description of the density field. The two-point galaxy correlation function is, therefore, an especially important measure of large-scale structure, particularly if the galaxy distribution can be described by a Gaussian random field, as expected in many models of the origin of structure (*e.g.* theories of inflation in the early universe, Kolb and Turner 1990). Even if the fluctuations are non-Gaussian, the two-point correlation function can provide an important test of theoretical models and is the most easily measured of a hierarchy of N -point correlation functions (see Peebles 1980 §34-35).

The three dimensional two-point function, $\xi(r)$, can be inferred from the angular two-point function, $w(\theta)$, via Limber's formula (Limber 1954, equation 31 below). Analyses of

several samples of galaxies (*e.g.* Peebles 1974, see also Section 4.1) have shown that at small angles the angular correlation function is a power law,

$$w(\theta) = A\theta^{1-\gamma}, \quad (4)$$

where $\gamma \approx 1.7$, and A depends on the sample depth. In an earlier paper, we presented measurements of $w(\theta)$ from the APM Galaxy Survey (Maddox *et al.* 1990c) which show that $w(\theta)$ steepens and lies below the extrapolation of the power law (4) at large angles. At a magnitude limit of $b_J = 20$, the break occurs at an angle $\theta \approx 2^\circ$, corresponding to a physical scale of $15 h^{-1}\text{Mpc}^*$ at the median depth of the survey. However, even though we observe a break in $w(\theta)$, our results provide strong evidence for more clustering at large scales than predicted by the standard $\Omega_0 = 1$ scale-invariant cold dark matter model (see Efstathiou 1995a for a recent review and Section 5 of this paper).

Measurements of clustering on scales $\gtrsim 10 h^{-1}\text{Mpc}$ are extremely difficult because $w(\theta)$ is small and hence sensitive to non-uniformities in the galaxy catalogue. For example, the results from the APM Galaxy Survey disagree with Groth and Peebles (1977; hereafter GP77) determination of $w(\theta)$ from the Lick sample (Shane and Wirtanen 1967, Seldner *et al.* 1977), which is the largest galaxy catalogue comparable to the APM Galaxy Survey. GP77 found a much sharper break from the power law on scales $\theta \gtrsim 3^\circ$ (see Section 4.2.3). The APM angular correlation function is in better agreement with that measured from the Edinburgh-Durham Southern Galaxy Catalogue, a machine measured sample similar to the APM Survey but covering about one third of the area of sky (Collins *et al.* 1992, Nichol & Collins 1993, see Section 4.2.2). It is unfortunate that the results from the machine measured catalogues and the Lick survey disagree, for it implies that one or more samples are affected by systematic errors. The uniformity of the Lick catalogue has been a subject of some controversy (see *e.g.* Geller *et al.* 1984, de Lapparent *et al.* 1986, Groth and Peebles 1986a,b), but because it was constructed by eye, and the information is extremely limited (consisting of counts of galaxies in $10' \times 10'$ cells), only a restricted set of checks can be applied to test its uniformity. In contrast, the APM Galaxy Survey was designed specifically to measure $w(\theta)$ at large scales and has several important advantages over the Lick survey that allow more stringent controls of systematic errors:

- (a) The APM Galaxy Survey gives positions, magnitudes and profile information for each image. The photometry on neighbouring plates in the APM Survey is matched by identifying individual galaxies in the plate overlap regions. In contrast, plates in the

* Throughout this paper h denotes the Hubble constant H_0 in units of $100\text{kms}^{-1}\text{Mpc}^{-1}$; Ω_0 is the mean mean mass density of the universe at the present epoch divided by the critical density of the Einstein de-Sitter model.

Lick survey are matched by comparing the galaxy counts on overlapping plates, which are strongly affected by galaxy clustering. The plate matching errors in the APM Galaxy Survey are consequently smaller than those for the Lick survey.

- (b) The magnitudes of individual galaxies in the APM Survey can be compared with CCD magnitudes to provide checks of the photometric accuracy.
- (c) The APM Survey covers a large area of sky and contains over 2 million galaxies. It can therefore be divided into subsamples to provide empirical estimates of sampling fluctuations and systematic errors. Although the Lick catalogue contains 1 million galaxies, only about half of these are at sufficiently high Galactic latitude to be useful in studies of the galaxy distribution.
- (d) The magnitude data in the APM catalogue allow us to apply the scaling test derived from Limber's equation (*e.g.* GP77) to check whether the angular correlation function scales with limiting magnitude as expected if $w(\theta)$ is measuring real structure in the galaxy distribution.

In addition, the APM Survey contains other data such as surface brightness and position angles, which enable a variety of other analyses to be carried out, *e.g.* analyses of galaxy ellipticities, large-scale alignments *etc* (Lambas, Maddox and Loveday 1992). Higher order correlations from the APM Survey are discussed by Gastanaga & Frieman (1994) and Szapudi *et al.* (1995). Catalogues of rich clusters of galaxies selected from the APM Survey, and the spatial distribution of APM clusters, are described in Papers IV and V of this series (Dalton *et al.* 1994a, 1995) and by Dalton *et al.* (1992, 1994b).

In this paper, we present measurements of $w(\theta)$ from the APM Galaxy Survey and an analysis of systematic errors and how these affect $w(\theta)$. In Section 2 and the Appendix, we discuss various estimators for $w(\theta)$ which we have tested on simulated galaxy distributions. We then present measurements of $w(\theta)$ from the APM Survey. Section 3 gives a detailed discussion of systematic errors in the survey. We compare our magnitudes to independent CCD photometry and address the points raised by Fong *et al.* (1992) concerning large scale gradients in the APM survey. We also present estimates of the angular correlation functions after correcting for systematic errors. In Section 4 we use deep redshift surveys to determine the distribution in redshift of APM galaxies as a function of limiting magnitude and these are used in Limber's equation to test the scaling of $w(\theta)$ with depth. We discuss briefly how our results compare with those from other catalogues and we investigate the effects of filtering our galaxy maps by subtracting smooth fits to the galaxy distribution. Some cosmological implications of our results are discussed in Section 5. Our main conclusions are summarized in Section 6.

2 Measurements of $w(\theta)$

2.1 Estimators of the correlation function.

Several methods of estimating the angular correlation function from galaxy surveys have been discussed in the literature, and in Appendix A we describe tests of various estimators on simulated galaxy catalogues. The results of these tests led us to choose two estimators to measure $w(\theta)$ for the APM Galaxy Survey.

The first of these is defined by the equation

$$w(\theta) = \frac{\langle N_i N_j \rangle}{\langle N_i \rangle \langle N_j \rangle} - 1, \quad (5)$$

where N_i is the count of galaxies in cell i and the angle brackets denote averages over pairs of cells at separation θ . As explained in Appendix A, this estimator is unaffected by first-order errors caused by density variations correlated with the survey boundaries. In Appendix A we define an estimator of $w(\theta)$ based of the Fourier transform of the two-dimensional power-spectrum of the survey which has similar statistical properties to the estimator (5) (see Appendix A, Section A3). However, although the Fourier transform estimator offers a considerable time saving over equation (5), it does not provide separate inter- and intra-plate estimates of $w(\theta)$, which are useful as a check on systematic errors in the survey (*cf* Groth and Peebles 1986a and Section 3.1.2). We have therefore used equation (5) to calculate the large-angle correlation functions presented in this Section.

The second estimator that we have used is based on a direct count of galaxy pairs. For this estimator, we count pairs of galaxies on each field taking into account edges and holes in the survey (see Plate 2 of Paper II) by cross correlating the galaxy distribution with a catalogue of random points within the same field boundaries. The estimate of $w(\theta)$ is defined by

$$w(\theta) = 2F \frac{DD}{DR} - 1, \quad (6)$$

where DD is the number of distinct galaxy-galaxy pairs with separations in the range $\theta \pm \delta\theta$, DR is the number of galaxy-random pairs, and the density of random points is set to F times the number of galaxies. The estimator of equation (6) is easy to evaluate and does not require gridding of the data. It is, however, subject to first order errors in the galaxy density contrast (Hamilton, 1993a; Appendix A), but this is not a problem because we use it to estimate $w(\theta)$ on small angular scales where the amplitude is high, and we average over a large number of fields so that first order errors cancel. In fact, over the range $0.09^\circ < \theta < 0.9^\circ$ the differences between the $w(\theta)$ estimates from equations (5) and

(6) are found to be negligible. Generalizations of equation (6) that have similar statistical properties to equation (5) are discussed by Hewett (1982), Hamilton (1993a) and Landy and Szalay (1993).

We have applied equation (5) to estimate $w(\theta)$ over the angular range $0.12^\circ < \theta < 30^\circ$ from several equal area maps of the galaxy distribution with cell sizes varying from $0.12^\circ \times 0.12^\circ$ to $0.9^\circ \times 0.9^\circ$. On smaller angular scales, $0.09^\circ < \theta < 0.9^\circ$, we apply equation (5) to cell counts on each Schmidt field. For very small separations, $0.0009^\circ < \theta < 0.9^\circ$ we estimate $w(\theta)$ from equation (6).

As discussed in the following subsection and in Appendix A, $w(\theta)$ is biased low if the mean density for each Schmidt field is estimated from the number of galaxies within it. This bias can be eliminated by using all fields to estimate the mean density, even though the pair counts are computed separately for each field. On scales $0.1^\circ < \theta < 0.5^\circ$, the mean of these single plate estimates agrees well with $w(\theta)$ measured from the full map (see Section 2.3).

We apply a correction to each estimate of $w(\theta)$ to account for the residual contamination of the galaxy sample by non-galaxy images. Since the large majority of contaminating images are stars or star-star mergers, it is a good approximation to assume that they are uncorrelated. There is a $\sim 10\%$ difference between the density of contaminating objects at the Galactic pole compared to low Galactic latitude ($|b| \lesssim 40^\circ$), but this gradient has very little effect on $w(\theta)$ (see Section 3.4.3). We thus simply multiply the $w(\theta)$ estimates by $1/(1-f)^2$ where f is the contamination fraction estimated from the visual classifications in Table 5 of Paper I.

As discussed in Paper I, the APM Galaxy Survey has a high level of completeness. However, most of the galaxies missing from our survey will be at the extremes of high and low surface brightness, and so incompleteness may lead to a small error in $w(\theta)$ if these galaxies are clustered differently to normal galaxies. Variations in the completeness from plate-to-plate will cause an error in $w(\theta)$ similar to magnitude matching errors: this small effect is discussed in Section 3.1.1.

2.2 Integral constraints and single plate measurements of $w(\theta)$

Figure 1 shows the average $w(\theta)$ estimated from equation (6) using galaxies in the magnitude range $17 \leq b_J \leq 20.0$ within the central $4.64^\circ \times 4.64^\circ$ area on each of 185 Schmidt plates. In calculating DD in equation (6) we count galaxy pairs only if both galaxies are on the same plate. The filled circles in Figure 1 show estimates of $w(\theta)$ in which the mean surface density in each single plate estimate is determined from the the number of galaxies within each field (*i.e.* rather than using a global estimate of the mean density derived from the entire survey). This method of estimating $w(\theta)$ is therefore similar

to that applied by other investigators to single Schmidt fields (*e.g.* Shanks *et al.* 1980, Hewett 1982). We use only the centre of each field because the errors in the field corrections and galaxy classification become larger near the edges (see Papers I and II for quantitative details).

At angular scales $\theta < 14''$, corresponding physical separation $\lesssim 20\text{kpc}$, the amplitude of $w(\theta)$ decreases with decreasing pair separation. This is because close pairs of galaxies are often recorded as one object by the APM machine (see Paper I) leading to an underestimate of $w(\theta)$ at small angular separations.

Over the angular range $0.01^\circ < \theta < 0.1^\circ$, the filled circles in Figure 1 approximately follow a power law. The results for each plate have been fitted to a power law $w(\theta) = A\theta^{1-\gamma}$ by least-squares. After correcting for the dilution of clustering caused by the 6% residual contamination by stellar mergers and misclassifications, the mean and standard deviation of γ and A averaged over the 185 fields are

$$\left. \begin{array}{l} \gamma = 1.72 \pm 0.01 \\ A = 0.023 \pm 0.001 \end{array} \right\} \text{ for } 0.01^\circ < \theta < 0.1^\circ.$$

where the amplitude A is given in units in which θ is in degrees. It is evident that the filled circles in Figure 1 fall below the extrapolation of a power-law with $\gamma = 1.7$ on scales $\theta > 0.5^\circ$. However, this is not a real feature of the galaxy distribution. As we will now demonstrate, estimates of $w(\theta)$ from individual Schmidt plates are biased low if the mean density is determined from the galaxy counts within each field. We can estimate the bias as follows (see also the Appendix). The net galaxy overdensity on each field is

$$\bar{\delta} = \frac{\mathcal{N} - \overline{\mathcal{N}}}{\overline{\mathcal{N}}}, \quad (7)$$

where $\overline{\mathcal{N}}$ is the true mean surface density and \mathcal{N} is the surface density measured on each field. The expectation value of $\bar{\delta}$ is zero and the variance is given by an integral over the two-point correlation function,

$$\langle \bar{\delta} \rangle = 0, \quad (8a)$$

$$\langle \bar{\delta}^2 \rangle = \frac{1}{\overline{\mathcal{N}}\Omega} + \frac{1}{\Omega^2} \int \int_{\Omega} w(\theta_{12}) d\Omega_1 d\Omega_2, \quad (8b)$$

(Peebles 1980 §36), where Ω is the solid angle of the field. If \mathcal{N} is used as a measure of the mean density, the estimate of $w(\theta)$ obtained by averaging over many fields, $w^e(\theta)$, will be biased low by

$$\langle w^e(\theta) \rangle \approx w(\theta) - \langle \bar{\delta}^2 \rangle, \quad (9)$$

We show in Appendix A that the precise form of the bias depends on the particular estimator that is used to measure $w(\theta)$, but equation (9) is a good approximation for all of the estimators considered in this paper if the angular separation θ is small in comparison to the size of a survey field.

An equivalent result to equation (9) can be derived by considering the total number of pairs that are counted on a single plate. If the total number of galaxies on a particular field is N , the total number of pairs must be $N(N - 1)$. Thus, the estimator $w^e(\theta)$ satisfies a relation of the form

$$\int \int_{\Omega} w^e(\theta_{12}) d\Omega_1 d\Omega_2 \approx 0, \quad (10)$$

(GP77) where the integral extends over the area of a single field. The bias in $w(\theta)$ (equation 9) thus arises because the estimator is subject to an integral constraint.

We can estimate $\langle \bar{\delta}^2 \rangle$ directly from the variance in field number counts. For galaxies in the magnitude range $17 \leq b_J \leq 20$, we find $\bar{\delta}^2 = 1.6 \times 10^{-2}$ at $b_J = 20$. The variance caused by plate matching errors accounts for $\approx 1.6 \times 10^{-3}$ (see Paper II and Section 3.1) and so the variance attributable to real galaxy clustering is 1.4×10^{-2} . The mean angular correlation function, after adding this constant is shown by the stars in Figure 1. The amplitude is increased and the mean slope of $w(\theta)$ becomes slightly shallower. The mean parameters of least squares fits to $w(\theta)$ over the angular range $0.01^\circ < \theta < 0.1^\circ$ are

$$\left. \begin{array}{l} \gamma = 1.679 \pm 0.01 \\ A = 0.0282 \pm 0.0012 \end{array} \right\} \text{ for } 0.01^\circ < \theta < 0.1^\circ. \quad (11)$$

As before the amplitude has been corrected to account for the residual stellar contamination. Adding the constant $\bar{\delta}^2$ eliminates the sharp break in $w(\theta)$ at $\theta \sim 0.2^\circ$ and brings the estimates into good agreement with the results obtained using the global mean to normalize the estimator of equation (6) (shown by the open circles in Figure 1). This analysis of bias in estimators of $w(\theta)$ from single Schmidt plates agrees with results from Monte Carlo simulations described in Appendix A. Hewett (1982) has also pointed out that the integral constraint will introduce an artificially sharp cutoff in estimates of $w(\theta)$ from single Schmidt plates and inferred that there must be significant correlations on pair separations of at least $10 h^{-1} \text{Mpc}$ to explain the observed scatter in single plate estimates of $w(\theta)$. Our results disagree with those of Shanks *et al.* (1980) and Stevenson *et al.* (1985) who analyzed clustering on single UKSTU fields limited at $b_J = 20$ and concluded that the break in $w(\theta)$ from an power law at $\theta \approx 0.3^\circ$ is attributable to a real feature of the galaxy distribution.

In summary, the results of this subsection show that the integral constraint introduces an artificial cut-off in the estimates of $w(\theta)$ determined from single Schmidt fields. The

bias in $w(\theta)$ depends on the variance in the galaxy counts on the scale of a Schmidt plate. The high photometric accuracy of the APM survey allows us to correct for the integral constraint bias bringing the single plate estimates of $w(\theta)$ into excellent agreement with those determined by using a global estimate of the mean galaxy surface density.

2.3 Measurements of $w(\theta)$ from galaxy density maps.

To estimate $w(\theta)$ on angular scales $\gtrsim 0.1^\circ$, we apply equation (5) to maps of the galaxy surface density. The maps were constructed by counting the number of galaxies in each $0.23^\circ \times 0.23^\circ$ cell of an equal area projection centred on the South Galactic pole. This produces a 512 square array covering a 120° patch of sky. Cells containing holes in the survey (areas near bright stars, globular clusters and calibration spots) and those outside the survey area were flagged and not used in the analysis. Figure 2 shows $w(\theta)$ for galaxies with $17 < b_J < 20$ computed from the whole survey area. We have estimated $w(\theta)$ from maps with cell sizes different by factors of 0.5, 2, and 4, from those in the 512×512 map and find essentially perfect agreement between the various estimates.

We have also estimated $w(\theta)$ separately for each of four zones containing 45, 45, 46 and 49 plates corresponding roughly to equally spaced strips in right ascension.* The mean of these four estimates is less sensitive to any large-scale gradient in the survey and the scatter between the estimates provides a realistic measure of the sampling errors in $w(\theta)$. The solid line in Figures 2a and 2b show $w(\theta)$ measured using the full survey area and the open circles show the mean of $w(\theta)$ in each of the four zones, with 1σ error bars computed from the scatter between the zones. The full area estimate is not significantly different from the average over the four zones. This demonstrates that gradients in the survey on scales comparable to the size of a single zone do not significantly affect our determination of $w(\theta)$. The solid points in Figure 2 show the mean of the single plate estimates described in Section 2.2 where we used the global mean surface \bar{N} to normalize the pair counts. The estimates of $w(\theta)$ from the maps are in excellent agreement with the single plate pair count estimates.

After correcting for the residual contamination by mergers, the mean of least squares fits of a power law to $w(\theta)$ between $\theta = 0.01^\circ$ and $\theta = 1^\circ$ in each zone gives

$$\left. \begin{aligned} \gamma &= 1.699 \pm 0.032, \\ A &= 0.0284 \pm 0.0029 \end{aligned} \right\} \text{ for } 0.01^\circ < \theta < 1^\circ. \quad (12)$$

* We also computed $w(\theta)$ in four different zones, where we divided the survey in half in both right ascension and declination. The mean $w(\theta)$ and the zone-to-zone scatter from these zones were found to similar to those for the four zones discussed in the main body of the text.

The quoted errors are from the variance in the mean of the four zones. At larger angles the slope of $w(\theta)$ gradually steepens. If we fit a power law between $0.07^\circ < \theta < 0.9^\circ$, i.e. similar physical scales as used by GP77, we obtain a slope of -0.734 , in agreement with their value of -0.741 ± 0.035 . The break at $\sim 3^\circ$ is extremely significant given the scatter between zones. In Figure 2b we plot $w(\theta)$ on a linear scale showing that the estimates are very close to zero (to within $\sim 5 \times 10^{-4}$) for $\theta \gtrsim 6^\circ$.

As described in Section 3.1, it is possible to correct these estimates of $w(\theta)$ for residual plate-to-plate errors in magnitude and classification by subtracting the correlation function of the expected errors. The estimates in Figures 1 and 2 have not been corrected for these errors, but as we will show in Section 3, we estimate that the errors on $w(\theta)$ are $\lesssim 2 \times 10^{-3}$ at small angles, and decreases rapidly at angles $\gtrsim 1^\circ$. Since this is much smaller than the amplitude of $w(\theta)$ even in the region near the break at $\sim 3^\circ$, we believe that our results are not significantly affected by errors in the survey. This point is so important for the interpretation of our results that we devote Section 3 of this paper to a lengthy analysis of systematic errors in the survey before we present corrected estimates of $w(\theta)$.

2.4 Variation of $w(\theta)$ with magnitude

The variation of $w(\theta)$ as a function of magnitude allows us to check that the angular correlation functions measure intrinsic clustering rather than systematic errors. If photometric errors and intervening obscuration are negligible, $w(\theta)$ is determined by the projection of the three-dimensional two point correlation function $\xi(r)$ via Limber's equation (equation 31), and hence $w(\theta)$ should obey a scaling relation as the depth of the survey is changed (Peebles 1980 §50 and Section 4.1.1 equation 33). To test if the correlation function scales as predicted, we evaluated $w(\theta)$ for each of six *disjoint* magnitude slices between $b_J = 17$ and 20.5. The magnitude slices are defined using uncalibrated APM magnitudes, and so are not exactly 0.5 magnitudes wide. The exact magnitude ranges in the calibrated b_J system are listed in Table 4 (Section 3.5) and in the Figures.

We have limited this analysis to the central 120 plates of our survey which lie at Galactic latitudes $b \lesssim -50^\circ$. At such high latitudes no significant errors are introduced by uncertainties in Galactic absorption or from the increase in the numbers of merged stellar images at low galactic latitudes (see Sections 3.4.1 and 3.4.3). The results are shown in Figure 3. Qualitatively, the behaviour is as expected: at brighter magnitudes the amplitude of $w(\theta)$ is higher and the break from a power law occurs at larger angles. In Section 4.1 we quantify the expected shifts by evaluating Limber's equation using empirical estimates of the survey selection function derived from deep redshift surveys.

3. Estimates of Systematic Errors in $w(\theta)$

In this Section we discuss several sources of systematic error which could in principle affect the shape of $w(\theta)$. Errors in the APM Survey could be caused by:

- [1] Variations in the APM scanning procedure.
- [2] Variations in plate emulsion sensitivity.
- [3] Atmospheric variations.
- [4] Galactic obscuration
- [5] Intergalactic dust.
- [6] Stellar contamination.

Sources 1, 2 and 3 introduce plate dependent variations which should be removed by the field corrections and plate matching procedure described in Paper II. Sources 3 - 6 could introduce gradients and features in the galaxy distribution that are continuous across plate boundaries and so would not be removed by the plate matching algorithm.

In the following subsections we describe various tests which we have applied to check the effects of these errors. In Section 3.1 we consider the effects of residual errors in the photometry and galaxy selection by analyzing various models for the errors. In Section 3.2, we test the photometric accuracy of the survey by comparing the APM photometry with independent CCD photometry of large numbers of galaxies. We test for errors correlated with exposure and scanning date in Section 3.3, and for gradients associated with extinction and stellar contamination in Section 3.4. The dependence of systematic errors with apparent magnitude is discussed in Section 3.5.

3.1 Models of residual photometric errors and variations in completeness.

Magnitude errors and variations in star-galaxy classification introduce errors in the observed number of galaxies as a function of position in the survey leading to errors in the measured correlation function. In most of the following discussion we combine both sources of error and consider a single overall error in the number of galaxies at each position on the sky. There are two distinct components to each of the errors: 1) variations across individual Schmidt plates, which we term ‘field effects’; and 2) differences between one plate and the next, which we call ‘plate matching errors’.

Several uncontrollable factors cause the sensitivity of a Schmidt plate to vary as a function of position, and so there are variations in the measured magnitudes as a function of position over each plate. The shape and amplitude of the variations are different for

each plate and, as described in Section 2 of Paper II, we correct the magnitudes using a two-dimensional correction function determined individually for each plate. Although the corrections precisely remove the errors when averaged over all plates, any individual plate is likely to have small residual field effects. This means that each edge of a plate may have systematic errors relative to the plate centre, and relative to the other edges.

The parameters used for star-galaxy separation also show variations across each plate, and so are subject to similar residual field effects. These errors will introduce variations in the completeness of the galaxy sample, and also in the contaminating fraction of non-galaxy images (mainly blended star images). We refer to these errors as galaxy counting errors.

The variations in emulsion, observing conditions and measurement parameters introduce differences in the photometry and completeness of each plate. For both the photometry and star-galaxy separation we have reduced these plate-to-plate variations by applying corrections to each plate so that the differences between measurements on neighbouring plate overlaps are minimized. Any errors in the overlap offsets produce plate-to-plate matching errors which are correlated, and so they propagate across the grid of plates in a random walk, introducing low-amplitude large-scale correlations in the matched parameters. These gradients are probably the most difficult source of error to quantify in the APM Survey. A simple analysis of this propagation of errors was presented in Section 3 of Paper II, and in Sections 3.1.1 and 3.1.2 below, we describe simulations of more complicated error models. A direct comparison with external CCD photometry is discussed in Section 3.2, and further tests to place upper limits on large-scale gradients are discussed in Section 4.2.3.

Without analysing specific error models, we can estimate the effect of correlated residual errors on measurements of $w(\theta)$ by considering the cells estimator of $w(\theta)$ defined in equation (5). The number of galaxies in cell i at magnitude limit m is given by $\log_{10}(N_i) \propto am$, where $a \sim 0.45$ is the slope of the galaxy number counts (Maddox *et.al.* 1990d). A magnitude error δm will thus produce a fractional error in the number of galaxies of $\delta N_i/N_i = a\delta m \ln(10) \approx \delta m$. Any variation in completeness or contamination rate translates directly to a fractional error in the number of galaxies, $\delta N_i/N_i = \delta c$, where δc is the overall error from these two effects, *i.e.* the contamination and the completeness. The total fractional error in the galaxy counts is $e_i = 1 + \delta m + \delta c$. and will vary between plates and as a function of position within each plate; by definition the mean value is unity, $\langle e_i \rangle = 1$.

Since our matching procedure uses the magnitudes and star-galaxy separation parameters of individual objects in the overlap regions, not the galaxy surface density, the errors

e_i are very nearly independent of the galaxy surface density N_i . The estimated angular correlation function, w_{est} , is therefore given by

$$\begin{aligned}
w_{est} &= \frac{\langle e_i N_i e_j N_j \rangle}{\langle e_i N_i \rangle \langle e_j N_j \rangle} - 1 \\
&= \frac{\langle e_i e_j \rangle \langle N_i N_j \rangle}{\langle e_i \rangle \langle e_j \rangle \langle N_i \rangle \langle N_j \rangle} - 1 \\
&= (1 + w_{err})(1 + w_{true}) - 1 \\
&\approx w_{err} + w_{true}.
\end{aligned} \tag{13}$$

if $w \ll 1$. The effect of errors in the survey is therefore simply to add the correlation function of the errors to the true galaxy correlation function. In the next section we consider several models for the combined effects of magnitude and counting errors, and compute the resulting error correlation function w_{err} .

To determine the amplitude of w_{err} we estimate the size of magnitude and counting errors from the consistency of measurements in plate overlaps. If the magnitude and counting errors are uncorrelated, the two amplitudes should be added in quadrature; if they are perfectly correlated they should be added, and if they are anticorrelated they should be subtracted. In practice we find that the magnitude errors totally dominate the errors that propagate through the plate grid.

3.1.1 Uncorrelated overlap errors

In our simplest error model we assume that the error in each overlap is uncorrelated with those in other overlaps, as in the error model that Groth and Peebles applied in their analysis of the Lick map (Groth and Peebles 1986b, hereafter GP86). In principle our analysis applies to both magnitude and counting errors but in practice the counting errors are negligible, and so for simplicity we refer to magnitudes, and mention counting errors only where necessary.

We use the definitions and notation given in Paper II unless stated otherwise, and we begin by summarizing the important quantities. For each plate we define a correction C_i so that an image with measured magnitude m_i has a matched magnitude m_o given by $m_o = m_i - C_i$. In the absence of measurement errors, the difference in magnitudes between galaxies in the overlap between plates i and j is a constant

$$T_{ij} = m_j - m_i = C_i - C_j.$$

In practice, there will be errors on each of these quantities and the plate matching algorithm will converge on estimates of the plate correction factors C_i^e that differ from the true

correction factors C_i . The mean magnitude difference measured in each overlap region, T_{ij}^e , will also differ from the true difference T_{ij} .

If we assume that the errors δT_{ij} in the T_{ij}^e are uncorrelated with each other, so that

$$\langle \delta T_{ij} \delta T_{ik} \rangle = \sigma^2 \delta_{jk}, \quad (14)$$

then we showed in Paper II (equation 23) that the variance in the difference between the T_{ij}^e and the plate correction factors on each overlap is given by

$$\epsilon^2 = \text{var}(T_{ij}^e + C_j^e - C_i^e) = \frac{N-1}{N+1} \sigma^2 \approx \frac{2}{3} \sigma^2. \quad (15)$$

where N is the mean number of overlaps on each plate.

Using the plate overlaps to calculate the correction factors C_i^e introduces correlations between the correction factors of different plates (*c.f.* de Lapparent *et al.* 1986). The propagation of these errors through a periodic square grid of plates can be analysed analytically and an expression for $\langle \delta C_i \delta C_j(\theta) \rangle$, based on this model is given in equation (31) of Paper II. However, the assumption of a periodic array of plates is not a good representation of the real plate configuration of the APM survey. We have therefore carried out Monte Carlo simulations using the real plate configuration as described in Paper II. In these simulations, a random Gaussian error was generated for each overlap and used to estimate the overlap offsets in the edge-matching procedure. The resulting correction coefficients are actually the errors that would be introduced in the plate-correction factors by the errors in the plate overlaps. The correlation function of errors, w_{err} , is thus given by the correlation function of the correction coefficients. As shown in Figure 14 of Paper II, the resulting w_{err} has small oscillations similar to the analytic function at $\theta \lesssim 10^\circ$, but on larger scales the Monte Carlo results decline smoothly while the analytic function remains oscillatory.

For the APM survey, the variance in overlap residuals measured directly from the overlaps is $\epsilon^2 = 1.9 \times 10^{-3}$ (see Paper II). The mean number of overlaps per plate is approximately $N = 5$ for the UK Schmidt fields, so equation (15) gives

$$\sigma^2 = 3.2 \times 10^{-3}, \quad (16)$$

ie the *rms* mean magnitude difference in a plate overlap is 0.057 magnitudes, which corresponds to a 6% fractional error in the galaxy density on a single Schmidt plate.

The corresponding overlap measurements for the ψ classification parameter described in Paper I, which we use to separate stars and galaxies, give a dispersion of $\epsilon = 44.5$. The number of galaxies as a function of ψ is well fit by an asymmetrical distribution centred on $\psi = 2166$ with dispersions $\sigma_1 = 603$ and $\sigma_2 = 347$, (see equation 2 of Paper I for a

definition of the parameters σ_1 and σ_2). Our galaxy sample is defined by selecting objects with $\psi > 1000$, so the observed dispersion in ψ introduces a dispersion of roughly 0.3% in galaxy density on a single Schmidt plate. Magnitude errors therefore totally dominate the propagation of errors in the galaxy counts. Note however, that the galactic gradient in stellar density will cause a gradient in the contamination rate, independent of the plate-matching procedure.

Using the magnitude *rms* overlap residual to normalize the error estimates, the analytic model predicts that the error correlation function at zero lag is

$$w_{err}(0) = \beta_{ii}^2 = 0.457\sigma^2 \approx 1.8 \times 10^{-3}. \quad (17)$$

In (17) we use the notation of GP86 where β_{ii}^2 denotes the variance in the plate zero points. At larger scales where the Monte Carlo estimate becomes smooth, w_{err} can be approximated roughly by an exponential

$$\langle \delta C_i \delta C_j(\theta) \rangle \approx w_{err}(\theta) \approx 0.49 \sigma^2 \exp(-\theta/\theta_c), \quad \theta_c \approx 11^\circ, \quad \theta \lesssim 50^\circ. \quad (18)$$

Over the range $10^\circ \lesssim \theta \lesssim 50^\circ$ equation (18) is accurate to within a few percent.

It is possible to check if the model for w_{err} is consistent with the data by computing the intra-plate and inter-plate estimates of $w(\theta)$ (see GP77 and Maddox *et al.* 1990c). The intra-plate estimate is derived by counting only galaxy pairs that lie on the same plate while the inter-plate estimate is derived by counting only galaxy pairs that lie on neighbouring plates. Since the true correlation function is independent of the choice of plate boundaries, any difference between the intra-plate and inter-plate estimates should be due to the difference in the error correlation function*. The error on the intra-plate correlation function is $w_{err}(0)$, and the error on the inter-plate estimate is approximately $w_{err}(5^\circ)$, since $\theta = 5^\circ$ corresponds to the distance between neighbouring Schmidt plates. In the analytic error model

$$w_{err}(5^\circ) \approx \beta_{ij}^2 = 0.208\sigma^2 \approx 1.0 \times 10^{-3}, \quad (19)$$

where, following the notation of GP86, β_{ij}^2 denotes the covariance between the zero point errors for neighbouring plates. Hence the predicted difference between inter- and intra-plate estimates of $w(\theta)$ is approximately $\beta_{ii}^2 - \beta_{ij}^2 \approx 0.8 \times 10^{-3}$. The offset observed from the APM measurements is 1.7×10^{-3} , which suggests that this uncorrelated error model may

* Although this is true in the mean, any single realization of a clustered distribution is likely to have some structure correlated with plate boundaries, so some offset is expected. This is discussed more fully in Section 3.5

be too simplistic. We discuss this test in more detail after considering more complex error models in the next section.

3.1.2 Correlated overlap errors.

The error model of the previous section assumes that the overlap errors are uncorrelated. Though this assumption enables an analytic approach to the modeling, it may not be a good approximation to the APM survey because the overlap errors are dominated by residual field errors. There are 3000 galaxies in a typical overlap with an *rms* error of 0.2 magnitudes per galaxy, so the random magnitude error in a single plate overlap is $0.2/\sqrt{3000} \sim 0.005$ magnitudes. In the absence of residual field effects, this would be the only source of error in the matching procedure, and so the plate-matching errors would be of similar order. However, the uncertainties in the corrections for field effects are expected to be of order 0.05 magnitudes, and so will dominate the error in each overlap. This is consistent with the observed dispersion between magnitudes in overlaps which is 0.06 magnitudes, as described in the previous section. The field correction errors are very likely to be systematically correlated for each plate: for example if the amplitude of the applied field correction is too small for a particular plate, then all of the edges would be low compared to the true value. We must therefore consider error models which include residual field errors.

Before describing these models, we point out that in the Lick survey, the assumption of uncorrelated errors is much more likely to be valid. The Lick plates were not hypersensitized and so the field effects should be similar for all plates. Applying the average field correction to all plates should therefore be accurate. Furthermore, the Lick plate matching used galaxy counts in plate overlaps to estimate the different depths of neighbouring plates. Since the counts on each unmatched plate sample the galaxy distribution to a different depth, and galaxies are clustered, this introduces an error in the estimated plate depths. In fact this error is much larger than the residual field errors. Since it depends on the galaxy distribution, the error is uncorrelated with the plate boundaries, and so it is reasonable to assume uncorrelated overlap errors for the Lick survey.

To simulate the effects of residual field errors in the APM Survey, we first generate an error, $S(x, y)$, as a function of position for each plate in the survey. This represents the total error in galaxy density as a function of position (caused by magnitude and classification errors), but as discussed in the previous section, the magnitude errors are the dominant contribution. We consider three functional forms to represent the residual field errors:

[A] Linear mode: $S(x, y) = 1 + ax + by$ where a and b are independent and selected at random from Gaussian distribution with zero mean and dispersion s .

[B] Quadratic mode: $S(x, y) = 1 + ax^2 + by^2$ with a and b selected as in mode A.

[C] Radial mode: with $S(x, y) = 1 + a(x^2 + y^2)$, and a selected as in modes A and B.

The error function for each plate was generated independently of the others and each field was also assigned a random global zero-point error with a distribution similar to that observed in the survey (Figure 11, Paper II).

For each neighbouring plate pair the difference between the functions at the common plate edge is used to measure an overlap offset. As for the real data, the iterative plate matching procedure (Section 3, Paper II) was applied to the model plate grid giving a set of estimated plate corrections which minimize the overlap residuals. The resulting corrections are added to the original field errors for each plate to give a map of the overall residual errors which includes both the original field errors, and any plate-to-plate matching errors introduced by the overlap errors. Finally we measure the final error correlation function using equation (5) applied to this error map.

The mean of 100 realizations for each mode are shown in Figures (4a)–(4c). The filled circles joined by the solid lines show the inter-plate estimates of $w(\theta)$ and the open circles joined by the dotted lines show the intra-plate estimates. In the models for these plots we chose the dispersion s for each of the modes so that the residual overlap error in the model is $\epsilon^2 = 1.9 \times 10^{-3}$ as measured in the real data. Table 1 gives the values for s normalized so that the plate coordinates x and y are in the range -1 to $+1$.

Table 1: Offsets and normalizations for different error modes

	mode	s	inter-intra offset	$w_{err}(0) \sim \beta_{ii}^2$
A	linear	0.07	1.0×10^{-3}	1.6×10^{-3}
B	quadratic	0.10	1.1×10^{-3}	1.7×10^{-3}
C	radial	0.22	6.9×10^{-3}	8.3×10^{-3}

As seen in Figure 4 the correlation functions of the errors for modes [A] and [B] are similar to the uncorrelated error model of the previous subsection. This is reasonable because the overlap errors for modes [A] and [B] are relatively weakly correlated and so the simple model of Paper II provides an adequate approximation. The intra-inter-plate offsets are slightly larger than the predictions of the Paper II model, because the intra-plate estimates include the structure of the error function within each plate. The offsets are slightly smaller than measured from the real data.

There are also small differences between behaviour of the inter- and intra-plate estimates of modes [A] and [B]. For mode [A] the linear gradient in errors across each field produces a gradient in the intra-plate estimates: the offset is more positive on small scales and negative at larger scales. For mode [B] the intra-inter-plate offset is more uniformly positive, with a slight increase between 6° and 7° , where the intra-plate estimate is based on galaxies in the very corners of the plates and the quadratic error functions have a large dispersion.

For mode [C] the overlap errors are almost perfectly correlated, so if the plate grid were uniformly rectangular, this mode would produce perfectly consistent plate overlaps, and there would be no residual dispersion in the overlaps. The real plate grid has overlaps of differing size and position for each field, and so there are small overlap residuals, but still this mode very poorly constrained by plate overlaps. For the parameters which match the observed variance in the overlap residuals of the APM Survey, mode [C] leads to a very high intra-plate estimate of $w(\theta)$, which is inconsistent with the data. In fact, comparing the observed and predicted inter-intra-plate offset in $w(\theta)$ provides a much better limit to the normalization of this mode of errors. Since the overlap residuals are so small in this error mode, the errors propagate less strongly through the plate network in comparison to the other two modes, leading to much smaller errors on scales larger than 7° . Note that the small overlap residuals seen in the ψ matching do not constrain possible mode [C] field errors in the star-galaxy separation. Although the counting errors do not contribute significantly to errors which propagate through the survey, they may still be significant in terms of radial field errors.

The intra- and inter-plate measurements from the real data in the magnitude range $17 \leq b_J \leq 20$ are plotted in Figure 5. The open circles show the intra-plate estimate of $w(\theta)$ and the filled circles the inter-plate estimate of $w(\theta)$. In each case we show the mean $w(\theta)$ from the four zones as described Section 2.3, and plot 1σ error bars from the scatter between the four zones. In the range $1.5^\circ < \theta < 4^\circ$, where the errors on both estimates are relatively small we find a mean offset $w_{intra} - w_{inter} = 1.7 \pm 0.7 \times 10^{-3}$. The size of the offset is similar to that expected from modes [A] and [B], but much smaller than mode [C]. In principle, we could reproduce the shape of the observed offset using some linear combination of the three modes, but the large uncertainties in the observations would make such a decomposition unreliable.

We have estimated the uncertainty in the observed offset from the dispersion between the four zones, as quoted above and plotted as error bars in Figure 5. This suggests that the $w_{intra} - w_{inter}$ is positive at only the one sigma level. The large scatter in the offsets measured in the different zones may seem surprising, but is in fact consistent with the scatter expected from ‘cosmic’ variance. We have tested this by computing inter- and intra- plate

estimates of $w(\theta)$ for several hundred simulations of clustered distributions using the Soneira-Peebles (1978) technique described in Appendix A1. For each realization, we imposed an artificial plate grid to calculate intra- and inter-plate estimates of $w(\theta)$. No errors were added to the simulated distribution, and the grid was used only to decide which pairs of cells to count for the intra-plate estimates and which for the inter-plate estimates. The rms scatter in the inter- intra-plate angular correlations was found to be 1×10^{-3} , in good agreement with the observed scatter between the 4 zones of the APM survey. Therefore the observed value $w_{intra} - w_{inter} = 1.7 \times 10^{-3}$ is only marginally significant evidence for errors in the APM measurements. Nevertheless we can use the measurement to limit the amplitude of mode [C] errors to be $\lesssim 2 \times 10^{-3}$ at zero lag.

In summary, the observed overlap residuals provide strong constraints on errors of the form [A] or [B], so that the zero-lag amplitude must be $1.7 \times 10^{-3} \lesssim \beta_{ii}^2 \lesssim 3 \times 10^{-3}$, corresponding to a magnitude error of between 0.041 and 0.054 magnitudes. The observed inter-intra-plate offset limits mode [C] errors to to have an amplitude $\lesssim 2 \times 10^{-3}$ at $\theta \lesssim 0.5^\circ$. Including all modes [A]-[C], these constraints limit the error correlation function to be $w_{err} \lesssim 6 \times 10^{-4}$ on angular scales $\theta \gtrsim 5^\circ$.

3.2 Comparison of APM photometry with CCD magnitudes

Two methods of measuring correlated errors in the APM photometry were analyzed in detail in Paper II:

- (a) The covariance of residuals between the matched magnitudes and 41 CCD sequences distributed over the survey. This directly measures the contribution to $w(\theta)$ from gradients in the magnitude matching and indicates that $w_{err} \lesssim 10^{-3}$ (see Figure 24 Paper II).
- (b) The covariance of the estimated plate zero-points (see Figure 16 of Paper II). Assuming that the *true* plate zero points C_i are uncorrelated, correlations between the *estimated* plate zero points C_i^e provide a measure of correlated plate-matching errors. As described in Paper II, the correlation function of the estimated plate zero points sets a limit of $\lesssim 10^{-3}$ on the error in $w(\theta)$ arising from large-scale gradients in the survey.

Fong *et al.* (1992, hereafter F92) have argued that some of the signal in our estimates of $w(\theta)$ from the APM Survey might be caused by large-scale gradients which we have failed to detect in these and other tests. Tests such as (b) are indirect and it is possible, though extremely unlikely, that the true plate zero points are anticorrelated with the estimated plate zero points to a high precision thus masking gradients in the survey. A direct test, *i.e.* in which independent photometry is compared with that of the APM Survey, is clearly the most convincing way of checking the uniformity of the APM magnitudes. Recently we have

been able to make such a comparison using CCD magnitudes of 13570 galaxies measured by Shectman *et al.* (1992, 1995). This is described in Section 3.2.1. We postpone a more detailed discussion of Fong *et al.* ’s criticisms until Section 3.2.2.

3.2.1 Comparison of Las Campanas CCD and APM magnitudes

The CCD Photometry used in this Section is part of the Las Campanas Deep Redshift Survey (LCDRS) described by Shectman *et al.* (1992). The CCD photometry is in the R band and was obtained from drift scans with the Las Campanas 1-metre Swope telescope. The scanned areas that have been kindly made available to us consist of a number of “bricks” of area $1.5^\circ \times 3.0^\circ$ in three declination strips running along the entire width of the APM survey, as shown in Figure 6. We have correlated the positions of APM galaxies with the LCDRS images and computed the mean magnitude difference $\Delta m = b_J - m_{CCD}$ as a function of UKSTU field. The CCD magnitudes are limited to $m_{CCD} \lesssim 18$, and the mean colour difference is $\langle \Delta m \rangle = 1.251$. Because of the large wavelength difference of the passbands in the two surveys, the *rms* dispersion of Δm about the mean is large and is equal to 0.45 magnitudes. Fortunately, there are a large number of galaxies with CCD magnitudes on most of the UKSTU fields and so the net scatter on the transforms arising from colour differences is small.

Table 2 summarizes the results of the comparison of the APM and LCDRS photometry. The second column of the Table lists the UKSTU field number and the third column gives the number of galaxies with CCD magnitudes in the LCDRS survey matched to APM galaxies in the field. Columns 4-9 list the mean right ascension and declination (equinox 1990.5) for the matched galaxies. Column 10 gives the mean magnitude difference $\delta m = \Delta m - \langle \Delta m \rangle$ and column 11 gives the *rms* dispersion about the mean for a single galaxy σ_m . The error on δm is thus $\sigma_m / \sqrt{N_g}$. We analyze only those UKSTU fields with more than 100 galaxies from the LCDRS CCD frames; there are a few fields with a smaller number of galaxies, but the uncertainties in δm for these are dominated by the dispersion in the galaxy colours.

From the entries in Table 2, we find

$$\sigma(\delta m) = 0.058, \tag{20a}$$

$$\sigma(m) = 0.028, \tag{20b}$$

where $\sigma(m)$ is the contribution to the variance from scatter in the individual magnitudes on each field,

$$\sigma^2(m) = \frac{1}{N_f} \sum_i^{N_f} \sigma_m^2(i) / N_g(i), \tag{21}$$

Table 2: Las Campanas CCD-APM magnitude residuals

	UKSTU	N_g	α^\dagger			δ^\dagger			δm	σ_m
1	236	141	21	42	50	-48	6	36	-0.001	0.724
2	237	379	21	51	28	-48	9	35	0.012	0.500
3	241	284	23	59	24	-43	51	36	-0.050	0.488
4	242	198	0	28	37	-45	1	12	-0.017	0.555
5	245	312	1	50	55	-44	37	11	0.043	0.399
6	246	242	2	23	40	-44	28	47	-0.173	0.446
7	247	185	2	43	45	-43	31	47	0.022	0.352
8	248	457	3	13	50	-44	47	24	0.004	0.340
9	249	538	3	48	23	-44	50	24	-0.135	0.431
10	251	155	4	32	38	-45	10	48	0.007	0.407
11	288	114	21	50	43	-47	22	48	0.071	0.462
12	290	245	23	2	52	-44	57	0	0.094	0.396
13	291	221	23	14	23	-44	34	48	0.030	0.534
14	293	887	23	59	25	-40	34	48	-0.020	0.450
15	294	1036	0	26	3	-39	39	35	0.012	0.444
16	295	343	0	53	50	-40	49	48	-0.065	0.442
17	296	621	1	15	40	-39	54	0	0.036	0.442
18	297	366	1	46	11	-39	35	24	-0.031	0.448
19	298	273	2	5	50	-41	29	24	0.028	0.521
20	299	674	2	36	14	-40	16	12	0.027	0.447
21	300	747	3	3	19	-39	47	59	0.017	0.416
22	301	476	3	28	12	-41	40	48	-0.051	0.431
23	302	606	3	48	23	-38	58	12	-0.075	0.492
24	303	307	4	26	12	-38	53	23	0.053	0.486
25	342	386	21	7	16	-38	59	24	-0.025	0.517
26	343	279	21	45	50	-39	2	59	0.033	0.512
27	345	724	22	29	38	-38	58	12	-0.049	0.458
28	346	285	23	5	43	-39	3	36	0.093	0.414
29	347	345	23	20	40	-40	33	36	0.037	0.446
30	348	285	23	43	37	-38	57	35	0.049	0.428
31	359	199	4	5	59	-35	57	0	0.015	0.448

† Equinox 1990.5

and N_f is the number of fields. If errors in the CCD zero points can be neglected, the rms error in the zero point of an APM field is

$$\sigma_{APM} = (\sigma^2(\delta m) - \sigma^2(m))^{1/2} = 0.051. \quad (22)$$

The quantity σ_{APM} is the square root of β_{ii}^2 defined in equation (17), which we have estimated to be between 0.041 and 0.054 in Section 3.1.

Figure 7 shows the residuals δm plotted as a function of right ascension. The Figure shows that the residuals are uncorrelated with right ascension; there is no evidence for any east-west gradient in the APM magnitude system. Two fields, 246 and 249 are outliers in Figure 7 and have residuals of -0.173 and -0.135 respectively, showing that the distribution of the magnitude errors is non-Gaussian. We have checked whether these fields show any peculiarities that might account for such large magnitude errors. Field 249 contains one of our calibration sequences (see Table 3), and the residual between the APM and CCD magnitudes is only 0.037, showing no evidence of poor matching. The plate correction factors δC^e applied to these fields (0.12 and 0.11 for 246 and 249) are not unusual when compared to the distribution of APM plate correction factors, which is well approximated by a Gaussian, with $rms \langle (\delta C^e)^2 \rangle^{1/2} = 0.178$ (*cf* Figure 11 of Paper II). The fluctuations in the galaxy surface density on each field, $\delta n/n$, to a magnitude limit of $b_J = 20$ are plotted against the zero point residuals δm in Figure 8. The surface density fluctuations on fields 246 and 249 are positive and equal to $\delta n/n = 0.148$ and 0.091 respectively, compared to the rms over all 185 plates of 0.143. The surface densities on these plates are thus typical of the rest of the survey and provide no firm evidence of large zero point errors. Another possible cause of these outlying points might be zero point errors in the CCD magnitudes; for example, the residual for field 246 would not look so improbable if the CCD zero point were in error by ~ 0.05 magnitudes.

It is therefore reasonable to exclude field 246 from the analysis giving

$$\sigma(\delta m) = 0.050, \quad (23a)$$

$$\sigma(m) = 0.028, \quad (23b)$$

$$\sigma_{APM} = 0.041, \quad (\text{minus field 246}). \quad (23c)$$

We conclude that the dispersion in the APM plate zero points lies in the range $0.041 \lesssim \sigma_{APM} \lesssim 0.051$ and that the lower value is probably more appropriate. This estimate is in excellent agreement with the limits $0.041 \lesssim \sigma_{APM} \lesssim 0.054$ determined from our analysis of errors in Section 3.1.

In Figure 9, we plot the correlation function for the LCDRS CCD-APM residuals,

$$\langle \delta m_i \delta m_j \rangle - \sigma^2(m) \delta(\theta) \quad (24)$$

and the error bars are computed on the assumption that the δm_i are uncorrelated,

$$\text{var}[\langle \delta m_i \delta m_j \rangle] = \frac{\sigma^2(\delta m)}{N_{pairs}} \quad (25)$$

where N_{pairs} is the number of distinct field pairs used in the bin centred on angle θ . The two sets of points show the correlation functions with and without field 246, but apart from the small difference at zero lag, the exclusion of this field causes no significant change to the correlation function.

The solid line plotted in the figure shows the correlation function for the error model [A] in Section 3.1 normalized to be 1.7×10^{-3} at zero lag, as required to match the observed plate overlap residuals $\epsilon^2 = 2 \times 10^{-3}$ (see Section 3.1). This error mode produces the largest error correlation function on large scales, and so is the worst case for our measurements. For all of our error models, the correlation function of the magnitude errors should be $\lesssim 10^{-3}$ on scales $\theta \gtrsim 2^\circ$, and this is compatible with the absence of any large scale correlations in the CCD-APM residuals. Figure 9 can be compared to similar figures plotted in Paper II showing the covariance of the zero-point correction factors $\langle C_i^e C_j^e \rangle$ (Figure 16 of Paper II) and the correlation function of the residuals between our own CCD zero points and APM magnitudes (Figure 24 of Paper II). In all cases, these correlation functions are consistent with zero to an accuracy of $\lesssim 1 \times 10^{-3}$ at $\theta > 4^\circ$.

In summary, the comparison between the LCDRS and APM magnitudes shows that the rms error in APM plate zero-points is $0.041 \lesssim \sigma_{APM} \lesssim 0.051$, and that the resulting error in $w(\theta)$ is less than 1×10^{-3} at $\theta > 4^\circ$. These estimates are in excellent agreement with the limits between $0.041 \lesssim \sigma_{APM} \lesssim 0.054$ and the error correlation functions determined in Section 3.1.

3.2.2 Comparison of APM CCD calibrations and APM magnitudes

In Paper II we presented a comparison of APM magnitudes with CCD magnitudes that we determined from observations with the 1m telescope at the South African Astronomical Observatory.

Recently, Fong *et al.* (hereafter F92) have used our CCD sequences to argue that we have underestimated the errors in the APM magnitudes and that the magnitude errors correlate on large-scales leading to a roughly linear gradient in the magnitude scale with right ascension.

From the APM and CCD magnitudes, we follow F92 and compute the statistics

$$\sigma_B^2 = \sum_{i=1}^k n_i \frac{(\bar{c}_i - \bar{c})^2}{\bar{n}(k-1)}, \quad (26a)$$

$$\sigma_W^2 = \sum_{i=1}^k \sum_{j=1}^{n_i} \frac{(c_{ij} - \bar{c}_i)^2}{\bar{n}(N-k)}, \quad (26b)$$

where

$$c_{ij} = (m_{APM})_{ij} + (b_J)_{ij}/1.097, \quad (27a)$$

$$\bar{c}_i = \sum_{j=1}^{n_i} \frac{c_{ij}}{n_i}, \quad \bar{c} = \frac{1}{N} \sum_{i=1}^k \sum_{j=1}^{n_i} c_{ij}, \quad (27b)$$

$$\bar{n} = \frac{N}{k}, \quad N = \sum_{i=1}^k n_i, \quad (27c)$$

and there are n_i galaxies in each of k sequences. The factor of 1.097 in equation (27a) takes into account the small deviation from unity of the slope in the relation between APM magnitudes and CCD b_J magnitudes (see Paper I, note that the APM magnitudes before conversion to the b_J system are defined to be negative, hence the plus sign in equation 27a). The excess variance caused by plate matching errors is

$$\sigma_{APM}^2 = \sigma_B^2 - \sigma_W^2. \quad (28)$$

These statistics are almost identical to the statistics used in Section 3.2.1 to measure the excess variance from the LCDRS CCD and APM photometry, differing only in the weighting given to sequences containing different numbers of galaxies. Calculating these statistics to the sequences listed in Table 3 of Paper II, we find

$$\sigma_B = 0.1167, \quad (29a)$$

$$\sigma_W = 0.0857, \quad (29b)$$

$$\sigma_{APM} = 0.079. \quad (29c)$$

The estimate of σ_{APM} derived here is slightly smaller than the value 0.084 found by F92. We have combined the multiple sequences in fields 344 and 530 in computing these numbers. The residuals $\bar{c}_i - \bar{c}$ and the scatter for each sequence are given in Table 3.

As discussed in Paper II, the residual for the sequence on field 152 is -0.363 , differing from the mean by more than three standard deviations. Excluding field 152, we find

$$\sigma_B = 0.1055, \quad (30a)$$

$$\sigma_W = 0.0849, \quad (30b)$$

$$\sigma_{APM} = 0.063 \quad (\text{minus field 152}). \quad (30c)$$

Table 3: APM CCD-APM magnitude residuals

	UKSTU	N_g	α			δ			$(\bar{c}_i - \bar{c})$	σ_m
1	53	7	0	8	5	-67	52	4	0.021	0.087
2	108	7	23	48	14	-65	41	56	0.077	0.115
3	110	6	23	56	1	-66	51	50	0.160	0.051
4	113	4	0	0	14	-61	23	45	-0.012	0.141
5	145	8	23	48	10	-62	37	4	0.006	0.114
6	147	9	23	56	2	-61	52	40	-0.003	0.200
7	152	5	0	4	8	-52	52	26	-0.367	0.260
8	193	8	23	56	13	-47	57	10	-0.068	0.141
9	195	6	0	0	15	-50	0	53	-0.072	0.256
10	199	4	0	8	14	-52	8	31	-0.221	0.208
11	235	7	23	44	15	-50	2	5	0.009	0.195
12	237	10	23	52	2	-52	0	57	0.145	0.174
13	244	9	0	4	5	-44	44	27	-0.192	0.180
14	249	7	0	12	9	-45	19	33	0.037	0.256
15	287	12	23	48	9	-47	17	41	0.073	0.216
16	302	6	0	12	11	-41	22	22	-0.012	0.173
17	304	4	0	16	11	-38	3	36	-0.081	0.113
18	342	8	23	48	0	-41	27	35	-0.063	0.207
19	344	8	23	52	1	-39	14	6	0.046	0.103
20	344	9	23	52	4	-39	59	56	-0.061	0.140
21	347	7	23	56	6	-39	30	39	0.003	0.247
22	349	6	23	56	14	-34	42	50	0.037	0.269
23	355	4	0	8	7	-36	26	38	0.031	0.127
24	401	8	23	44	15	-36	18	32	0.195	0.075
25	403	9	23	48	10	-34	15	18	0.123	0.231
26	405	7	23	52	2	-36	55	33	-0.005	0.155
27	407	6	23	56	3	-33	35	42	-0.164	0.186
28	412	4	0	4	5	-30	15	7	-0.137	0.016
29	418	8	0	12	8	-29	8	16	-0.174	0.242
30	467	4	23	52	4	-29	19	4	-0.100	0.413
31	469	5	23	52	13	-29	42	57	0.179	0.152
32	471	5	23	56	12	-30	26	2	0.036	0.221
33	477	8	0	8	0	-27	3	43	-0.068	0.242
34	530	5	23	48	3	-23	12	32	0.189	0.342
35	530	5	23	48	5	-27	25	8	0.122	0.494
36	533	6	23	52	4	-26	49	33	-0.023	0.272
37	535	6	23	56	4	-26	21	7	0.129	0.153
38	550	5	0	16	1	-17	28	47	-0.099	0.084
39	599	7	23	48	7	-18	16	1	0.021	0.189
40	603	4	23	52	12	-17	46	12	0.249	0.230
41	605	4	23	56	6	-22	22	4	0.135	0.236

Notes: The second column gives the UKSTU field number in which each CCD sequence is located. The third column gives the number of galaxies in each sequence. The next six columns give the right ascension and declination of the CCD centres (epoch 1950). The tenth column given the mean difference between the CCD and APM magnitudes as defined in equations (27). The final column gives the *rms* fluctuation in the magnitude differences (c_{ij}) for each sequence.

F92 use numbers similar to those in equations (29) to argue that we have underestimated the errors in the APM zero points, concluding that the error is closer to 0.08 magnitudes rather than the value 0.04–0.05 estimated in Paper II and Sections 3.1 and 3.2.1 of this paper. However, this is extremely unlikely for the following reasons:

[1] There can be little doubt that the CCD photometry in field 152 is in error because the galaxy number density on the plate is *underdense* by 11%, whereas if the APM magnitudes in this field were in error by 0.36 magnitudes, we would expect the galaxy number density in this field to be *high* by $\approx 40\%$. Consistency between the CCD zero point on this field and the observed number counts would thus require that field 152 is underdense by more than 50%, *i.e.* by about 3.5 standard deviations, which is implausible. Figure 10 shows the magnitude residuals plotted against fluctuations in the galaxy surface density to a magnitude limit $b_J = 20$ in each APM field. There is no trend between the magnitude residuals and the galaxy density.

[2] The errors on the zero point of each individual sequence are large because the number of galaxies are small. The *rms* deviation of the APM-CCD and APM magnitudes is $\sigma_m = 0.24$, *i.e.* about half the dispersion measured in the previous section for the LCDRS and APM magnitudes. The smaller dispersion between the APM CCD and APM magnitudes arises because the APM CCD sequences were taken in the *B* and *V* passbands. The CCD magnitudes were transformed to the b_J passband via a colour equation (equation 33 of Paper II) and so the dispersion caused by the mismatch between the CCD and APM passbands is much smaller than for the R-band LCDRS photometry. However, whereas there are typically 400 galaxies in each LCDRS-APM sequence, there are only ≈ 7 in the APM CCD sequences. The accuracy with which we can determine σ_{APM} from the APM calibrations is therefore relatively poor. Figure 11 shows the distributions of 10000 Monte Carlo computations in which we have generated 39 sequences with the same number of galaxies per sequence as listed in Table 4. Each magnitude has a Gaussian random error of 0.22 magnitudes. The solid and dotted histograms show the distribution of σ_{APM} measured from the statistics assuming that the zero point errors are Gaussian distributed with dispersion 0.045 and 0.080 magnitudes respectively. These Monte Carlo calculations show that a measured value of $\sigma_{APM} = 0.063$ (*i.e.* the value determined excluding field 152) occurs with a probability of about 24% if $\sigma_{APM} = 0.045$, and so is perfectly reasonable.

[3] If we include field F152, then the measured value of $\sigma_{APM} = 0.079$ excludes a true value of $\sigma_{APM} = 0.045$ at about the 93% confidence level. However, we have shown that the outlying CCD sequence in field 152 *must* be an error because the galaxy counts in this field are close to the mean value for the whole survey (Figure 10). Furthermore, high values of σ_{APM} are inconsistent with the results from the LCDRS CCD sequences. For

example, if the true value of $\sigma_{APM} = 0.080$, the probability of measuring $\sigma_{APM} \leq 0.051$ from the LCDRS sequences is less than 0.64%. Fong *et al.*'s assertion that $\sigma_{APM} \approx 0.08$ can thus be excluded at a very high confidence level.

[4] Some of the scatter in the comparison with APM-CCD and APM magnitudes might be caused by systematic errors in converting B and V magnitudes to the b_J system (see Paper II). If we exclude galaxies with very blue colours, $B - V \geq 1.25$, then we find $\sigma_{APM} = 0.063$ if field 152 is included and $\sigma_{APM} = 0.043$ if field 152 is excluded.

F92 also point out that the APM CCD sequences indicate a large-scale gradient correlated with right ascension. We plot the magnitude residuals against α in Figure 12 and in agreement with F92 we find some indications for a large-scale gradient in the magnitude residuals. However, the error bars are large and so the evidence for a linear gradient is of marginal statistical significance. We make the following remarks concerning Figure 12:

[1] Even if we accept that the gradient in Figure 12 is caused by large-scale correlated errors in the APM magnitudes, the correlation function for these residuals (Figure 24 in Paper II) has a low amplitude and would cause very little change to our estimates of $w(\theta)$.

[2] The comparison of APM with LCDRS photometry as a function of right ascension (Figure 7) shows no evidence for a large-scale gradient in the APM magnitude residuals. If there is a large-scale gradient in the APM photometry, it is evidently *not* a simple gradient in right ascension.

[3] The lower panel in Figure 12 shows fluctuations in the mean galaxy surface density to $b_J = 20$ plotted as a function of right ascension for the plates containing APM CCD fields (open circles) and for all 185 fields (filled circles). In each case, there is no evidence of a gradient in the galaxy counts. In their discussion of gradients, F92 consistently ignored the important point that our estimates of $w(\theta)$ are derived from the *galaxy counts*. It is evidently incorrect to infer that magnitude errors introduce errors in $w(\theta)$ via large-scale gradients in the galaxy counts if, in fact, there are no such large-scale gradients in the counts.

[4] The absence of gradient in the galaxy counts could be caused by an unlikely compensation between systematic variations in magnitude and star galaxy classification. Large-scale gradients caused by classification errors are discussed in more detail in Section 3.5.

3.3 Tests for systematic errors correlated with scan and exposure dates

3.3.1 Scan dates

First we consider the plate scanning process. The best check for errors in this step is simply to scan the same plate more than once and compare the image parameters measured from each scan. For a few plates we compared scans made at different times during the survey and these showed no evidence for significant variations in the measured image parameters. Such a comparison is impractical for more than a few fields, but we have tested for systematic trends in all fields by producing a scatter plot of galaxy density for each Schmidt plate in order of APM scan. As shown in Figure 13, the galaxy density shows no systematic trend with scan date.

Furthermore, we can check directly that the scanning date has no effect on the $w(\theta)$ measurements by evaluating $w(\theta)$ separately for plate pairs with a scan interval < 1 year and > 1 year. The resulting estimates, together with the total $w(\theta)$ are shown in Figure 14. The difference between the overall estimate (solid line) and the other estimates (dotted and dashed lines), is $\sim 10^{-3}$. From our lengthy discussion in Sections 3.1 and 3.2, we expect to see random errors of order 10^{-3} , and so this difference is not statistically significant. We also evaluated $w(\theta)$ after simply discarding plates scanned during some periods. This produced virtually no change in $w(\theta)$. Thus it is unlikely that APM scan variations have seriously biased our correlation functions.

3.3.2 Exposure dates

Other possible sources of plate-to-plate scatter include variations in emulsion sensitivity and observing conditions. These would show up as changes in the detection efficiency as a function of the exposure date of each plate. Figure 15 shows the galaxy surface density on each plate plotted against its exposure date; no significant trend is seen showing that there is no evidence for any long-term temporal dependence in the completeness of the APM Survey.

The clustering of the galaxy distribution introduces a scatter of $\approx 11\%$ in the number of galaxies per plate, so we must average over many plates to test for variations with smaller amplitude. An average of roughly 20 plates per year were taken for the survey, and so it is impossible to check directly for $\lesssim 3\%$ variations over time-scales less than about a year. However, short term variations can be excluded as a significant source of error on scales $5^\circ - 10^\circ$ by considering the distribution of exposure dates across the sky as plotted in Figure 17 of Paper II. Only 54 out of the 505 pairs of neighbouring plates were exposed within a month of each other compared to 36 expected for a random distribution. The *rms* of the unmatched plate zero points is only 0.2 magnitudes, so in the worst case, where the 18 excess plate pairs have perfectly correlated errors of 0.2 magnitudes, the error in $w(\theta)$ would be only $(18/505) \times 0.2^2 \sim 1.4 \times 10^{-3}$.

3.4 Plate-independent Errors

Obscuration by galactic and intergalactic dust, variable contamination by stellar images and atmospheric absorption can introduce errors in the survey which would continue smoothly across plate boundaries. Such errors would not be corrected by the plate-matching procedure, and would not show up in the tests carried out in the previous sections. In this subsection we present tests that show none of the effects significantly bias our measurements of $w(\theta)$.

3.4.1 Galactic Extinction

Extinction by dust in our Galaxy introduces a gradient in galaxy density with Galactic latitude, and the patchiness of the obscuration can produce spurious clustering on smaller scales. The extinction can be estimated from the 100 micron emission as mapped by the IRAS satellite. Assuming that all the dust is at the same temperature, the thermal emission will trace the column density of dust in any particular direction, and hence it is possible to predict the extinction at visual wavelengths. This has been studied by Rowan-Robinson et al (1991), who estimate a constant to convert from 100 micron surface brightness to an extinction value, $A_V = 0.06I_{100}$.

In our equatorial survey covering the sky with $22^{hr} < \alpha < 4^{hrs}$ and $-17.5^\circ < \delta < +2.5^\circ$, the extinction is high enough that we can see an anti-correlation between the surface density of galaxies and I_{100} if no correction is applied. Applying magnitude corrections from the IRAS map removes the overall correlation between the galaxy density and I_{100} , but inspection of the corrected galaxy maps reveals that there are several small patches of high I_{100} emission which are still underdense in galaxies. It is probable that these patches correspond to clouds of dust that are colder than the mean dust temperature, leading to a higher extinction per unit 100 micron flux. In the region with $\delta < -17.5^\circ$ the predicted extinction varies by less than 0.05 magnitudes, and there are none of these anomalous patches, so the simple single temperature model should be accurate.

The points in Figure 16 show the correlation function of galaxies with magnitude $17 < b'_j < 20$ where b'_j is the magnitudes after correcting for obscuration using the I_{100} estimate. The solid line plotted in Figure 16 is the same as in Figure 2a, and it can be seen that the changes introduced by the correction are very small.

We have estimated the covariance function of the obscuration by making a map of the predicted extinction over the area that we use for our correlation function estimates. We then calculated $w_{obsc} = \langle A_i A_j \rangle$, where A_i is the mean obscuration in cell i of the map. This is plotted in Figure 17, and it corresponds to the error introduced in the observed galaxy correlation function by the obscuration. It can be seen that the effect of Galactic extinction is less than 10^{-3} on all angular scales.

3.4.2 Atmospheric Extinction

The UK Schmidt Telescope is situated at latitude -31° and the southernmost plates in the survey are centred at -70° . The survey plates were exposed as they cross the meridian, so the airmass for the most southerly plates is 1.28. Using $A_V = 0.11 \sec(z)$, $A_B = 0.27 \sec(z)$ and $B_J = B - 0.28(B - V)$, the predicted maximum extinction is only ~ 0.06 magnitudes relative to the zenith. In fact all but 13 out of the 185 plates are centred at $\delta \geq -60^\circ$ and thus have an airmass ≤ 1.14 , so the atmospheric extinction for most fields is smaller than 0.02 magnitudes. The variation in galaxy density introduced by this effect is smaller than the variations caused by real structure in the galaxy distribution. This can be seen in Figure 18 which shows galaxy density as a function of δ before and after correcting the magnitudes for atmospheric extinction.

3.4.3 Stellar Contamination Gradient

The increase in the number of stars towards the Galactic plane leads to a gradient in the number of blended stellar images which contaminate the galaxy sample. After applying the extinction corrections described above, this Galactic gradient is seen as an apparent increase in galaxy density towards lower latitudes. In Figure 19 we plot the apparent surface density of galaxies as a function Galactic latitude, b , and this shows that the change in mean density from the Galactic pole to $|b| = 40^\circ$ is 10%. This variation is consistent with our visual classification checks at different Galactic latitudes, which showed the contamination is $\sim 5\%$ near the pole, and $\sim 15\%$ at $|b| = 40^\circ$. The change is not a simple linear gradient: for $|b| \gtrsim 50$ the density is essentially constant, but there is a significant rise in the density for $40 < |b| < 50$. This reflects the rather sharp increase in stellar density as we start to look through the Galactic bulge. In the area of sky used for our best correlation function estimates ($|b| \gtrsim 50^\circ$), there is almost no gradient, even with no further correction.

The surface density of contaminating stellar blends, N_{blend} , is approximately proportional to the square of the density of stars, N_{stars} . We can therefore use a map of stellar density to estimate the number of contaminating images, and so calculate a correction to the equivalent galaxy map. We determine the relation between the N_{blend} and N_{star} empirically by considering the mean surface density of “galaxies + contaminating blends”, $N_{tot} = N_{gal} + N_{blend}$ as a function of N_{stars} . Since there should be no correlation between the number stars and the number of true galaxies, any correlation must be due to contaminating images. The scatter plot of the apparent number of galaxies (N_{tot}) against the number of stars is shown in Figure 20. To produce this plot we created 512×512 pixel maps of the number of galaxies and the number of stars in $0.23^\circ \times 0.23^\circ$ cells, using an equal area projection centred on the South Galactic Pole. The large scatter in the number of galaxies per cell is caused by the clustering of the galaxy distribution. The dashed line in the figure

shows the mean galaxy density as a function of stellar density, and as expected there is an increase in N_{tot} at higher values of N_{star} . The solid line in the figure is a quadratic fit to the mean of N_{tot} as a function of N_{star} . We use this fit to estimate the change in N_{blend} as a function of N_{star} , and by subtracting this from the raw galaxy map we produce a corrected galaxy map. Figure 21 shows the corrected density of galaxies as a function of Galactic latitude, and there is no longer any significant gradient.

3.4.4 The overall effect of extinction and gradient corrections.

Figure 22 shows the angular correlation function of the final map of galaxies with $17 < b_J < 20.0$, corrected for mean atmospheric and galactic extinction, and the contamination by blended stars. It is almost indistinguishable from the correlation function of the uncorrected galaxy map, which is shown as the solid line in the figure. This is not surprising, because the main effect of both extinction and contaminating images, is to introduce a gradient in number of galaxies as a function of galactic latitude. Since the gradients are of opposite sign and nearly equal amplitude they almost exactly cancel.

These effects are very small, and the uncertainty in the overall correction is as large as the correction itself. Therefore we feel that the accuracy of the corrected $w(\theta)$ estimate is not significantly better than the uncorrected estimate. To keep our analysis as simple as possible we decided to exclude the low latitude part of the survey where these effects may be significant. For the 120 high latitude fields used in our best $w(\theta)$ estimates, the corrections are completely negligible.

3.5 Magnitude dependent errors

The discussion of errors in the previous sections are based mainly on the galaxies to a limit of $b_J = 20.0$, but since we also measure clustering as a function of magnitude, we have investigated magnitude-dependent errors. Possible sources of magnitude-dependent error include contamination by merged stars, incompleteness of the galaxy sample, and emulsion saturation.

Table 4 shows various estimates of the plate-matching errors, measured for each half-magnitude slice. The variance of the overlap residuals ϵ^2 and the inter-intra-plate offset are model independent ways to quantify the matching errors. The values of σ^2 , β_{ii}^2 and β_{ij}^2 are derived quantities dependent on assumptions concerning the propagation of errors across the plate network. In Table 4 we we have used the simple analytic model of equations (17) and (19). The inter-intra-plate offset gives an estimate of errors that is independent of the

Table 4: Magnitude dependence of photometric errors

magnitude range	ϵ^2	σ^2	β_{ii}^2	β_{ij}^2	$\langle w_{\text{intra}} - w_{\text{inter}} \rangle$
17.1 – 17.7	0.92×10^{-3}	1.5×10^{-3}	0.70×10^{-3}	0.32×10^{-3}	7.5×10^{-3}
17.7 – 18.3	1.40×10^{-3}	2.3×10^{-3}	1.07×10^{-3}	0.49×10^{-3}	6.0×10^{-3}
18.3 – 18.9	2.24×10^{-3}	3.7×10^{-3}	1.70×10^{-3}	0.78×10^{-3}	6.1×10^{-3}
18.9 – 19.5	2.38×10^{-3}	4.0×10^{-3}	1.81×10^{-3}	0.82×10^{-3}	3.1×10^{-3}
19.5 – 20.0	2.48×10^{-3}	4.1×10^{-3}	1.89×10^{-3}	0.86×10^{-3}	1.6×10^{-3}
20.0 – 20.5	1.88×10^{-3}	3.1×10^{-3}	1.43×10^{-3}	0.65×10^{-3}	3.8×10^{-3}

Notes: The second column gives ϵ^2 estimated from the plate-overlap residuals (equation 15). The third column gives σ^2 determined from this assuming the overlap errors are uncorrelated (equation 14). The next two columns give estimates of β_{ii}^2 and β_{ij}^2 from equations (17) and (19). The final column gives the observed offset between the intra- and inter-plate angular correlation functions measured for each magnitude slice.

overlap residuals, but the relation to an overall error correlation function depends on which error model is assumed, as described in Section 3.1.

The residual errors in the overlaps for the magnitude matching are essentially constant as a function of magnitude. This is good evidence that the magnitude errors do not vary as a function of magnitude. Since the overlap errors depend on the precision of the field corrections for each plate, the constant value of the residuals suggests that the field corrections are just as accurate at bright magnitudes as at faint magnitudes.

The observed offsets between intra- and inter-plate estimates of $w(\theta)$ do increase as a function of magnitude. As mentioned in Section 3.1.2, the cosmic variance in the estimated offset is large for a realistic clustered galaxy distribution. Nevertheless, it may be considered worrying that the offsets for all 6 slices are positive at about the 1σ level. We therefore investigated the dependence of the offsets in the Soneira-Peebles simulations described in Appendix A1 by selecting samples with different magnitude limits from each realization. The variance in offsets for brighter magnitude limits increased roughly in proportion to the amplitude of the correlation function. Also, for a particular realization, the offsets for different magnitude limits are highly correlated. This might have been expected, since features in the distribution that are correlated with plate boundaries at one magnitude limit will be correlated at other magnitude limits as well. The observed APM offsets thus follow the model predictions *ie.* they increase roughly in proportion to the amplitude of $w(\theta)$, remaining about 1σ positive for all magnitudes ranges brighter than $b_J = 20$.

The exception is the $20.0 < b_J < 20.5$ slice, where the offset is 3.8×10^{-3} ; much larger than expected from the magnitude errors and the cosmic variance. The reason for this is that star-galaxy classification breaks down near the magnitude limit of the survey. The completeness is fairly constant at 90% for samples brighter than $b_J = 20.3$, but rapidly drops for galaxies fainter than this, reaching a mean of 75% for galaxies with $20.4 < b_J < 20.5$. The incompleteness becomes significant first in the vignettted corners of each field, producing errors like the mode (C) simulations described in Section 3.1.2, which lead to a large offset. Nevertheless, even for this worst case the errors are not large enough to hide the break in $w(\theta)$.

3.6 Best estimates for $w(\theta)$

We correct for the residual matching errors by simply subtracting our estimated error correlation function (plotted as the solid line in Figure 9) from the raw $w(\theta)$ measurements. Except for the faintest slice, the matching errors are very nearly constant as a function of magnitude, so we use the same amplitude for the errors. For the faintest slice the variations in completeness become significant, so the errors from the magnitude matching do not represent the full errors. Since the offset for this slice is larger than the cosmic variance introduced by clustering, we can use the observed offset to estimate the overall matching errors. We therefore scaled the error correlation function to match the observed offset, and subtracted this from the measured $w(\theta)$. To account for the contaminating fraction of stellar images, each slice has also been multiplied by a factor $1/(1-f)^2$, where f is the fraction of stellar image misclassified as galaxies and varies from 4% for the brighter magnitudes, to 15% at the faintest limit. This correction has a significant effect on the amplitude of the correlation functions but does not change their shape. As mentioned in Section 3.4.4, the corrections for extinction and merger gradients are completely negligible for the high latitude fields that we use.

Figure 23 shows the final error-corrected correlation functions. At first sight they are not very different to those shown in Figure 3, but careful inspection shows that the results for faintest slice no longer cross the next brighter slice. This is the only significant change introduced by the exhaustive error analysis of this Section.

The various tests presented in this Section do not reveal any additive source of error which can increase the observed $w(\theta)$ by more than $1 - 2 \times 10^{-3}$ at $\theta = 0$. Some effects are likely to introduce correlated errors, but these rapidly decrease at larger scales, with an expected amplitude of $\sim 5 \times 10^{-4}$ on scales $\theta \sim 5^\circ$, and $\sim 2 \times 10^{-4}$ at $\theta \sim 10^\circ$. Over most of the angular scales we consider, this means that the observed $w(\theta)$ is more than 100 times the amplitude of our estimated errors. Even at the largest scales, where our results have fallen below the power law extrapolation, the amplitude of $w(\theta)$ for the different slices

varies between $4 - 11 \times 10^{-3}$. This means that the estimated signal to noise at the break angle (see Section 4.1.3 for our definition of break angle), varies from about 5 for the faintest magnitude slice, to 40 for the brightest magnitude slice.

We can be very confident that we have not significantly *underestimated* $w(\theta)$. It is extremely unlikely that there are errors that have avoided detection in our tests and that have conspired to eliminate intrinsic galaxy correlations. Also, for these estimates of $w(\theta)$ we have not applied any filtering to remove clustering. In Section 4.2.3 we consider the effect of explicitly removing smooth fitting functions and conclude that these filtered measurements are much poorer estimates of the real correlation function.

4. The Scaling Test and Comparisons with other Catalogues

In this section we first test if our best estimates of $w(\theta)$ scale with magnitude as predicted by Limber’s equation. This is an important test that must be satisfied if our measurements really represent the projected clustering of the three-dimensional galaxy distribution. We then use the scaling relations to compare our measurements to the Lick catalogue, and other more recent surveys. Although there are apparent discrepancies between $w(\theta)$ from some of these surveys, we find that the measurements are consistent to within the errors associated with each survey.

4.1 Limber’s equation and the scaling test

4.1.1 Limber’s equation

As mentioned in Section 2.4, the variation of $w(\theta)$ as a function of magnitude allows us to check that the angular correlation functions measure intrinsic clustering rather than systematic errors. If $w(\theta)$ is determined by the projection of the true spatial correlation function, $\xi(\mathbf{r})$, rather than by systematic errors in the catalogue, the shape of $w(\theta)$ as a function of magnitude limit can be calculated from the relativistic version of Limber’s equation (GP77, Phillipps *et al.* 1978, Peebles 1980 §56),

$$w(\theta) = \frac{\int_0^\infty \int_0^\infty r_1^2 r_2^2 p(r_1) p(r_2) \xi(r_{12}, z) dr_1 dr_2}{\left[\int_0^\infty r^2 p(r) dr \right]^2}, \quad (31)$$

where $r_{12} = |\mathbf{r}_1 - \mathbf{r}_2|$ and $p(r)$ is the selection function, which gives the fraction of galaxies at proper distance r in the magnitude limited sample.

If we assume that $\xi(r, z)$ is a power law in r and redshift z ,

$$\xi(r, z) = \left(\frac{r_0}{r} \right)^\gamma (1 + z)^{-(3+\epsilon)} \quad (32)$$

and we adopt the small angle approximation $r_1 \approx r_2 \gg r_{12}$, equation (31) can be rewritten as

$$w(\theta) = \sqrt{\pi} \frac{\Gamma[(\gamma - 1)/2]}{\Gamma(\gamma/2)} \frac{B}{\theta^{\gamma-1}} r_0^\gamma, \quad (33a)$$

where

$$B = \frac{\int_0^\infty x^{5-\gamma} a^6 p^2(x) (1+z)^{(\gamma-3-\epsilon)} F(x)^{-1} dx}{\left[\int_0^\infty x^2 a^3 p(x) F(x)^{-1} dx \right]^2}. \quad (33b)$$

In equation (33b) a is the cosmological scale factor normalized to unity at the present epoch, x is the coordinate distance at redshift z ,

$$x = (2c/H_0)[(\Omega_0 - 2)(1 + \Omega_0 z)^{1/2} + 2 - \Omega_0 + \Omega_0 z]/[\Omega_0^2(1 + z)], \quad (34a)$$

for a Friedman-Robertson-Walker universe with zero cosmological constant and present day density parameter Ω_0 (see Peebles 1980, §56); the factor

$$F(x) = [1 - (H_0 x/c)^2 (\Omega_0 - 1)]^{1/2}, \quad (34b)$$

comes from the metric and is equal to unity for a spatially flat universe.

Equation (33b) can be written in terms of the redshift distribution of galaxies in the sample, dN/dz ,

$$B = \frac{\int_0^\infty x^{1-\gamma} \left(\frac{dN}{dz}\right)^2 F(x) (1+z)^{(\gamma-3-\epsilon)} \left(\frac{dz}{dx}\right) dz}{\left[\int_0^\infty \left(\frac{dN}{dz}\right) dz \right]^2}, \quad (35a)$$

(Efstathiou *et al.* 1991), since dN/dz is related to the selection function by

$$\left(\frac{dN}{dz}\right) dz \propto x^2 a^3 \frac{p(x)}{F(x)} \left(\frac{dx}{dz}\right) dz. \quad (35b)$$

Thus, we can evaluate equations (33b) and (35b) if we have a model of the selection function $p(x)$ derived *e.g.* from the galaxy luminosity function, or directly from the redshift distribution of a representative subset of APM galaxies to a specified magnitude limit. Models for the selection function will be described in the next subsection.

The model for the evolution of the spatial correlation function (equation 32) is simplistic and may well not apply over a wide range of redshifts and spatial scales (see Efstathiou *et al.* 1991, Efstathiou 1995b). The value $\epsilon = 0$ corresponds to stable clustering in physical coordinates, which may be applicable at small separations where $\xi \gg 1$ and most galaxy pairs are in bound and stable systems (Peebles 1980 §73); the value $\epsilon = -1.3$ corresponds to a constant amplitude of ξ in comoving coordinates for a power law correlation function with slope $\gamma = 1.7$. In Section 4.1.3 we will illustrate the sensitivity of our results to uncertainties in the evolution of ξ and to cosmological parameters.

4.1.2 Model for the selection function

In Maddox *et al.* (1990c) we constructed a model for the selection function $p(x)$ derived from the galaxy luminosity function. We reproduce the model here for reference. The selection function for a magnitude slice $m_{min} \leq b_J \leq m_{max}$ is given by

$$a^3 p(x) \propto \int_{\ell_{min}(x)}^{\ell_{max}(x)} \varphi(\ell, z) d\ell, \quad (36a)$$

where $\phi(\ell, z) d\ell$ is the galaxy luminosity function at redshift z and

$$\ell_{min/max}(x) = \text{dex}\{0.4(M_{b_J}^*(z) - (m_{max/min} - 25 - 5 \log[x(1+z)]))\}, \quad (36b)$$

and $M_{b_J}^*$ is the characteristic absolute magnitude of the Schechter (1976) luminosity function at redshift z . The model of $\phi(\ell, z)$ adopted by Maddox *et al.* (1990c) is

$$\begin{aligned} \varphi(\ell, z) d\ell &= \varphi^* \ell^\alpha \exp(-\ell) d\ell, \quad \ell \equiv 10^{0.4(M_{b_J}^* - M)}, \quad (37) \\ M_{b_J}^*(z) &= M_0^* + M_1^* z, \quad \alpha(z) = \alpha_0 + \alpha_1 z, \\ \varphi^* &= 1.3 \times 10^{-2} h^3 \text{Mpc}^{-3}, \\ M_0^* &= -19.8 + 5 \log(h), \quad M_1^* = 1, \quad \alpha_0 = -1, \quad \alpha_1 = -2. \end{aligned}$$

Note that equation (3) of Maddox *et al.* (1990c) contains a misprint in the definition of ℓ . This parametric form is intended to model the evolution of the galaxy luminosity function (including the k -correction) and to be consistent with the following observations: (a) The low redshift field galaxy luminosity function (Efstathiou *et al.* 1988, Loveday *et al.* 1992a); (b) The galaxy number counts from the APM Survey (Maddox *et al.* 1990d) and from deeper CCD surveys (*e.g.* Tyson 1988, Cowie *et al.* 1988, Metcalfe *et al.* 1995); (c) The redshift distribution in the deep spectroscopic survey of Broadhurst *et al.* (1988). (d) Constraints on the evolution of the luminosity function determined from the Broadhurst *et al.* survey (see Maddox 1988, and Gaztanaga 1995). Note that the normalization of the luminosity function, ϕ^* , cancels in Limber's equation.

There has been a large increase in the number of faint galaxy redshifts in the last few years and so it has become possible to constrain the selection function of the APM Survey by direct comparison with the redshift distribution of magnitude limited samples. R.S. Ellis has kindly made available to us a list of 697 galaxy redshifts in 21 small fields. These fields have magnitude limits that lie approximately within one of the three ranges $17 < B < 19.7$, $19.7 < B < 20.3$ and $20.3 < B < 21.5$. The fields include the redshifts measured by Broadhurst *et al.* (1988), Colless *et al.* (1990, 1993) and unpublished redshifts. The sample is a subset of the data used by Cole *et al.* (1994a) to study the spatial clustering of faint galaxies. We correlated the galaxy positions on each field with the APM Survey and computed a mean magnitude offset to convert from the B magnitudes used in the redshift survey into the APM b_J system. We then used the completeness factors, sampling rates and areas to weight each field and so computed a redshift distribution within a specified APM magnitude slice. The results are shown in Figure 24 for the magnitude slices $17 \leq b_J \leq 19$,

$17 \leq b_J \leq 20$ and $17 \leq b_J \leq 21$. In each case, the histograms have been normalized to the actual (*i.e.* unweighted) number of galaxies N_g in each magnitude slice, as listed in the Figure.

The dashed lines in Figure 24 show the redshift distributions computed from the Maddox *et al.* (1990c) model of equation (37). The median redshifts predicted by this model are slightly too high and the model predicts more high redshift galaxies than are observed. The solid lines in Figure 24 show redshift distributions in magnitude slices computed from the distribution

$$\left(\frac{dN}{dz}\right) dz \propto \frac{10^{0.45m}}{z_c^3} z^2 \exp\left[-\left(\frac{z}{z_c(b_J)}\right)^{3/2}\right] dz, \quad (38a)$$

where the median redshift is given by

$$z_m(b_J) = 0.016(b_J - 17)^{1.5} + 0.046 \quad b_J \geq 17 \quad (38b)$$

$$z_m(b_J) = 1.412z_c. \quad (38c)$$

This model was introduced by Baugh & Efstathiou (1993) and the specific parameters were chosen to match the redshift distributions of the $b_J = 17.15$ limited Stromlo/APM redshift survey (Loveday *et al.* 1992a,b) and of the Broadhurst *et al.* (1980) and Colless (1990, 1993) surveys, which are a subset of the data plotted in Figure 24. As Figure 24 shows, equation (38) provides an excellent match to the empirically determined redshift distributions. In the next subsection, we will evaluate Limber's equation using the models of equations (37) and (38) to illustrate the sensitivity of the results to errors in the model for the selection function. However, it is worth emphasizing that the predicted amplitude of $w(\theta)$ depends mainly on the median redshift of the sample, which is well determined from the redshift surveys rather than on the precise shape of the redshift distribution.

4.1.3 Application of the scaling test

In this subsection we evaluate Limber's equation to scale the angular correlation functions for the six magnitude slices plotted in Figure 23 to a common depth. As a reference depth, we have chosen to scale the angular correlation functions to a magnitude limit of $b_J = 18.4$. At this magnitude limit, the galaxy counts in the APM Survey are about equal to those in the Lick survey, thus our scaling will transform each of the $w(\theta)$ estimates in Figure 23 to about the same depth as the Lick catalogue.

For each magnitude slice, we compute the shifts $\delta \log \theta$, $\delta \log w(\theta)$ required to transform the angular correlation functions to the Lick depth, assuming a two power model for $\xi(r)$ with a slope $\gamma_1 = 1.7$ at small separations (equation 12) and a slope $\gamma_2 = 3.0$ at large separations (see GP77, Figure 15, for an explanation of how these shifts are computed in the two power-law model). The results are listed in Table 5. The scaling factors are relatively insensitive to the evolution parameter ϵ in equation (32) and to the cosmological model, as expected at the low redshifts of the APM survey. The scaling factors are more

sensitive to the model for the redshift distribution, though even for redshift distributions as different as the two models adopted here, the scaling factors do not differ by more than 0.03 in the log. In the rest of this subsection, we use the scaling factors in the fourth and fifth columns of Table 5 based on equation (38), since this provides a good fit to the observed redshift distributions (Figure 24), and assuming $\epsilon = 0$ and $\Omega = 1$,

Figure 25 shows the six $w(\theta)$ estimates from Figure 23 scaled to the the Lick depth. The agreement between these curves is excellent. The rms scatter in the mean of the 6 slices sample using 80 logarithmically-spaced bins in θ is only 4.5%. The agreement between the six magnitude slices is better than plotted in Figure 2b of Maddox *et al.* (1990c) for two reasons. Firstly, the model of the redshift distribution (38) is more accurate than the model of equation (37) used by Maddox *et al.* (1990c), and this improves the accuracy of the scaling correction. Secondly, the corrected $w(\theta)$ for the faintest magnitude slice has a lower amplitude at large angles (*c.f.* Figures 3 and 23) and this again improves the agreement of the scaling test. The improvement in the accuracy of the scaling test supports our error analysis of the previous sections which indicates that systematic errors are significant only close to the magnitude limit of the survey. The scaling test thus provides strong evidence that our angular correlation functions are measuring real clustering in the galaxy distribution.

Table 5: Scaling factors to Lick depth

mag range	(equation 37)		($\epsilon = 0, \Omega = 1$)		(equation 38)		($\epsilon = -1.3, \Omega = 1$)		($\epsilon = 0, \Omega = 0$)	
	$\delta \log \theta$	$\delta \log w$	$\delta \log \theta$	$\delta \log w$	$\delta \log \theta$	$\delta \log w$	$\delta \log \theta$	$\delta \log w$	$\delta \log \theta$	$\delta \log w$
17.1 – 17.7	0.038	-0.117	0.015	-0.114	0.013	-0.112	0.016	-0.116	0.016	-0.116
17.7 – 18.3	0.125	-0.021	0.143	-0.046	0.141	-0.054	0.147	-0.043	0.147	-0.043
18.3 – 18.9	0.205	0.071	0.230	0.057	0.230	0.037	0.237	0.064	0.237	0.064
18.9 – 19.5	0.280	0.159	0.303	0.164	0.303	0.132	0.311	0.176	0.311	0.176
19.5 – 20.0	0.341	0.233	0.358	0.254	0.359	0.210	0.367	0.272	0.367	0.272
20.0 – 20.5	0.393	0.299	0.402	0.333	0.403	0.276	0.412	0.355	0.412	0.355

Another way of demonstrating the accuracy of the scaling relation is shown in Figures 26a and 26b. For each of the magnitude slices we have fitted a power law $w(\theta) = A\theta^{1-\gamma}$ over the angular range $0.01^\circ \leq \theta \leq 1^\circ$, with the slope $\gamma = 1.7$. The resulting amplitudes are plotted against the corresponding magnitude limit in Figure 26a. The line in Figure 26a shows the predicted variation from the model of equation (38) with $\epsilon = 0$ and $\Omega = 1$ assuming a slope $\gamma = 1.7$ and normalizing the amplitude of ξ to minimize the *rms* residuals about the line. The amplitude of the faintest slice is about 8% lower than predicted by the model. As explained in Section 3.6, the overall normalization of $w(\theta)$ for the faintest slice is uncertain because of residual contamination by stars, but this is unlikely to introduce errors larger than 5%. Thus the discrepancy in the scaling may be marginally significant and may

indicate the start of a decline away from the model predictions that has been found from deeper photographic and CCD surveys (Efstathiou *et al.* 1991; Neuschaefer, Windhorst and Dressler 1991, Pritchett and Infante 1992, Roche *et al.* 1993, Neuschaefer and Windhorst 1995).

In Figure 26b we plot the characteristic break angle θ_{break} as a function of limiting magnitude against the predictions of the two power-law model. We define the break angle as the angle at which the measured $w(\theta)$ has fallen to half the value expected by extrapolating the power law fitted at smaller angular scales as described above. The break angles decrease at fainter magnitudes in good agreement with the model predictions. This provides strong evidence that the break from a power-law is a real feature of the galaxy distribution. Figure 26b contradicts the claim by F92 that the scaling of $w(\theta)$ measured from the APM survey is well approximated by a shift only in amplitude. It shows that a combination of shifts in amplitude and angle is seen, as expected if the break in $w(\theta)$ is associated with a physical feature in the shape of $\xi(r)$.

It is also interesting to compute the amplitude of $\xi(r)$ implied by Limber's equation. Using the redshift distribution of equation (38) and assuming a power law $\gamma = 1.7$, the parameters of the angular correlation function for the magnitude slice $17 \leq b_J \leq 20$ of equation (12) give a correlation length r_0 (equation 32) of

$$r_0 = 4.81 \pm 0.28 \text{ h}^{-1}\text{Mpc} \quad (\epsilon = 0, \Omega_0 = 1) \quad (39a)$$

$$r_0 = 4.43 \pm 0.26 \text{ h}^{-1}\text{Mpc} \quad (\epsilon = -1.3, \Omega_0 = 1) \quad (39b)$$

$$r_0 = 5.05 \pm 0.29 \text{ h}^{-1}\text{Mpc} \quad (\epsilon = 0, \Omega_0 = 0) \quad (39c)$$

These numbers are in good agreement with the correlation length of $r_0 \approx 4.7 \text{ h}^{-1}\text{Mpc}$ determined by GP77 from the Lick survey, with the correlation lengths of $\sim 5 \text{ h}^{-1}\text{Mpc}$ determined from the CfA-2 (Park *et al.* 1994) and Stromlo-APM (Loveday *et al.* 1995) redshift surveys (though redshift space distortions, Kaiser 1987, complicate the comparison with redshift surveys as described in Section 5 below). Notice that the statistical uncertainty in the amplitude of $\xi(r)$ implied by equation (12) corresponds to only 6% in r_0 and is smaller than the error of about 15% arising from uncertainties in the evolution of ξ and the cosmological model, which are probably slightly larger than the residual errors arising from uncertainties in the shape of the redshift distribution.

4.2 Comparison with $w(\theta)$ from other surveys

4.2.1 Small area surveys

Several groups have used small area surveys to estimate $w(\theta)$. Measurements of small numbers of Schmidt and 4m plates have produced galaxy surveys covering a few hundred square degrees to a limit $b_J \sim 20$ and a few square degrees to a limit of $b_J \sim 23$ (Sebok 1986, Pritchett and Infante 1986, Koo and Szalay 1984, Stevenson *et al.* 1985, Hewett 1982, Shanks *et al.* 1980). The results from these surveys show power-law behaviour in $w(\theta)$ on small angular scales, with a sharp break at larger angles. The power-law slope of

the estimated correlations functions are fairly consistent, varying between ~ -0.7 and -0.8 . The corresponding amplitudes of $w(\theta)$, however, show a large scatter. Cosmic variance alone will introduce a large scatter in the amplitude of $w(\theta)$ determined from a small number of Schmidt plates. This can be seen from the simulations described in Appendix A and from the scatter in the single-plate $w(\theta)$ estimates from the APM Survey described in Section 2.2.

The break in $w(\theta)$ from a power law seen in all these surveys is caused by the integral constraint in the estimator of $w(\theta)$, as discussed in Section 2.2. This effect also explains why the slopes of power law fits to $w(\theta)$ from small samples are slightly steeper than the fits to our $w(\theta)$ measurements described in Section 2.2. One of the most important results from our analysis of the APM Survey is the demonstration that large areas of sky are required to determine $w(\theta)$ reliably on angular scales of a few degrees. This point is discussed further in the next subsection.

4.2.2 Comparison with the Edinburgh-Durham catalogue

As mentioned in the introduction, the Edinburgh-Durham Southern Galaxy Catalogue (EDSGC) is the largest machine constructed catalogue of comparable size to the APM Galaxy Survey. It is based on the same photographic plate material as the APM Survey scanned with the COSMOS measuring machine, but comprises only 60 plates centred on the South Galactic Pole, *i.e.* about one-third of the area of the APM Galaxy Survey. The EDSGC is described by Heydon-Dumbleton *et al.* (1989). Estimates of $w(\theta)$ from the EDSGC have been presented by Collins *et al.* (1989, 1992), and an analysis of errors in the $w(\theta)$ estimates from the EDSGC is described by Nichol & Collins (1993).

In Figure 27, we compare the EDSGC estimates of $w(\theta)$ at a magnitude limit of $b_J = 19.5$ with the APM estimates for the magnitude slice $17 < b_J < 20$. We have corrected for the small difference in limiting magnitudes by scaling the EDSGC results to the APM depth using the model of equation (38) with $\epsilon = 0$ and $\Omega_0 = 1$. The open circles in Figures 27 show the uncorrected estimates of $w(\theta)$ for the EDSGC from Figure 2 of Collins *et al.* (1992). The solid points in Figure 27a are the means of the APM $w(\theta)$ estimates from 4 approximately equal area zones in the survey. Notice that the open circles lie above the APM estimates at $\theta \gtrsim 1^\circ$. The discrepancy between these estimates is probably caused by the larger calibration errors of the EDSGC.

Collins *et al.* (1992) show that the dispersion in the plate overlap residuals in the EDSGC is about $\epsilon = 0.08$ magnitudes. The EDSGC matching procedure is not based wholly on plate overlaps, and so our analysis of Section 3.1 cannot strictly be used to relate the overlap residuals to a plate zero-point error. A reasonable approximation for the EDSGC is that $\beta_{ii}^2 \sim 0.5\epsilon^2 = 3.2 \times 10^{-3}$, *i.e.* about twice the value measured for the APM Survey. Larger calibration errors in the EDSGC are plausible because they use a less accurate technique for correcting for plate field effects, and because they use CCD sequences with rather few galaxies to determine the the plate correction factors for about half the survey, rather than using the plate overlaps.

Nichol and Collins (1993) have analyzed the effects of plate matching errors in the EDSGC survey using simulations. Their simulations do not include the effects of the propagation of errors, which we discussed in detail in Section 3, since they make extensive use of calibrating photometry and this should limit the large-scale propagation of errors. As seen in Figure 3 of Nichol and Collins (1993), the resulting error correlation function has a high amplitude on scales less than the size of a plate, $\theta \lesssim 5^\circ$, but the errors do not propagate to larger scales. The dotted lines in Figure 27 show the EDSGC $w(\theta)$ after correcting for plate errors and for the effects of variable Galactic obscuration (although plate matching errors dominate the correction). The dotted line is in much closer agreement with the APM points, though it lies slightly higher on angular scales greater than $\sim 2^\circ$.

Figure 27b shows the individual estimates of $w(\theta)$ for each of the 4 roughly equal area zones of the APM Survey plotted together with the uncorrected and corrected EDSGC $w(\theta)$. Each of the 4 APM zones has about the same area as the EDSGC, hence Figure 27b gives a good indication of the sampling errors for a catalogue of the size of the EDSGC. The $w(\theta)$ estimates for the 4 zones show a large scatter, especially at $\theta \gtrsim 4^\circ$, showing that a large area of sky is required to determine $w(\theta)$ accurately at amplitudes $\lesssim 10^{-2}$. The corrected EDSGC estimates of $w(\theta)$ lie within the scatter of the 4 APM zones, hence we conclude that the corrected EDSGC estimates of $w(\theta)$ are consistent with ours within the sampling fluctuations. Since the EDSGC catalogue is based on the same photographic material as the APM Survey, it is possible to make a detailed image-by-image comparison of the two surveys. Such an analysis is in progress and will be described in a future paper.

4.2.3 Comparison with the Lick survey and the effects of filtering the APM catalogue

The Lick survey samples a large enough area of sky that sampling fluctuations and biases in the estimates of $w(\theta)$ caused by the integral constraint should be relatively small. Thus $w(\theta)$ from the Lick survey should be comparable to the estimates of $w(\theta)$ derived from the APM Survey. Figure 28 shows the GP77 estimates of $w(\theta)$ for the Lick catalogue compared to the APM $w(\theta)$ estimates for the magnitude slice $17 \leq b_J \leq 20$. The APM $w(\theta)$ has been scaled to the Lick depth as described in Section 4.1.2. Figure 28a shows the GP77 estimates derived from four separate zones of the Lick catalogue which were filtered to remove large scale gradients in the galaxy counts (see GP77, Section III). The Lick $w(\theta)$ is in excellent agreement with the APM results on angular scales less than $\theta \approx 3^\circ$. On larger angular scales our results disagree. GP77 find that $w(\theta)$ breaks sharply from a power law on scales of $\sim 3^\circ$, whereas we find a more gentle decline.

The most likely reason for this discrepancy is that the GP77 filtering of the Lick map has removed a component of intrinsic clustering. In Figure 28b we compare the APM $w(\theta)$ to the unfiltered $w(\theta)$ from the Lick survey from Figure 2 of GP77. The results from the unfiltered Lick map lie slightly higher than the APM $w(\theta)$ on large angular scales. Evidently, filtering has a large effect on the Lick angular correlation function and could account for the discrepancy with the APM $w(\theta)$.

Seldner *et al.* (1977) find that the mean square error in the fractional galaxy count in a single plate overlap after applying the Lick plate correction factors is $\sigma^2 = 0.025$, *i.e.* about eight times larger than for the APM Survey (equation 16). As described by GP86 and in Section 3.1, these plate matching errors propagate through the network of plates and introduce large-scale gradients in the corrected Lick counts. GP86 estimate that the Lick plate matching errors lead to a variance in the counts on a single plate of $\beta_{ii}^2 = 0.0127$ (*c.f.* equation 17). Subtracting the contribution $4\sigma^2/25$ caused by plate-to-plate errors GP86 conclude that large-scale gradients caused by plate matching errors introduce a variance of 0.0087 in the Lick counts. However, GP86 fit a polynomial map to the Lick counts which has a variance of 0.0194, more than twice the predicted value, hence it is plausible that the filtering has removed a component of real clustering in the galaxy distribution in addition to large-scale gradients in the counts caused by plate matching errors.

To summarize, the expected errors in the Lick $w(\theta)$ arising from errors in the plate matching are $w_{err} \sim 10^{-2}$, about an order of magnitude larger than the errors estimated for the APM survey. This estimate of the Lick errors is of the same order as the differences seen between the APM and Lick angular correlation functions and between the angular correlation functions estimated from the filtered and unfiltered Lick maps. We conclude, therefore, that it is difficult to disentangle real galaxy clustering on scales of a few degrees from artificial large-scale gradients in the Lick catalogue.

We have tested the effect of filtering the the APM Survey, by evaluating the correlation functions for our six magnitude slices after first subtracting a bicubic spline function fitted independently to the counts in each slice (see also Appendix A2). The results are shown in Figure 29. The estimates of $w(\theta)$ for the faintest slices change only slightly, but for the brighter slices the break steepens considerably. Figure 20b shows the filtered estimates of $w(\theta)$ scaled to the Lick depth as in Figure 25. The agreement between the scaled slices is significantly worse after spline fitting. The *rms* fractional variation of the spline fits is 1.5, 0.8, 2.5, 6.5, 13, 20×10^{-3} for the 6 slices in faint-to-bright order. As described in Section 3.5, it is extremely unlikely that our systematic errors are increasing this rapidly at brighter magnitudes, thus we conclude that the spline fits to the bright slices are dominated by true large-scale galaxy clustering and that the unfiltered APM results are close to the correct values.

GP77 argued that their $w(\theta)$ shows anticorrelation of only ≈ -0.004 at $\theta \sim 10^\circ$, therefore they could not have over-filtered $w(\theta)$ by much more than this amount. However, the results from spline fitting our maps show that the correlation function of the spline fits, $w_S(\theta)$, typically crosses zero at $\sim 20^\circ$, and that $w_S(10^\circ) \sim \frac{1}{2}w_S(0^\circ)$. It is therefore quite likely that GP77 have in fact underestimated $w(\theta)$ by as much as 0.008. It is clear from the above analysis that the GP77 smoothing functions are the main source of the apparent discrepancy between our results and theirs. For example, if we fit a spline function to our brightest magnitude slice (at approximately the Lick depth) or to the Soneira-Peebles simulations described in Appendix A, we obtain a very similar result to GP77.

4.2.4 A firm upper limit to errors in $w(\theta)$

A firm upper limit on all sources of error in our $w(\theta)$ measurements can be set from the angular correlation function of the faintest galaxies in the APM Survey. Any error that is approximately independent of magnitude will add the same error correlation function to each of the magnitude slices, so the observed $w(\theta)$ for the faintest slice provides an upper limit to these errors. Realistically we believe that the errors are more than an order of magnitude smaller than this, so this is gross overestimate of the most likely errors. Nevertheless, by assuming that *all* of the correlations in the faintest slice are caused by errors we can ‘correct’ the brighter slices by subtracting $w(\theta)$ of the faintest slice from the $w(\theta)$ of each of the brighter slices. Conceptually this subtraction is equivalent to finding a filter which removes all of the structure in the distribution of faint galaxies, and then applying the same filter to the distribution of the brighter galaxies.

After this subtraction the brighter galaxies still show strong clustering to large scales, as seen in Figure 30. The brightest three slices have such a high amplitude, that any errors and gradients of the same amplitude as those in the faintest slice are not significant. This rules out all sources of error which affect bright and faint galaxies equally. Given that there are no significant errors in the brighter slices, then the agreement between our best estimates of $w(\theta)$ after scaling suggests that errors are unlikely to be important even at faint magnitudes. Thus we are confident that the excess power relative to GP77 is real, especially for the brighter slices where the signal is much more than ten times larger than the estimated systematic errors.

To summarize, we believe that filtering of the APM Survey is unjustified for the following reasons:

- (i) The angular correlation functions of the faint slices show more power than the GP77 result even after filtering.
- (ii) The angular correlation functions for the filtered maps do not obey the scaling relation because the filtering affects mainly the $w(\theta)$ estimates from the brighter magnitude slices.
- (iii) Filtering simulated galaxy distributions that have the same $w(\theta)$ as measured from the APM Survey, but no plate-matching errors, removes large-scale power from the $w(\theta)$ estimates resulting in an artificial break in $w(\theta)$ similar to that found by GP77 for the filtered Lick maps (see Appendix A2).
- (iv) Subtracting $w(\theta)$ for the faintest slice from w for the brightest three slices does not change them significantly. Hence filtering is justified only if the systematic errors are unique to the brightest slices.

5. Cosmological Implications

In this Section we consider some implications of the angular correlation functions estimated in previous Sections. In Section 5.1, we compare our estimates of $w(\theta)$ with the angular correlation functions calculated from a family of cold dark matter (CDM) power spectra. In Section 5.2, we discuss the three-dimensional power spectrum derived by inverting $w(\theta)$ following the technique described by Baugh and Efstathiou (1993) and we compare the results with the power spectra determined from N-body simulations of several CDM-like models. We compare the APM power spectrum with the power spectra estimated from several redshift surveys in Section 5.3.

5.1 Angular correlations

The spatial two-point correlation function is the Fourier transform of the three-dimensional power spectrum $P(k)$ (equation 1). Thus, given a theoretical prediction for $P(k)$, we can compute the spatial correlation function ξ and hence $w(\theta)$ by integrating Limber's equation (31). In this subsection, we compare the APM $w(\theta)$ with the predictions of a family of CDM-like power spectra. According to linear perturbation theory, the present day power-spectrum of mass fluctuations in a CDM dominated universe arising from scale-invariant adiabatic fluctuations in the early universe is well approximated by the formula

$$P(k) = \frac{Bk}{(1 + [ak + (bk)^{3/2} + (ck)^2]^\nu)^{2/\nu}}, \quad (40)$$

$$a = (6.4/\Gamma) \text{ h}^{-1}\text{Mpc}, \quad b = (3.0/\Gamma) \text{ h}^{-1}\text{Mpc}, \quad c = (1.7/\Gamma) \text{ h}^{-1}\text{Mpc}, \quad \nu = 1.13.$$

Equation (40) is accurate to a few percent for spatially flat universes in which baryons make a negligible contribution to the total mass density (Bond & Efstathiou 1984). The parameter $\Gamma = \Omega_0 h$ defines a useful sequence of models with varying amounts of large-scale power (Efstathiou, Bond and White 1992). In the standard version of the CDM model (*e.g.* Blumenthal *et al.* 1984, Davis *et al.* 1985) $\Omega_0 = 1$ and $h \approx 0.5$, thus $\Gamma \approx 0.5$.

Figure 31 shows $w(\theta)$ computed from the power spectra (40) compared to the APM measurements for the magnitude slice $17 \leq b_J \leq 20$. We have adopted our standard model for the APM selection function (equation 38) and have assumed $\epsilon = 0$ and $\Omega_0 = 1$ in evaluation Limber's formula. Each curve in Figure 31 has been normalized so that the variance of the mass fluctuations in a sphere of radius $x_f = 8 \text{ h}^{-1}\text{Mpc}$,

$$\sigma^2(x_f) = \frac{V}{2\pi^2} \int_0^\infty P(k) W^2(kx_f) k^2 dk, \quad (41)$$

$$W(kx_f) = \frac{3}{(kx_f)^3} [\sin kx_f - kx_f \cos kx_f].$$

is equal to $(0.9)^2$. This normalization has been chosen so that each of the curves in Figure 31 passes through the APM data points at $\theta \approx 0.4^\circ$. The angular scale corresponding to a physical scale of $5 \text{ h}^{-1}\text{Mpc}$ at the median depth $d^* \approx 315 \text{ h}^{-1}\text{Mpc}$ of the sample is shown

by the arrow. Larger angular scales probe spatial separations at which $\xi(r) \lesssim 1$ (equation 39) and so typical mass fluctuations should be smaller than unity unless galaxies are strongly antibiased relative to the mass distribution.

The shape of the APM $w(\theta)$ at large angles is well approximated by equation (40) with Γ in the range 0.2 – 0.3, rather than the value $\Gamma = 0.5$ appropriate for the standard CDM. This is consistent with the results of previous papers (Maddox *et al.* 1990c, Efstathiou *et al.* 1990, Efstathiou 1993, Peacock and Dodds 1994). We make several points concerning this Figure:

- (i) The best fitting value of Γ in Figure 31 is slightly larger than the value $\Gamma \approx 0.2$ favoured in some of our earlier papers. This is because we compared the CDM models to the scaled results from the six magnitude slices plotted in Figure 3. The faintest slice is noticeably affected by systematic errors as described in earlier sections and this biases Γ to slightly lower values. In contrast, the effects of systematic errors on the estimates plotted in Figure 31 should be no larger than $\approx 10^{-3}$ in $w(\theta)$.
- (ii) The normalization of the CDM curves plotted in Figure 31 is arbitrary. In principle, we could raise the amplitude of the $\Gamma = 0.5$ curve in Figure 31 to fit the angular correlation function at $\theta \sim 5^\circ$ (this would require a normalization of $\sigma_8 \approx 1.6$) but the predicted $w(\theta)$ would then lie well above the data points on angular scale $\lesssim 2^\circ$.
- (iii) The points at $w(\theta)$ on scales $\gtrsim 1^\circ$ correspond to physical separations at which the mass fluctuations are likely to be in the weakly non-linear regime. Thus, it is possible that non-linearities may distort the shape of the power spectrum over much of the angular range plotted in Figure 31.

We discuss the last two points in more detail in the next subsection.

5.2 The power spectrum determined from the APM Survey

Baugh and Efstathiou (1993, hereafter BE) show that the three-dimensional power spectrum $P(k, z)$ is related to $w(\theta)$ by an integral equation

$$w(\varpi) = \int_0^\infty P(k) k g(k\varpi) dk, \quad \varpi = 2 \sin(\theta/2), \quad (42a)$$

where the kernel $g(k\varpi)$ is equal to

$$g(k\varpi) = \frac{\frac{1}{2\pi} \int_0^\infty \frac{F(z)}{(1+z)^\alpha} \left(\frac{dN}{dz}\right)^2 \left(\frac{dz}{dx}\right) J_0(k\varpi x) dz}{\left[\int_0^\infty \left(\frac{dN}{dz}\right) dz\right]^2}, \quad (42b)$$

and the time evolution of the power spectrum has been parameterized as

$$P(k, t) = \frac{P(k)}{(1+z)^\alpha}. \quad (42c)$$

In these equations k is defined as a comoving wavenumber, hence for a power law spatial correlation function of the form given in equation (32), the exponent α giving the time dependence of $P(k, t)$ is equal to $\alpha = 3 + \epsilon - \gamma$. In the analysis below, we set $\alpha = 1.3$, *i.e.* we assume that the small scale power-spectrum is constant in physical coordinates, consistent with the assumption $\epsilon = 0$ that we adopted to compute the scaling of $w(\theta)$ in Figure 25. Equation (42a) can be inverted using Lucy’s (1974) deconvolution algorithm to yield $P(k)$ from observations of $w(\theta)$. The technique is described in detail by BE. A similar technique, in which observations of the two-dimensional power spectrum are inverted to recover $P(k)$ is discussed by Baugh and Efstathiou (1994), together with an application to the two-dimensional power spectra measured from the APM Galaxy Survey.

Figure 32a shows the BE technique applied to the $w(\theta)$ estimates for the magnitude slice $17 \leq b_J \leq 20$. The kernel (42b) has been evaluated assuming $\Omega = 1$; BE discuss the sensitivity of the inversion to assumptions concerning the cosmological model and the evolution of $P(k)$, showing that these have little effect on the shape of the power spectrum but introduce an uncertainty of $\sim 20\%$ in the amplitude of $P(k)$ even at the moderate depths of the APM Survey (*cf* the estimates of r_0 in equations 39 derived from Limber’s equation). The dotted lines in Figure 32a show the inversion of the $w(\theta)$ estimates for each of the four nearly equal area zones (*cf* Figure 27b). The points show the mean of these curves together with the standard deviation of the mean. The thick solid line shows the inversion of the $w(\theta)$ estimate for the full APM area (Figure 2). Figure 32b shows a check of the inversion procedure; here we have integrated equation (42a) by linearly interpolating the inverted power spectrum for the full APM area and compared the resulting $w(\theta)$ (plotted as the solid line) against the APM data points. The agreement is excellent, showing that the inversion is extremely accurate (see BE for further tests of this method).

Figure 32a shows that we recover the power spectrum accurately for wavenumber $k \gtrsim 0.05h \text{ Mpc}^{-1}$. At smaller wavenumbers there is considerable scatter between the estimates from different zones and at these wavenumbers, systematic errors of $\sim 10^{-3}$ in $w(\theta)$ can bias the estimates of $P(k)$ (*cf* Figure 7 of BE). Thus, although we see tentative evidence for a peak in the power spectrum at $k \sim 0.05h \text{ Mpc}^{-1}$, we caution readers that the scatter between zones is likely to underestimate the errors in $P(k)$, which are probably dominated by systematic errors at such small wavenumbers.

We have integrated equation (41) using the power spectra for each of the four zones plotted in Figure 32a to compute σ_8 . The result is

$$\sigma_8 = 0.96 \pm 0.04 \tag{43}$$

where the error is determined from the scatter from the four zones. Uncertainties in the cosmological model and the exponent α in equation (42c) introduce an additional uncertainty of about 10% in this estimate. This is in agreement with the value $\sigma_8 \sim 1$ determined by Davis and Peebles (1983) from an analysis of $\xi(r)$ from the CfA redshift survey, but note that the estimate (43) is based on the power spectrum in real space, rather than in redshift space

and so is unaffected by the distortion of the clustering pattern caused by galaxy peculiar motions.

Figure 33 shows the inverted estimates of $P(k)$ plotted against the family of CDM power spectra, in analogy with Figure 31. Each of the theoretical power spectra has been normalized to $\sigma_8 = 1$. The standard CDM power spectrum, $\Gamma = 0.5$, provides a very poor match to the shape of the APM power spectrum. A value $\Gamma \approx 0.2 - 0.3$ provides a much better fit to the data, in agreement with our discussion of $w(\theta)$.

In Figure 34 we compare the APM power spectrum to the power spectra of the mass distributions from N-body simulations of three CDM-like models: standard CDM (SCDM) *i.e.* $\Omega = 1$, $h = 0.5$; a low density spatially flat model (LCDM) with $\Omega = 0.2$ and $h = 1$; a mixed dark matter (MDM) model with $h = 0.5$ in which CDM contributes $\Omega_{CDM} = 0.6$, light neutrinos contribute $\Omega_\nu = 0.3$ and baryons contribute $\Omega_b = 1$. The MDM and SCDM simulations are as described by Dalton *et al.* (1994); for each of these models we ran an ensemble of 10 simulations each containing 10^6 particles within a cubical computational box of length $300 h^{-1} \text{Mpc}$ using the P³M N-body code described by Efstathiou *et al.* (1985). The LCDM curves in Figure 34 were derived from an ensemble of 10 simulations each containing 4×10^6 particles within a box of length $600 h^{-1} \text{Mpc}$. The models were evolved to approximately match the amplitude of microwave background anisotropies determined from the first year COBE maps (Smoot *et al.* 1992); thus σ_8 for the mass fluctuations is equal to unity for the LCDM and SCDM models, and is 0.67 for the MDM model (ignoring gravitational wave contributions to the anisotropies, *e.g.* Crittenden *et al.* 1994).

Each of the curves in Figure 34 shows the mean of the power spectra of the mass distributions, $P_m(k)$, estimated from the simulations. For the MDM model, we have arbitrarily multiplied $P_m(k)$ by a constant b^2 , with $b = 1.3$ to match the observations on large scales, *i.e.* we have introduced a linear biasing factor in relating mass fluctuations to fluctuations in the galaxy distribution. Figure 34 illustrates the following points:

- (i) The SCDM curve has a similar shape to the linear theory power spectrum plotted in Figure 33 over almost the entire range of wavenumbers plotted in the Figure ($k \lesssim 0.3h \text{ Mpc}^{-1}$). To reconcile the SCDM curve with the APM data would require substantial scale-dependent biasing, with galaxies strongly biased relative to the mass distribution at wavenumbers $k \lesssim 0.1h \text{ Mpc}^{-1}$ and strongly antibiased at larger wavenumbers. An argument against scale dependent biasing as a resolution of this problem has been given by Dalton *et al.* (1994) who show that the spatial two-point correlation function of rich APM clusters of galaxies also fails to match the predictions of the SCDM model.
- (ii) The LCDM model provides a good match to the observations at wavenumbers $k \lesssim 0.1h \text{ Mpc}^{-1}$ but lies above the data points at larger wavenumbers. Evidently antibiasing is required on spatial scales $\lesssim 5 h^{-1} \text{Mpc}$ if this model is to match the clustering of the galaxy distribution (*cf* Efstathiou *et al.* 1990).
- (iii) The MDM model provides a satisfactory fit to the observations over the entire range of wavenumbers plotted in the Figure.

In summary, the APM angular correlation functions and the three dimensional power spectrum derived by inverting $w(\theta)$ are incompatible with the power spectrum expected in the standard CDM model with $\Gamma = 0.5$. Non-linear evolution of the mass fluctuations cannot resolve this discrepancy, as shown by the numerical simulations plotted in Figure 34. The observations are in better agreement with a CDM power spectrum with Γ in the range 0.2-0.3.

5.3 Comparison with power spectra determined from redshift surveys

In this subsection we compare the APM power spectrum with the power spectra estimated from redshift surveys. A number of authors have estimated power spectra of redshift surveys: Vogeley *et al.* (1992) and Park *et al.* (1994) have analyzed the CfA-2 survey (see Baumgart and Fry 1991, for an analysis of the CfA-1 survey); Park, Gott & da Costa (1992) and da Costa *et al.* (1994) have analyzed the optically selected Southern Sky Redshift Survey; Fisher *et al.* (1993) have computed the power spectrum of a redshift survey of IRAS galaxies with 60μ fluxes $f_{60} > 1.2\text{Jy}$ (see Fisher *et al.* 1995 for details of the 1.2Jy survey); Feldman, Kaiser & Peacock (1994) have estimated $P(k)$ for the sparse sampled 1 in 6 QDOT survey described by Lawrence *et al.* (1995).

Figure 35 shows the APM power spectrum (as in Figure 34) together with estimates of $P(k)$ for IRAS and optically selected galaxies. The open symbols show $P(k)$ from a reanalysis of the 1.2Jy and QDOT IRAS surveys by Tadros & Efstathiou (1995a). The open triangles show $P(k)$ for the CfA-2 survey from Park *et al.* (1994); these are derived from a volume limited subset of the CfA-2 survey consisting of 1509 galaxies to a coordinate distance of $101\text{ h}^{-1}\text{Mpc}$. The three lines show estimates of $P(k)$ in *redshift space* derived from the three ensembles of N-body simulations described in the previous subsection. We make the following remarks concerning this figure:

- (i) The IRAS power spectrum lies below the real-space estimates of $P(k)$ derived from the APM survey by a factor of ~ 1.5 . Since redshift space distortions are likely to boost the amplitude of the power spectrum in redshift space compared to that measured in real space (Kaiser 1987, compare also the redshift space and real space estimates of $P(k)$ for the simulations in Figures 34 and 35), we conclude that IRAS galaxies are more weakly clustered than optically selected galaxies on large scales. The effect is relatively small, and is consistent with an analysis of the cell-count variances of IRAS and the Stromlo-APM redshift surveys described by Efstathiou (1995c).
- (ii) The CfA-2 power spectrum has a slightly higher amplitude than the APM estimate in the wavenumber range $0.1 \lesssim k \lesssim 0.3h\text{ Mpc}^{-1}$. At $k \lesssim 0.10h\text{ Mpc}^{-1}$, the CfA-2 estimates have a slightly lower amplitude, but the errors on $P(k)$ at such low wavenumbers are large. In principle, a direct comparison of the APM estimates of $P(k)$ with an estimate derived from an optically selected redshift survey would allow a determination of the effects of redshift-space distortion. However, it is clear from Figure 35 that the observational errors (particularly in the redshift-space estimates of $P(k)$) are sufficiently large that it is not yet possible to set tight limits on the effects of redshift-space

distortions in the linear regime $k \lesssim 0.2h\text{Mpc}^{-1}$. This point is discussed in much greater detail in another paper (Tadros & Efstathiou 1995b), where we compare the APM $P(k)$ with redshift space estimates of $P(k)$ derived from the Stromlo-APM redshift survey (Loveday *et al.* 1992a,b). Analyses of redshift space distortions in redshift surveys are described by Hamilton (1993b) Fisher *et al.* (1994), Cole *et al.* (1994b), Peacock & Dodds (1994) and Loveday *et al.* (1995).

- (iii) The redshift-space power spectra derived for the MDM and LCDM models are compatible with the CfA-2 estimates with the large observational errors. The SCDM curve lies slightly lower than the CfA-2 estimates and slightly higher than the IRAS estimates, though the general shape is compatible with the both estimates (*cf* Bahcall *et al.* 1994, who make a similar point). This illustrates a point that we have discussed in detail in other papers (*e.g.* Loveday *et al.* 1992b, Efstathiou 1995a,c), namely that the uncertainties on estimate of $P(k)$ derived from redshift surveys are sufficiently large that they cannot yet distinguish between different CDM-like models.

6. Conclusions

The main conclusions of this paper are as follows:

- (i) We have discussed various estimators of $w(\theta)$ and illustrated the biases in estimates caused by integral constraints and gradients in the galaxy surface density that are correlated with the survey boundaries. Estimates of $w(\theta)$ derived from single Schmidt plates are biased significantly by the integral constraint and this leads to an artificial break in $w(\theta)$ from a power law.
- (ii) We have investigated how errors in the selection of galaxies in the APM survey will affect our estimates of $w(\theta)$. We have analyzed simulations of errors including correlated plate matching errors and field effects, and show that the observed plate overlap residuals and the good agreement between the inter-plate and intra-plate estimates of $w(\theta)$ limit the error in $w(\theta)$ to be $\lesssim 10^{-3}$.
- (iii) We have used a large body of CCD photometry from the Las Campanas Deep Redshift Survey to estimate the errors in the APM magnitudes. The results are consistent with the error estimates of Paper II and show that the zero-point magnitude error for a typical APM field is in the range $0.04 \lesssim \sigma_{APM} \lesssim 0.05$ magnitudes. We estimate that photometric errors lead to systematic errors of $\lesssim 10^{-3}$ in $w(\theta)$.
- (iv) We have investigated the criticisms of the APM photometry by Fong *et al.* (1992) and have shown that they are unjustified. In particular, large photometric errors as claimed by Fong *et al.* are incompatible with the good agreement that we have found between the APM and LCDRS photometry, with the uniformity of the galaxy counts in the APM survey, and with various other tests of the accuracy of the APM magnitudes described in Paper II.

- (v) There is no evidence for any correlation between errors in the APM Survey and the exposure or scanning dates of the Schmidt plates.
- (vi) The effects of Galactic obscuration have been investigated using IRAS maps of $100\mu\text{m}$ emission. We estimate that the angular correlation functions measured from the APM Survey are biased by at most 8×10^{-4} by variable Galactic obscuration.
- (vii) The changes in stellar contamination of the APM galaxy sample caused by the variation in stellar surface density in our galaxy are negligible over the area we use to estimate the galaxy correlations.
- (viii) We have used the magnitude residuals on plate overlaps and inter- and intra-plate residuals in $w(\theta)$ to estimate the errors in the APM survey as a function of magnitude. The systematic errors in $w(\theta)$ are found to be independent of magnitude except close to the magnitude limit of the survey $b_J > 20$, where plate-to-plate variability in star-galaxy classifications introduces fluctuations in the APM counts.
- (ix) We have presented estimates of $w(\theta)$ as a function of limiting magnitude corrected for various sources of systematic error. The corrections are almost negligible except for the faintest magnitude slice $20 \leq b_J \leq 20.5$.
- (x) We have used faint redshift surveys to determine the selection function of the APM survey as a function of limiting magnitude. By evaluating Limber's equation, we show that the APM estimates of $w(\theta)$ scale accurately with depth, as expected if we are measuring real structure in the galaxy distribution.
- (xi) The APM $w(\theta)$ estimates show slightly less power at large angular scales than the estimates from the Edinburgh-Durham Southern Galaxy Catalogue (EDSGC). The discrepancy may be explained by the larger photometric errors and smaller area of the EDSGC.
- (xii) The APM $w(\theta)$ estimates are higher at large angular scales than the GP77 estimates of $w(\theta)$ from the filtered Lick counts. We have argued that GP77 may have removed real clustering by filtering the Lick catalogue.
- (xiii) The APM $w(\theta)$ estimates are incompatible with the linear theory predictions of the standard CDM model with $\Gamma = \Omega_0 h = 0.5$. Our angular correlation functions are much better described by a CDM model with Γ in the range 0.2–0.3.
- (xiv) We reach similar conclusions by comparing the three-dimensional power-spectrum $P(k)$ determined by inverting our estimates of $w(\theta)$. By calculating $P(k)$ from N-body simulations we show that non-linear evolution cannot reconcile the standard cold dark matter model with the shape of $P(k)$ determined from the APM survey.

Acknowledgements

We wish to thank the staff of the UK Schmidt Telescope for providing the excellent plate material on which this survey is based; We are indebted to the APM group at Cambridge (Mike Irwin, Pete Bunclark & Mick Bridgeland) for much advice and assistance over the past seven years and to Gavin Dalton and Jon Loveday for their contributions to the APM Galaxy Survey. We thank Douglas Tucker and Richard Ellis, and their collaborators, for supplying data in advance of publication. GPE and WJS would like to thank PPARC for the award of Senior and Advanced Fellowships respectively.

REFERENCES

- Bahcall N.A., Cen R., Gramann M., 1994, ApJ, **408**, L77.
- Baugh C.M., Efstathiou G., 1993, MNRAS, **265**, 145.
- Baugh C.M., Efstathiou G., 1994, MNRAS, **267**, 323.
- Baumgart D.J., Fry J.N., 1991, ApJ, **375**, 25.
- Blumenthal G.R., Faber S.M., Primack J.R., Rees M.J., 1994, Nature, **311**, 517.
- Bond J.R., Efstathiou G., 1984, ApJ, **285**, L45.
- Broadhurst T.J., Ellis R.S., Shanks T., 1988, MNRAS, **235** 827.
- Cole S., Ellis R.S., Broadhurst T., Colless M., 1994a, MNRAS, **267**, 541.
- Cole S., Fisher K.B., Weinberg D.H., 1994b, MNRAS, **267**, 785.
- Colless M.M., Ellis R.S., Taylor K., Hook R.N., 1990, MNRAS, **244**, 408.
- Colless M.M., Ellis R.S., Broadhurst T.J., Taylor K., Peterson B.A., 1993, MNRAS, **261**, 19.
- Collins C.A., Heydon-Dumbleton N.H., MacGillivray, H.T., 1989, MNRAS, **236**, 7p.
- Collins C.A., Nichol R.C., Lumsden S.L., 1992, MNRAS, **254**, 295.
- Cowie L.L., Lilly S.J., Gardner J.P., McLean I.S., 1988, ApJ, L29.
- Crittenden R., Bond J.R., Davis R.L., Steinhardt P.L., 1993, PRL, **71**, 324.
- da Costa L.N., Vogeley, M.S., Geller M.J., Huchra J.P., Park C., 1994, ApJ, **437**, L1.
- Dalton G.B., Efstathiou G., Maddox S.J., Sutherland W.J., 1992, ApJ, **390**, L1.
- Dalton G.B., Efstathiou G., Maddox S.J., Sutherland W.J., 1994a, MNRAS, **269**, 151.
(Paper IV)
- Dalton G.B., Croft R.A.C., Efstathiou G., Sutherland W.J., Maddox S.J., Davis, M., 1994b, MNRAS, **271**, L47.
- Dalton G.B., Efstathiou G., Sutherland W.J., Maddox S.J., 1995, in preparation. (Paper V).
- Davis M., Peebles P.J.E., 1983, ApJ, **267**, 465.
- Davis M., Efstathiou G., Frenk C.S., White, S.D.M., 1985, ApJ, **292**, 371.

de Lapparent V., Kurtz M.J., Geller, M.J., 1986, ApJ, **304**, 585.

Efstathiou G., 1993, *Proc Natl Acad Sci. USA*, **90**, 4859.

Efstathiou G., 1995a, *Les Houches Lectures*, ed. R. Schaefer, Elsevier Science Publishers, Netherlands, in press.

Efstathiou G., 1995b, MNRAS, **272**, L25.

Efstathiou G., 1995c, MNRAS, **276**, 1425.

Efstathiou G., Davis M., Frenk C.S., White S.D.M., 1985, ApJ, **292**, 371.

Efstathiou, G., Ellis, R.S., Peterson, B.A., 1988, MNRAS, **232**, 431.

Efstathiou G., Sutherland W.J., Maddox S.J., 1990a, Nature, **348**, 705.

Efstathiou G., Bernstein G., Katz N., Tyson J.A., Guhathakurta, P., 1991, ApJ, **380**, L47.

Efstathiou G., Bond J.R., White S.D.M., 1992a, MNRAS, **258**, 1p.

Feldman H.A., Kaiser N., Peacock J.A., 1994, ApJ, **426**, 23.

Fisher K.B., Davis M., Strauss M.A., Yahil A., Huchra J.P., 1993, ApJ, **402**, 42.

Fisher K.B., Davis M., Strauss M.A., Yahil A., Huchra J.P., 1994, MNRAS, **267**, 927.

Fisher K.B., Strauss M.A., Davis M., Yahil A., Huchra J.P., 1995, ApJS, in press.

Fong R., Hale-Sutton D., Shanks T., 1992, MNRAS, **257**, 650. (F92)

Gaztanaga E., 1995, MNRAS, in press.

Gaztanaga E., Frieman J.A., 1994, ApJ, **437**, L13.

Geller M.J., de Lapparent V., Kurtz, M.J., 1984, ApJ, **287**, L55.

Groth E.J., Peebles P.J.E., 1977, ApJ, **217**, 38. (GP77)

Groth E.J., Peebles P.J.E., 1986a, ApJ, **310**, 499.

Groth, E.J., Peebles P.J.E., 1986b, ApJ, **310**, 507. (GP86)

Hamilton A.J.S., 1993a, ApJ, **417**, 19.

Hamilton A.J.S., 1993b, ApJ, **406**, L47.

Heydon-Dumbleton N.H., Collins C.A., MacGillivray H.T., 1989, MNRAS, **238**, 379.

Hewett P.C., 1982, MNRAS, **201**, 867.

Kaiser, N., 1987, MNRAS, **227**, 1.

Kolb E.W., Turner M.S., 1990, *The Early Universe*, Addison-Wesley Publishing Company.

Koo D.C., Szalay A.S., 1984, ApJ, **282**, 390.

Lambas D. Maddox S.J., Loveday J., 1992, MNRAS, **258**, 404.

Landy S.D., Szalay A.S., 1993, ApJ, **412**, 64.

Lawrence A. *et al.* , 1995, MNRAS, in press.

Limber, D.N., 1954, ApJ, **119**, 655.

Loveday J., Peterson, B.A, Efstathiou, G., Maddox S.J., 1992a, ApJ, **390**, 338.

Loveday J., Efstathiou, G., Peterson B.A., Maddox S.J., 1992b, ApJ, **400**, L43.

Loveday J., Maddox S.J., Efstathiou, G., Peterson B.A., 1995, ApJ, in press.

Lucy L.B., 1974, AJ, **79**, 745.

Maddox S.J., 1988, PhD Thesis, Cambridge.

Maddox S.J., Sutherland W.J., Efstathiou G., Loveday J., 1990a, MNRAS, **243**, 692. (Paper I).

Maddox S.J., Efstathiou G., Sutherland W.J., 1990b, MNRAS, **246**, 433. (Paper II).

Maddox S.J., Efstathiou G., Sutherland W.J., Loveday J., 1990c, MNRAS, **242**, 43p.

Maddox S.J., Sutherland W.J., Efstathiou G., Loveday J., Peterson B.A., 1990d, MNRAS, **247**, 1p.

Metcalfé N., Shanks T., Fong R., Roche N., 1995, MNRAS, **273**, 257.

Neuschaefer L.W., Windhorst R.A., Dressler A., 1991, ApJ, **382**, 32.

Neuschaefer L.W., Windhorst R.A., 1995, ApJ, **439**, 14.

Nichol R.C., Collins C.A., 1993, MNRAS, **265**, 867.

Park C., Gott J.R., da Costa, L.N., 1992, ApJ, **392**, L51.

Park C., Vogeley M.S., Geller M.J., Huchra J.P., 1994, ApJ, **431**, 569.

Peacock J.A., Dodds S.J., 1994, MNRAS, **267**, 1020.

Peebles, P.J.E., 1974, ApJ, **189**, L51.

Peebles P.J.E., 1980, *The Large-Scale Structure of the Universe*, Princeton University Press, Princeton.

Phillipps S., Fong R., Ellis R.S., Fall S.M., MacGillivray, H.T., 1978, MNRAS, **182**, 673.

Pritchett C., Infante L., 1986, AJ, **91**, 1.

Pritchett C., Infante L., 1992, ApJ, **399**, L35.

Roche N., Shanks T., Metcalfe N., Fong R., 1993, MNRAS, **263**, 360.

Rowan-Robinson M., Hughes J., Jones M., Leech, K., Veda, K., Walker D.W., 1991, MNRAS, **249**, 729.

Schechter P.L., 1976, ApJ, **203**, 297

Sebok, W.L., 1986, ApJS, **62**, 301.

Shane C.D., Wirtanen C.A., 1967, Publ Lick Observatory, **22**, part 1.

Shectman S., Schechter P.L., Oemler A., Tucker D., Kirshner R.P. Lin H., 1992, in *Clusters and Superclusters of Galaxies*, ed A.C. Fabian, Dordrecht, Kluwer, p351.

Shectman S., Landy S., Oemler A., Tucker D., Kirshner R., Lin H. & Schechter P., 1995, in *Wide Field Spectroscopy and the Distant Universe*, 35th Herstmonceux Conference, eds S.J. Maddox and A. Aragon-Salamanca, World Scientific Press, Singapore, p98.

Seldner M., Siebers B., Groth E.J., Peebles P.J.E., 1977, AJ, **82**, 249.

Shanks T., Fong R., Ellis R.S., MacGillivray H.T., 1980, MNRAS, **192**, 209.

Smoot G.F. *et al.* 1992, ApJ, **396**, L1.

Soneira R.M., Peebles P.J.E., 1978, AJ, **83**, 845.

Stevenson P.R.F., Shanks T., Fong R., MacGillivray, H.T., 1985, MNRAS, **213**, 953.

Szapudi I., Dalton G.B., Efstathiou G., Szalay, A.S., 1995, ApJ, **444**, 520.

Tadros H., Efstathiou G., 1995a, MNRAS, **276**, L45.

Tadros H., Efstathiou G., 1995b, submitted.

Tyson, J.A., 1988, AJ, **96**, 1.

Vogele M.S., Park C., Geller M.J., Huchra J.P., 1992 ApJ, **391**, L5.

Appendix A: Estimators of the Angular Correlation Function

A.1 Soneira-Peebles Simulations

There has been some disagreement between authors concerning biases in estimators of angular correlation functions (*e.g.* Shanks *et al* 1980, Hewett 1982). We have therefore checked a number of estimators using simulations of clustered galaxy distributions. We have also used these simulations to assess the effect on $w(\theta)$ of filtering the data.

The simulations that we have used follow the prescription of Soneira and Peebles (1978) which uses a simple algorithm designed to produce galaxy distributions with a similar visual appearance and low-order correlation function as the Lick survey. Although N-body simulations can provide a better match to the observed “frothy” nature of the galaxy distribution, extremely large simulations would be necessary to model the large volume ($\sim 10^8 \text{Mpc}^3$) sampled by the APM Survey and so would be time-consuming to generate.

The Soneira-Peebles simulations are constructed from a large number of ‘clumps’: for each clump, an imaginary rod of length L is randomly oriented in space. Two shorter rods of length L/a are randomly oriented, with their centres at the ends of the first rod; two rods of length L/a^2 are randomly oriented with their centres at the ends of each of the previous two, and the process is continued for a number of ‘levels’, N . A ‘galaxy’ is placed at the end of each rod on the N th level, i.e. 2^N galaxies in a clump of level N . If all clumps have the same N , the amplitudes of the three and four point correlation functions are smaller than observed, thus a dispersion is introduced in the number of levels (see Table A.1) to produce approximately the observed values.

The clumps are distributed randomly in space within a cone of half-angle 30° and length $1000 \text{h}^{-1} \text{Mpc}$, and then “observed” from a point on the axis of the cone, $50 \text{h}^{-1} \text{Mpc}$ inside the apex (to avoid boundary effects): galaxies are accepted or rejected with a probability calculated from a Schechter (1976) luminosity function, with an apparent magnitude limit of $b_J = 20$. This produces a simulated 0.85 steradian of ‘sky’ for which we construct an equal area maps as for the real survey data, and use this to measure the angular correlation function.

A few short-cuts, as described by Soneira and Peebles, were used to speed up the computations. The spatial volume was truncated at $1000 \text{h}^{-1} \text{Mpc}$ where the selection probability is $\sim 1\%$, each clump was reused a number of times at different positions in space (but different galaxies visible each time), and if the selection probability p at the distance of a given clump was ≤ 0.05 we simply chose pN galaxies randomly from the clump rather than generating a different random number for every galaxy. None of these simplifications will have any significant effect on the correlation function. The random numbers were generated by the NAG routine G05CAF in ‘batches’ of 1000, placed into an array and shuffled with another 1000 random numbers to ensure independence between successive random numbers.

One set of simulations (labelled SP0) has identical parameters to those given in Soneira and Peebles, shown in Table A.1. We generated simulations with additional large-scale power by scaling up the clumps: the minimum value of N was increased by 1, the length of the rods was scaled up by a factor 1.76 and the density of clumps was halved giving the set of simulations labelled SP1. Repeated scaling up gives the simulations labelled SP2, SP3 and SP4. This process does not change the small-scale correlation functions but simply moves the break in $w(\theta)$ to larger angles.

Table A.1 Parameters used in construction of clumps in the SP0 simulations

Definition	Parameter	Value
Min, max clump level	N_{min}, N_{max}	7, 12
% of clumps of level N	$p_7 \dots p_{12}$	68, 23, 6, 1.5, 0.5, 0.11
Length of longest rods	L_0	11.5 h ⁻¹ Mpc
Mean spacing of clumps	$n^{-1/3}$	20 h ⁻¹ Mpc

We also generated a simulation with power on very long wavelengths (*cf* the isocurvature baryon model, Peebles 1986) by simply imposing a large-scale gradient of amplitude $\pm 15\%$ across the observed ‘sky’ from an SP0 simulation. These simulations are labelled SPS. Grey-scale pictures of some typical simulations are shown in Figure A.1.

A.2 Estimating the Correlation Function

For each of the simulations we evaluated the correlation function $w(\theta)$ using the ‘direct’ estimator

$$w(\theta) = \frac{\langle N_i N_j \rangle}{\bar{N}^2} - 1, \quad (A1)$$

and the ‘ensemble’ estimator

$$w(\theta) = \frac{\langle N_i N_j \rangle}{\langle N_i \rangle \langle N_j \rangle} - 1. \quad (A2)$$

In these equations N_i is the galaxy count in cell i , \bar{N} is the mean galaxy count and the averages are over all cells with separations within the separation bin centred on angle θ . We also used an estimator based on the Fourier transform of the two-dimensional power spectrum. To evaluate the FT estimator, we constructed a 2-D array of galaxy counts in cells from an equal area projection of the catalogue. The mean from all data cells was subtracted from the data cells; cells outside the survey area were set to zero. We then evaluated the Fast Fourier Transform of this array, multiplied this by its complex conjugate and performed the inverse transform. We then defined the ‘window function’ by setting cells within the observational window equal to unity and setting those outside equal to zero: the same algorithm was then applied to this array. If $\delta(\mathbf{x})$ denotes the density field with the

mean subtracted (we ignore errors in the mean density, which will be discussed in Section A3), and $W(\mathbf{x})$ is the window function of the sample, then the observed density field is

$$\delta_{obs}(\mathbf{x}) = W(\mathbf{x})\delta(\mathbf{x}).$$

Fourier transforming

$$\hat{\delta}_{obs}(\mathbf{k}) = (\hat{W} * \hat{\delta})_{\mathbf{k}}$$

and so the power-spectrum in two dimensions is

$$P_{obs}(\mathbf{k}) = (\hat{W} * \hat{\delta})_{\mathbf{k}}(\hat{W} * \hat{\delta})_{-\mathbf{k}}.$$

The inverse FT of the power spectrum, $f(\mathbf{x})$, is is

$$\begin{aligned} f(\mathbf{x}) &= \mathcal{F}^{-1}(P(\mathbf{k})) \\ &= \mathcal{F}^{-1}((\hat{W} * \hat{\delta})_{\mathbf{k}}) * \mathcal{F}^{-1}(\hat{W} * \hat{\delta})_{-\mathbf{k}} \\ &= (W\delta * \overline{W}\overline{\delta})(\mathbf{x}) \end{aligned}$$

where $\overline{W}(\mathbf{x}) \equiv W(-\mathbf{x})$ and \mathcal{F}^{-1} denotes the inverse Fourier transform. If the window is uncorrelated with the true galaxy distribution,

$$\begin{aligned} f(\mathbf{x}) &= W * \overline{W}(\mathbf{x}) \delta * \overline{\delta}(\mathbf{x}) \\ &= \langle W(\mathbf{a})W(\mathbf{a} + \mathbf{x}) \rangle \langle \delta(\mathbf{a})\delta(\mathbf{a} + \mathbf{x}) \rangle \end{aligned} \tag{A3}$$

and so $f(x)$ is equal to the product of the correlation functions of the window function and the galaxy density. The FT estimate of the correlation function w_{FT} is therefore given by dividing the inverse FT of the power spectrum of the data by that of the window function, then radially averaging in bins of $|\mathbf{x}|$ to give $w(\theta)$.

We first evaluated the correlation functions with the ensemble and direct estimators for a number of simulated Schmidt plates of 5° square using the SP0 simulation parameters. This is of interest because several authors have published estimates of $w(\theta)$ from individual Schmidt plates (see Section 4.2.1) and there has been some controversy concerning the reliability of the results, for example whether the results are biased low because of the small area used to define the mean surface density. Some typical results from our simulations are shown in Figure A.2: there is substantial scatter between plates using the ensemble estimator, but very much large scatter using the direct estimator. In both cases the mean $w(\theta)$ of the 9 plates shown is biased significantly low relative to $w(\theta)$ for the whole area. The large scatter for the direct estimator can be explained by edge effects as follows: in a finite sample, cells have different numbers of neighbours separated by angle θ depending on their proximity to the boundary, hence cells have different weights. For $\theta \lesssim 0.5 \times$ the sample size, cells at the edge have half the weight of those at the centre. For $\theta \gtrsim 0.5 \times$ the sample size, central cells have zero weight whereas edge cells have high weights. If there are substantial density variations on scales comparable to the sample size, then the mean density for central

cells may differ from that of cells at the edges. Thus using a global estimate of the mean cell count \bar{N} is then inappropriate and introduces an error that is first order in $\delta\rho/\rho$ whereas $w(\theta)$ is second order. Thus the direct estimator becomes unreliable if structures exist on scales comparable to the sample area. This is discussed in further detail in Section A.3.

After averaging over the simulations, the estimates for both estimates are biased low. For the direct estimator, with a total of N_T galaxies in n_c cells it is clear that an integral constraint applies, as described in Section 2.2, since

$$\bar{N}^2 \sum_{i,j} w(\theta_{ij}) = \sum_{i,j} (N_i N_j - \bar{N}^2) = N_T^2 - n_c^2 \left(\frac{N_T}{n_c} \right)^2 = 0.$$

The bias is second order in $\delta\rho/\rho$. The ensemble estimator is also subject to an integral constraint which leads to a bias that is second order in $\delta\rho/\rho$, but in this case, the expression for the bias is more complex (see Section A3).

We also evaluated each estimator of $w(\theta)$ for the full 60° cone for each of the simulations. Results for simulations SP0, SP2 and SP4 are shown in Figure A.3. In each case the ensemble and FT estimators are in excellent agreement with each other and with the expected behaviour built in to the simulation. For the SP0 model the break occurs at $\sim 1.5^\circ$, half the scale of the Lick survey, since the sample depth is about twice that of Lick. For SP2 and SP4 the break moves outward as expected, occurring very close to the noise for SP4.

The direct estimator agrees well for the SP0 simulation but is increasingly discrepant for SP2 and SP4: this is because the added large-scale power results in fewer independent structures in each simulation and so the edge effects become more important. This is illustrated in Figure A.4 which shows results for three different realizations of the SP4 prescription; the direct estimator shows very large scatter between different realizations.

For the SPS simulation with an added large-scale gradient, both the ensemble and direct estimators show a positive tail $w(\theta) \sim 5 \times 10^{-3}$ as expected. This is plotted in Figure A5, and shows that any ‘filtering’ of large-scale power arising from the ensemble estimator is negligible (see Section A3).

We have also investigated the effect on $w(\theta)$ of fitting large-scale smoothing functions to the galaxy counts (as in GP77): we fitted a two-dimensional cubic polynomial (i.e. a bicubic spline with no knots) to the data map, divided the map by the polynomial and multiplied by the previous mean density, then evaluated $w(\theta)$ using the ensemble estimator. Some typical results for an SP4 simulation are shown in Figure A.6: the result is very close to simply subtracting the correlation function of the spline from that of the data. This moves the break to smaller angles and substantially steepens the slope beyond the break, so the $w(\theta)$ for a spline-filtered SP4 simulation is quite similar to that for an SP0 simulation. Slight anticorrelation is seen beyond the break as in GP77. This suggests that the GP77 smoothing functions may have removed some true signal from their correlation function results.

The conclusions of this section can be summarized as follows:

- (i) The direct estimator displays large fluctuations which are of first order in the fluctuations in the galaxy distribution and so dominate the estimates of $w(\theta)$ at large angles. The fluctuations in ensemble estimator are of second order in $\delta\rho/\rho$.
- (ii) Both the ensemble and direct estimators are biased low by integral constraints on scales comparable to the sample size.
- (iii) The ensemble and FT estimators agree very well.
- (iv) The ensemble estimator is very nearly unbiased and does not filter out large scale power in the galaxy distribution as has sometimes been claimed.
- (iii) Fitting large-scale smoothing functions to the observed galaxy distribution (cf GP77) can remove power on *intermediate* scales, and move the break in $w(\theta)$ to smaller angles.

A.3 Mathematical Analysis of Estimators

Hamilton (1993a) has recently made a comprehensive mathematical analysis of estimators of correlation functions and it is useful to summarize how his results relate to those of the previous section. Denoting the window function of the survey as W , the observed galaxy density is

$$N = \overline{N}W(1 + \delta), \quad (A4)$$

where \overline{N} is the mean surface density. The mean overdensity of the catalogue $\overline{\delta}$, the galaxy-catalogue correlation function $\psi(\theta)$, and the windowed galaxy-galaxy correlation function w_c are defined by

$$\overline{\delta} = \frac{\langle W\delta \rangle}{\langle W \rangle}, \quad \psi = \frac{\langle W_1\delta_1W_2 \rangle}{\langle W_1W_2 \rangle}, \quad w_c = \frac{\langle W_1\delta_1\delta_2W_2 \rangle}{\langle W_1W_2 \rangle}. \quad (A5)$$

The direct estimator is related to these quantities by

$$w_D(\theta) = \frac{w_c(\theta) + 2\psi(\theta) - 2\overline{\delta} - \overline{\delta}^2}{(1 + \overline{\delta})^2}, \quad (A6)$$

and the ensemble estimator gives

$$w_E(\theta) = \frac{w_c(\theta) - \psi^2(\theta)}{(1 + \psi(\theta))^2}, \quad (A7)$$

(Hamilton 1993a). In our application, the window function is either zero or unity, hence $\psi(0) = \overline{\delta}$, and so the two first order terms in equation A6 do not quite cancel leading to a first-order error in $\delta\rho/\rho$ that depends on the distribution of galaxies relative to the boundaries of the sample. This is why the direct estimator leads to such a large scatter when applied to the simulations of the previous section.

It is easy to apply this analysis to the Fourier transform estimator of $w(\theta)$ defined in the previous section. This gives

$$w_{FT}(\theta) = w_c(\theta) - 2\psi(\theta)\bar{\delta} - \bar{\delta}^2, \quad (\text{A8})$$

and so differs from the true catalogue correlation function by second order terms. This is why the FT and ensemble estimators agree so closely.

If we average over a large number of catalogues, the first order terms in equation (A6) average to zero, but the expectation value of the second order term is the expected variance of the overdensity within the field area

$$\langle \bar{\delta}^2 \rangle = \frac{\int W_1 W_2 w(\theta_{12}) d\Omega_1 d\Omega_2}{[\int W_1 d\Omega_1]^2} = \frac{1}{\Omega^2} \int w(\theta_{12}) d\Omega_1 d\Omega_2 \quad (\text{A9})$$

i.e. the mean of the direct estimate estimate differs from the true catalogue correlation function by the integral constraint (equation 10) as discussed in Section 2.2.

Each of the estimators (A5) - (A7) is subject to an integral-type constraint leading to a bias that is second order in $\delta\rho/\rho$, for example, the ensemble estimator is biased low by

$$\langle \psi^2(r) \rangle = \frac{\int W_1 W_2 W_3 W_4 w(\theta_{13}) d\Omega_1 d\Omega_2 d\Omega_3 d\Omega_4}{[\int W_1 W_2 d\Omega_1 d\Omega]^2}, \quad (\text{A10})$$

where W_1 and W_2 , and W_3 and W_4 are separated by r . If the separation r is small compared to the size of the sample, we can make the approximation $W_1 \approx W_2$, $W_3 \approx W_4$ and so $\langle \psi^2(r) \rangle \approx \bar{\delta}^2$, *i.e.* the offset is the same as for the direct estimator. This result is true for all of the estimators considered here, including the estimator of equation (5) used for single plate estimates in section 2.2. In summary, first order errors in the estimates of $w(\theta)$ will average out over a large number of realizations leaving second order biases. At separations small compared to the survey size, the bias is approximately equal to the variance of the galaxy overdensity within the field, but at large separations the precise form of the correction depends on the particular estimator used to measure $w(\theta)$.

$17 < b_J < 20$

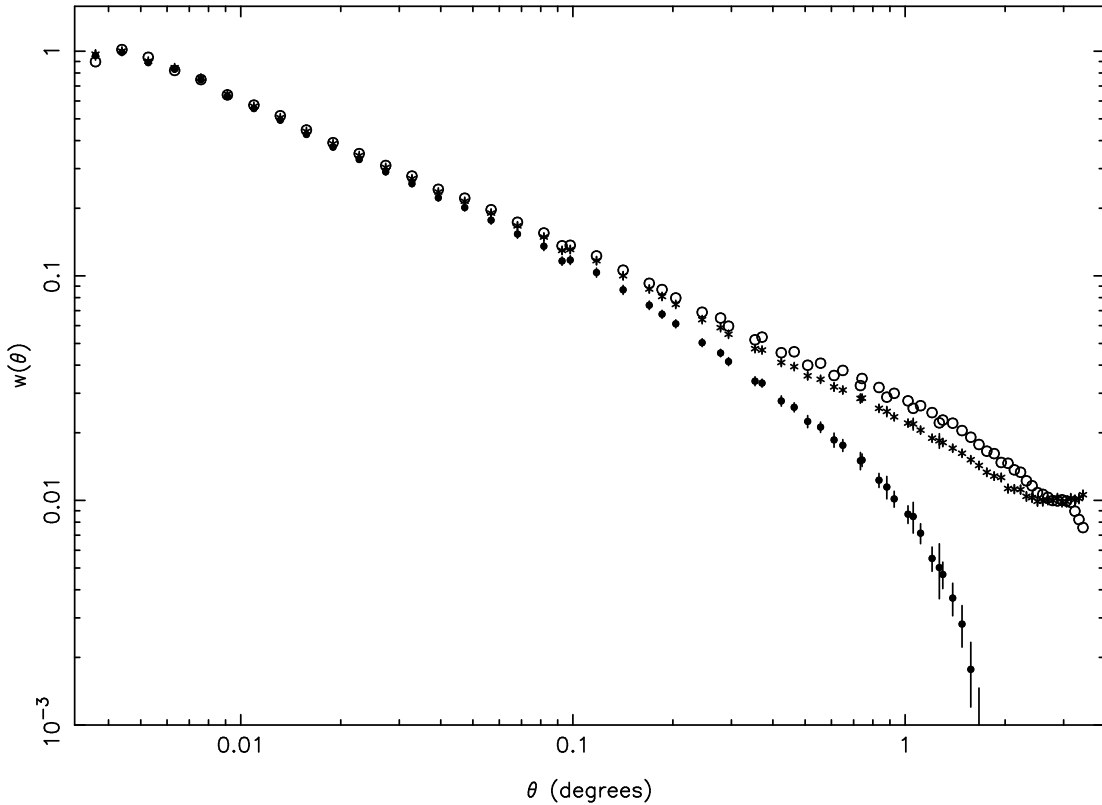


Figure 1. The filled circles show the mean of $w(\theta)$ for galaxies in the magnitude range $17 < b_J < 20$ determined by applying the direct pair count estimator (equation 6) to 185 Schmidt fields using the galaxy counts on each individual plate to normalize w . The open circles show the mean value of $w(\theta)$ using a global estimate of the mean surface density to normalize w . The stars show how $w(\theta)$ changes if a constant, $\bar{\delta}^2 = 1.4 \times 10^{-2}$ is added to the filled circles to correct for the bias introduced by the integral constraint (equation 10).

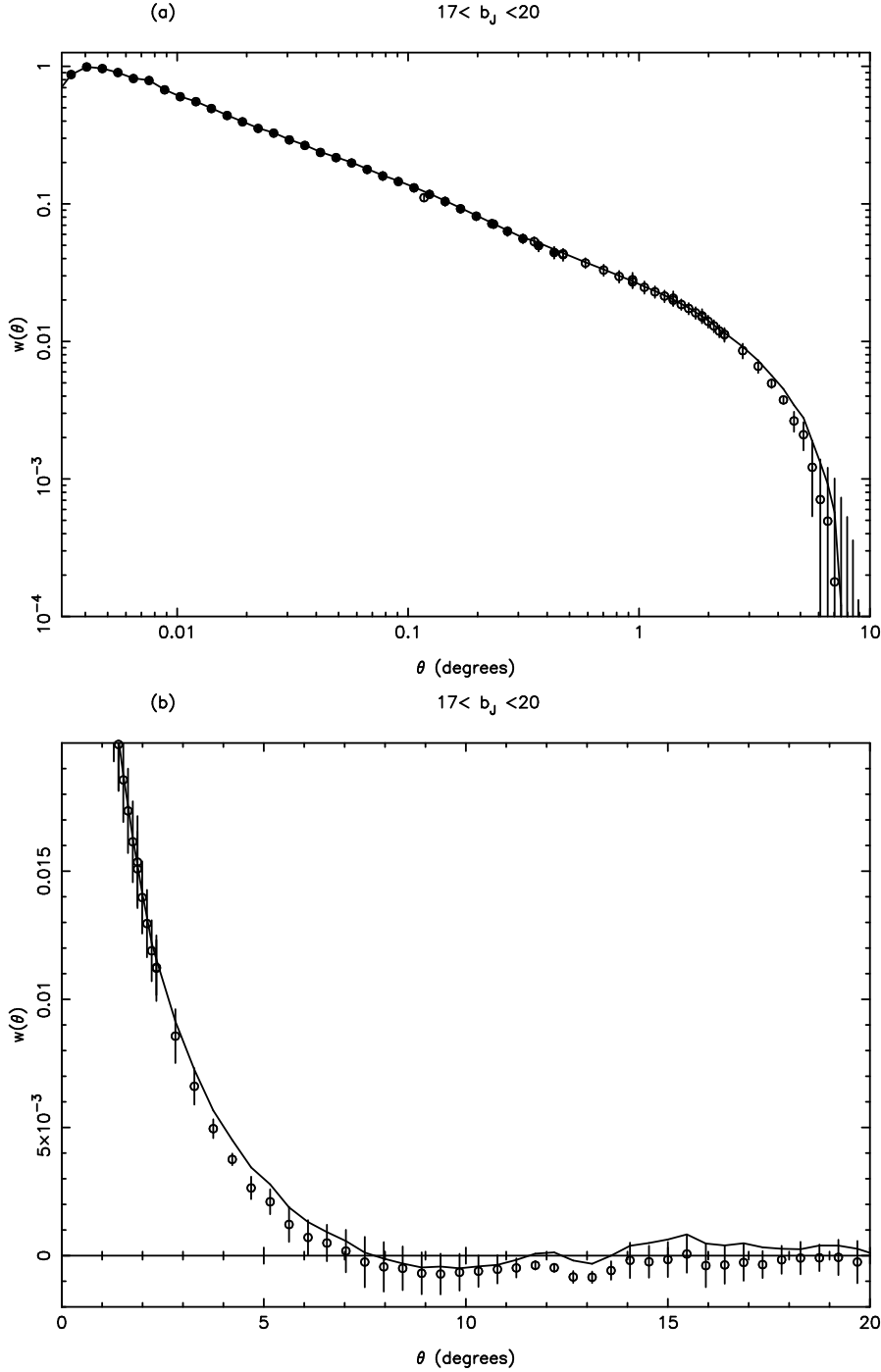


Figure 2. Estimates of $w(\theta)$ for galaxies with magnitudes in the range $17 < b_J < 20$ plotted with logarithmic axes in Figure (2a) and linear axes in Figure (2b). The line shows the estimate for the full area of the survey. The open circles at $\theta > 0.1^\circ$ show the mean of $w(\theta)$ derived by applying the ensemble estimator (equation 5) to four separate zones of approximately equal area. The error bars show one standard deviation on the mean determined from the zone-to-zone scatter. The filled circles at $\theta < 0.5^\circ$ show the mean of $w(\theta)$ and 1σ errors using the direct pair count estimator applied to 185 Schmidt plates (plotted as the stars in Figure 1).

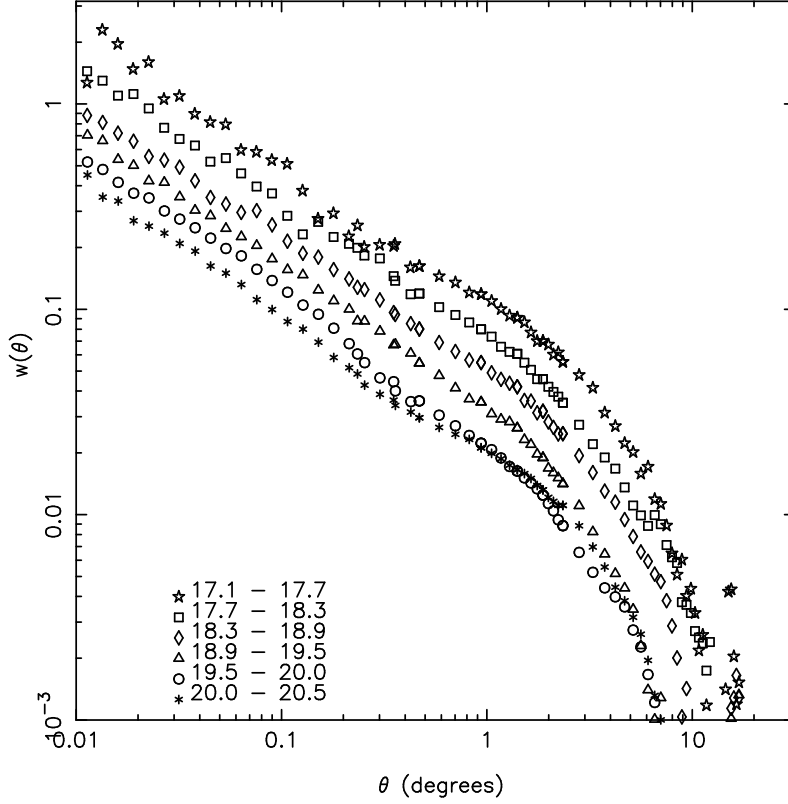


Figure 3. Estimates of $w(\theta)$ for six disjoint magnitude slices in the range $17.0 < b_J < 20.5$ derived from the central 120 plates of the survey at Galactic latitudes $b < -50^\circ$. For each magnitude slice the angular correlation functions at $\theta > 0.4^\circ$ are derived by applying the ensemble estimator (equation 5) to the central part of the equal area maps. At $\theta < 0.4^\circ$ $w(\theta)$ is derived by applying the direct pair count estimator to the 120 plates using a global estimate of the mean surface density to normalize w .

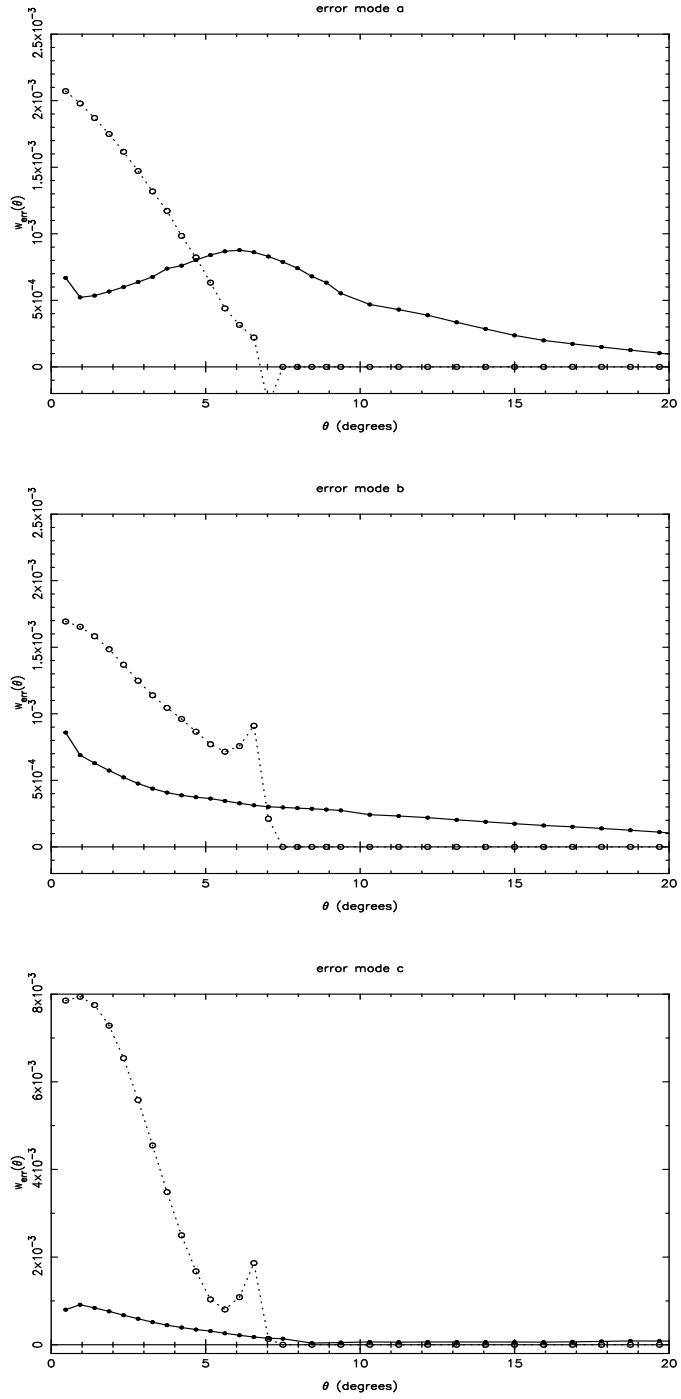


Figure 4. Angular correlation functions w_{err} estimated from simulated maps which include correlated overlap errors according to the modes (A)-(C) described in the text. The filled circles show the inter-plate estimates of w and open circles show the intra-plate estimates.

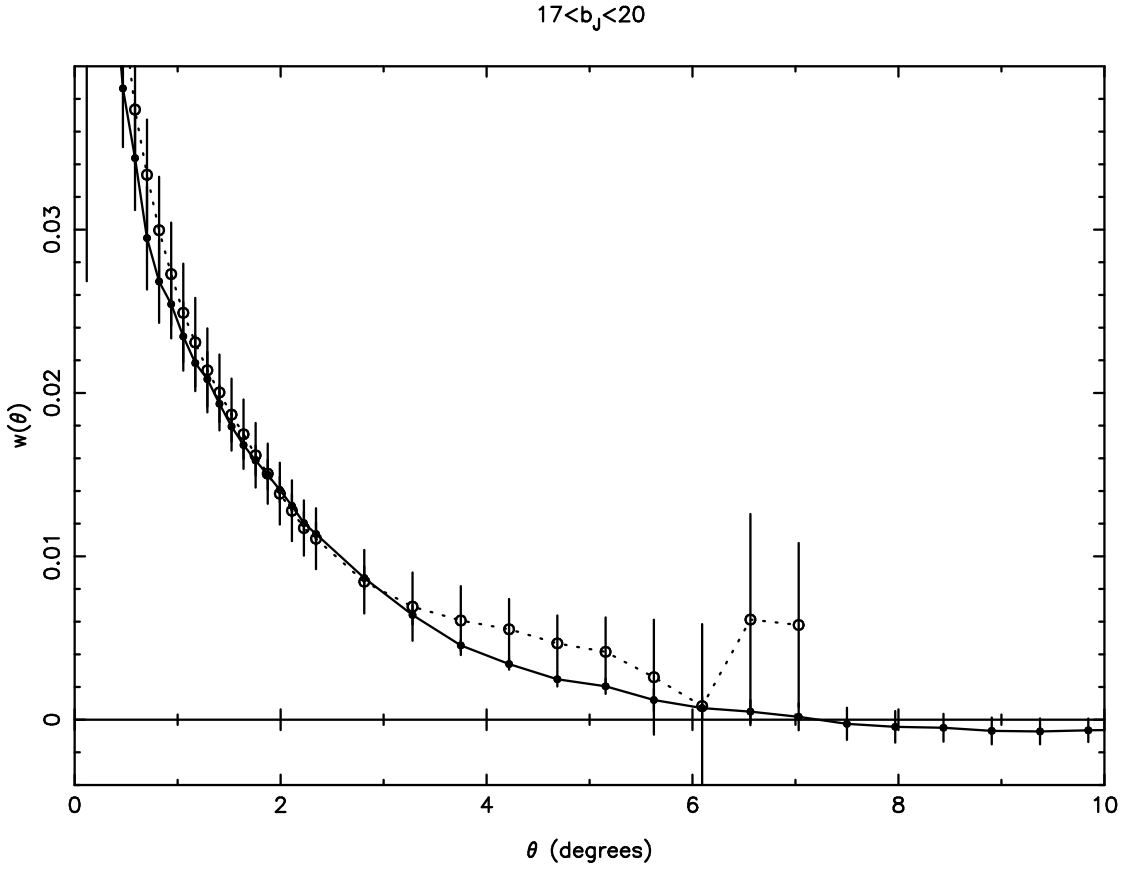


Figure 5. Inter- and intra-plate estimates of $w(\theta)$ for galaxies in the APM survey in the magnitude range $17 < b_J < 20$. The filled circles show the inter-plate estimates and open circles show the intra-plate estimates. The error bars are derived from the scatter of four nearly equal area zones.

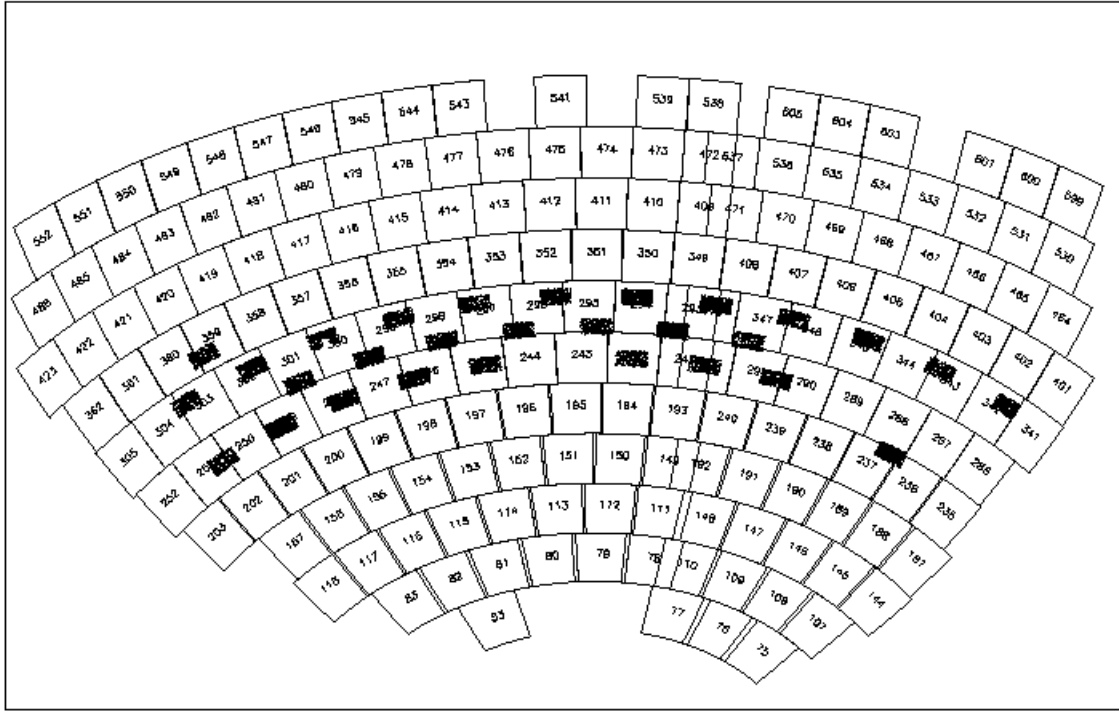


Figure 6. The position of the LCDRS fields relative to the UK Schmidt survey fields in the APM survey area. The map is in an equal area projection centred on the South Galactic Pole. A 5° square is plotted for each Schmidt field, and a dot is plotted for each LCDRS galaxy. Each LCDRS field has an area of $1.5^\circ \times 3.0^\circ$.

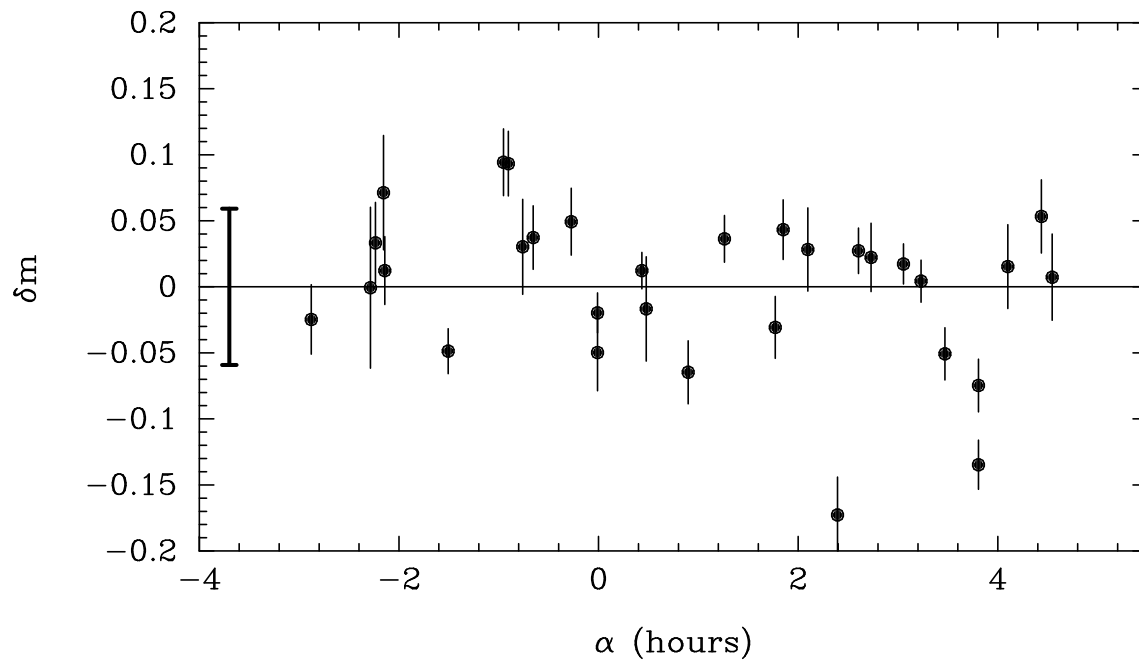


Figure 7. Magnitude residuals of the Las-Campanas-APM photometry plotted against right ascension. The thick error bar plotted to the left shows the *rms* scatter of the points about zero (0.051 magnitudes). The error bars on the points arise mainly from the scatter in galaxy colours.

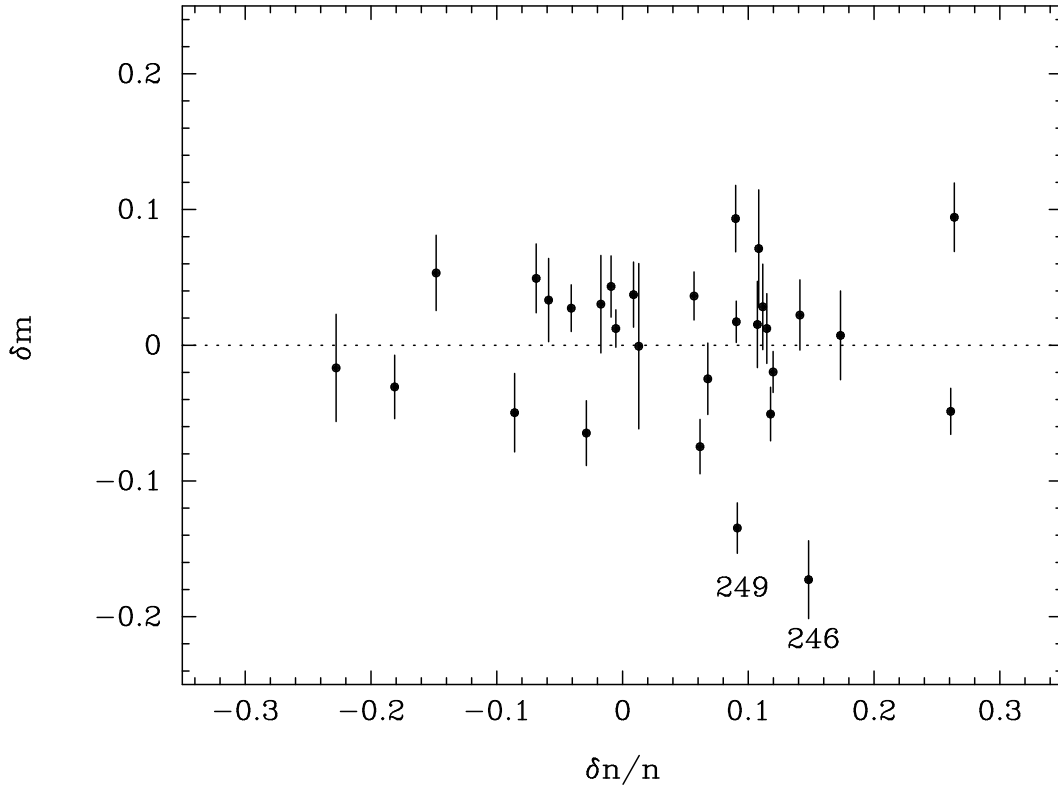


Figure 8. The Las Campanas-APM magnitude residuals plotted against fluctuations in the galaxy surface density in each APM field to a magnitude limit $b_J = 20$. The two outlying points in Figure 7, APM fields 246 and 249, are indicated.

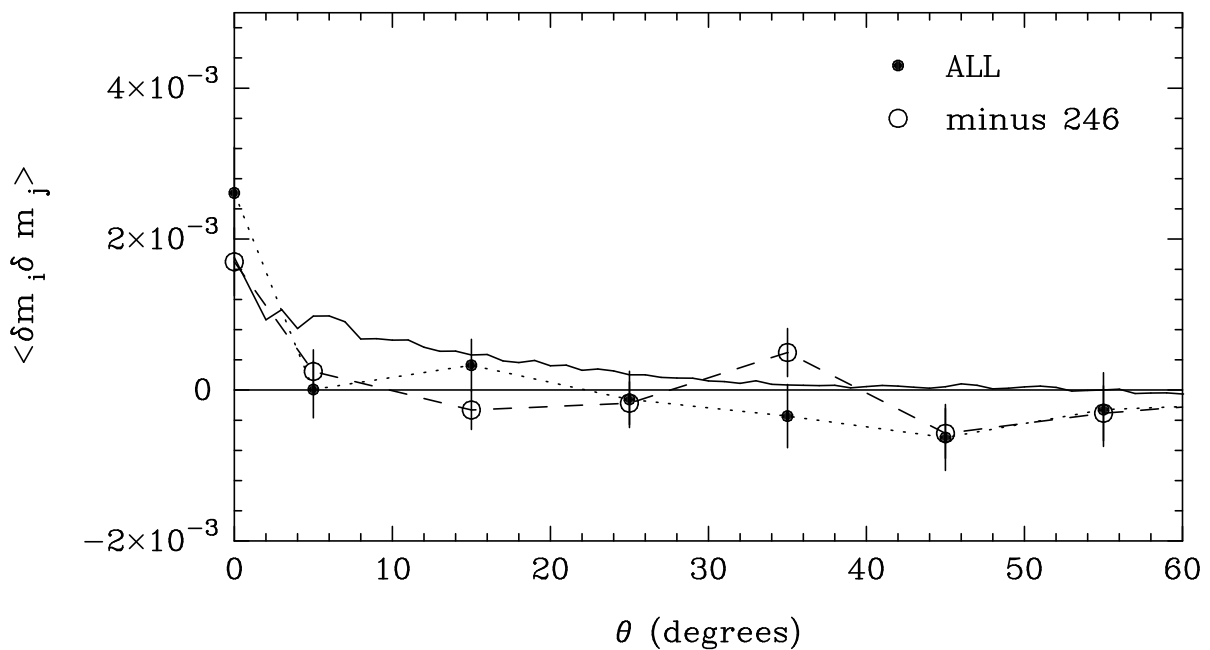


Figure 9. The correlation function of Las Campanas-APM magnitude residuals (equation 24) plotted as a function of angle. The filled points show the correlation function of all fields and the open circles show how the correlation function changes when the outlying field F246 is removed. The error bars are computed from equation (25). The solid line shows the Monte-Carlo model for mode [A] magnitude errors as described in Section 3.1.3.

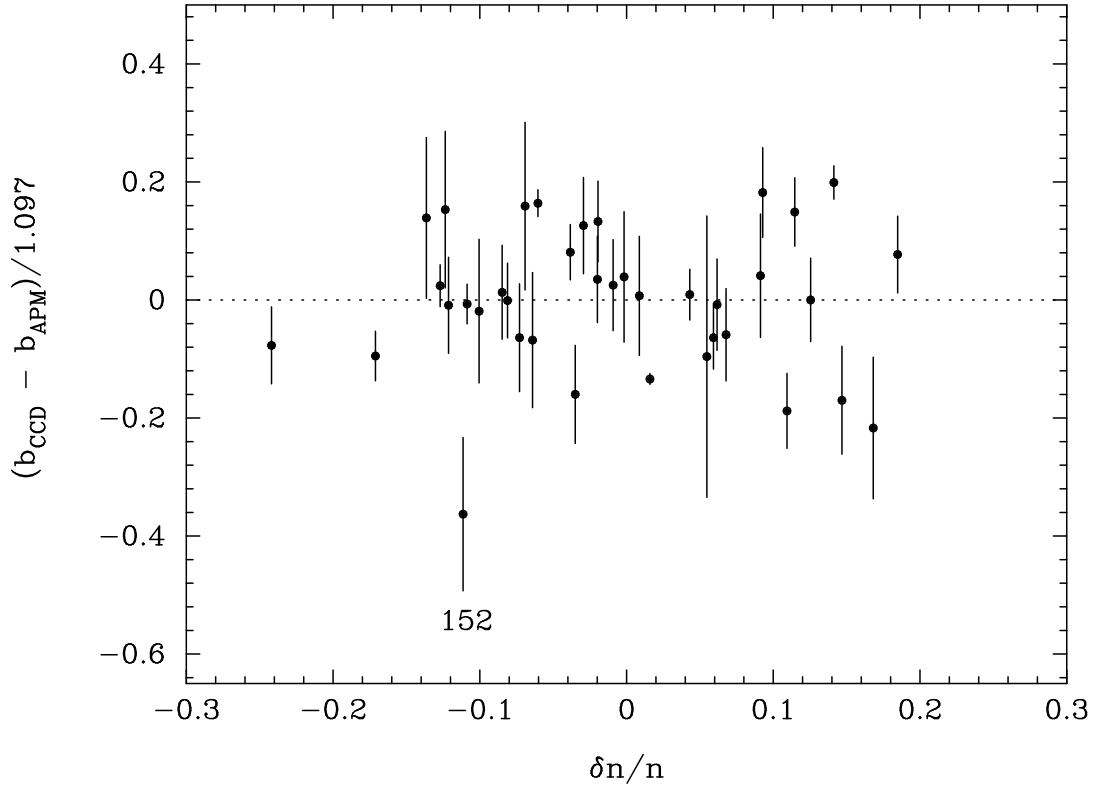


Figure 10. The Maddox et al CCD - APM magnitude residuals ($\bar{c}_i - \bar{c}$ in equation 27) plotted against fluctuations in the galaxy surface density in each APM field to a magnitude limit $b_J = 20$. The error bars show the *rms* fluctuation of the magnitude differences in each sequence listed in the final column of Table 3. The outlying APM field 152 is indicated.

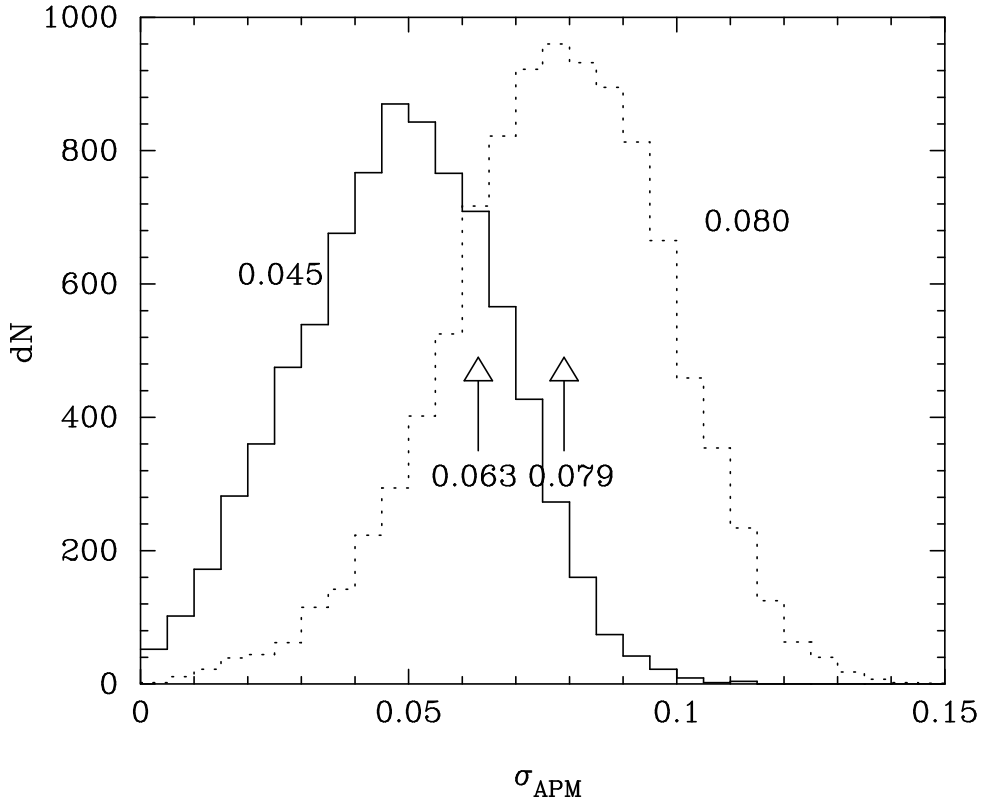


Figure 11. Histograms illustrating the accuracy with which σ_{APM} can be determined from the Maddox et al CCD sequences. The diagrams show the distribution of σ_{APM} from 10000 Monte-Carlo simulations of the Maddox et al CCD sequences as described in the text. The solid histogram shows the distribution if the true value of $\sigma_{APM} = 0.045$ and the dashed histogram shows the distribution if the true value is $\sigma_{APM} = 0.080$ as advocated by Fong *et al.* (1992). The arrows show the values determined from the real data, 0.079 if all fields are included and 0.063 if the outlying sequence on field 152 is excluded.

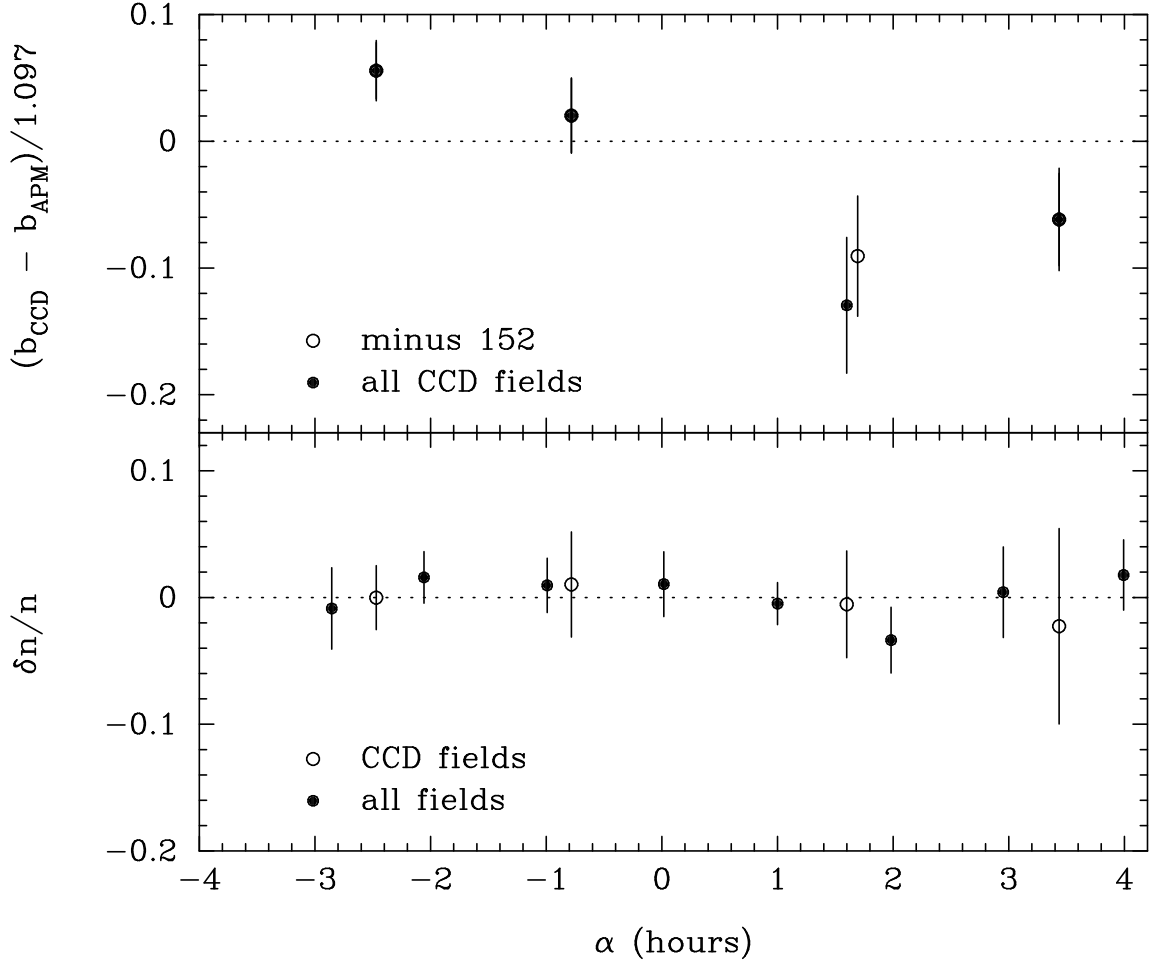


Figure 12. The upper panel shows Maddox et al CCD - APM magnitude residuals plotted against right ascension. The lower panel shows the fluctuations in the galaxy surface density to $b_J = 20$ in the APM fields plotted against right ascension. The filled circles in the lower panel show all fields in the APM survey and the open circles show only those fields in which there is a Maddox et al CCD sequence.

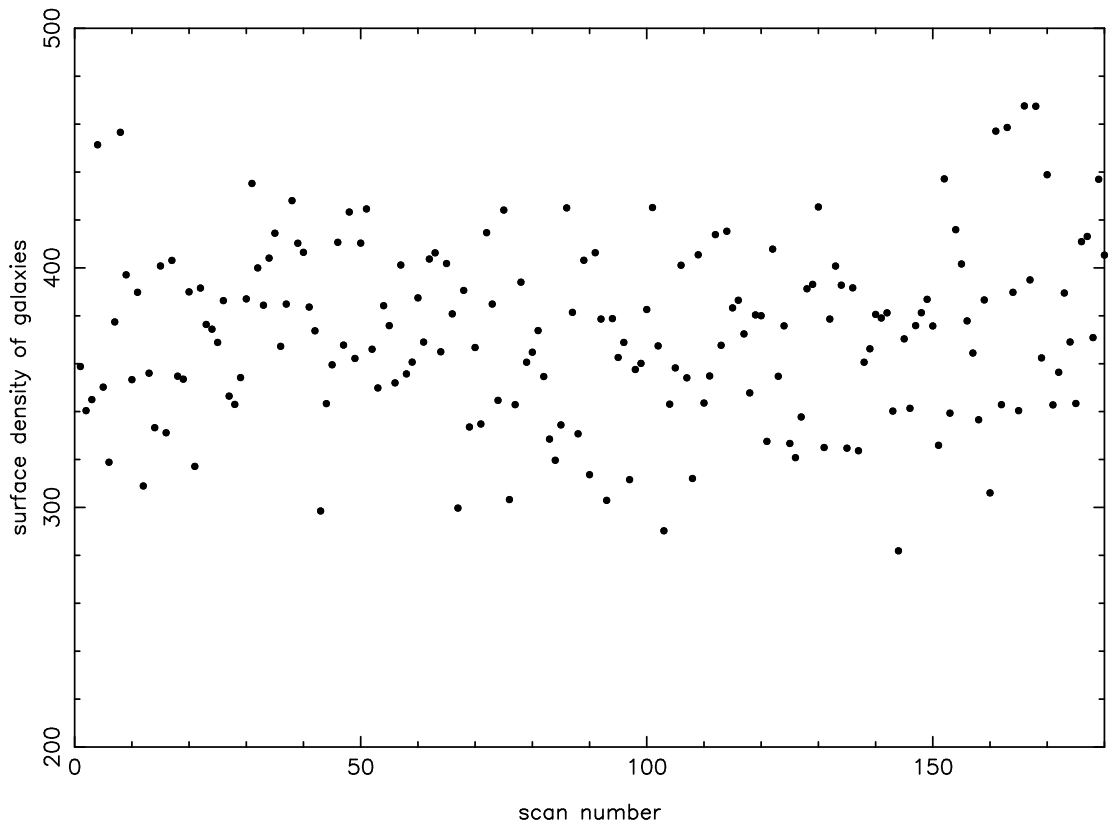


Figure 13. A scatter plot of the surface density of galaxies brighter than $b_J = 20.5$ on each plate in number per square degree, plotted against the sequential number of each APM scan.

$17 < b_j < 20$

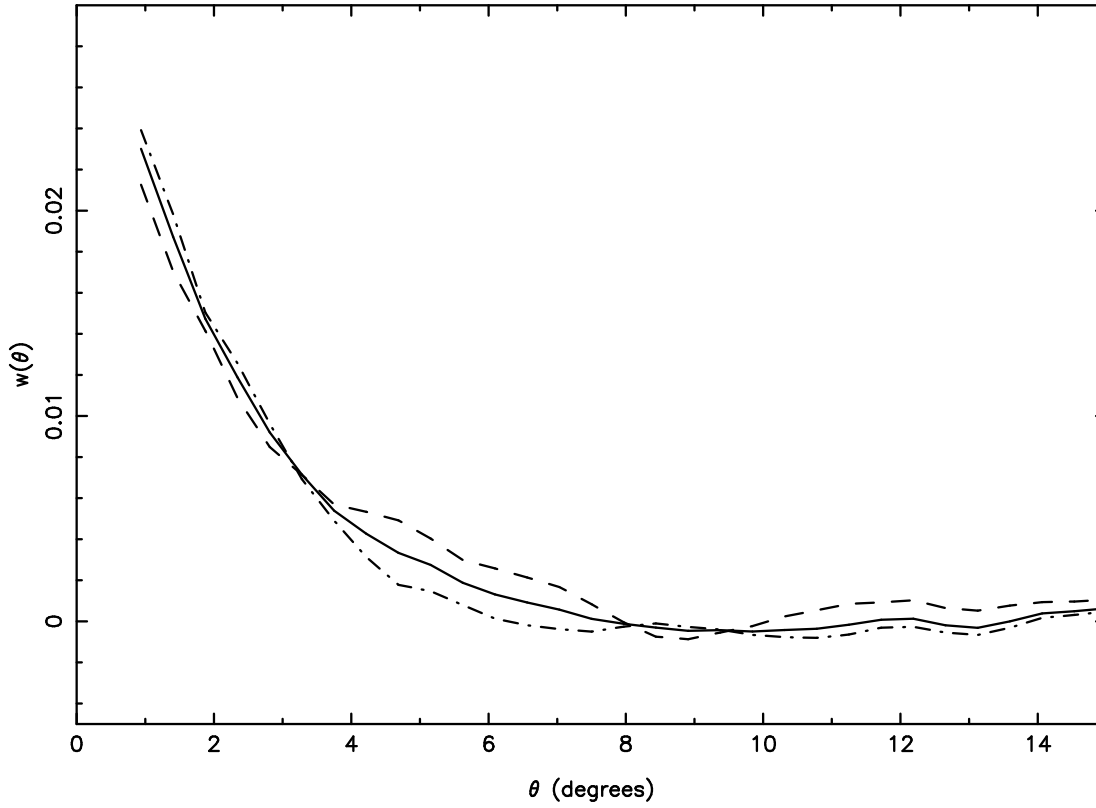


Figure 14. Inter-plate angular correlation functions for plate pairs scanned within 1 year of each other (dashed line) and scanned more than one year apart (dot-dashed line). The solid line shows the correlation function estimated from all galaxy pairs.

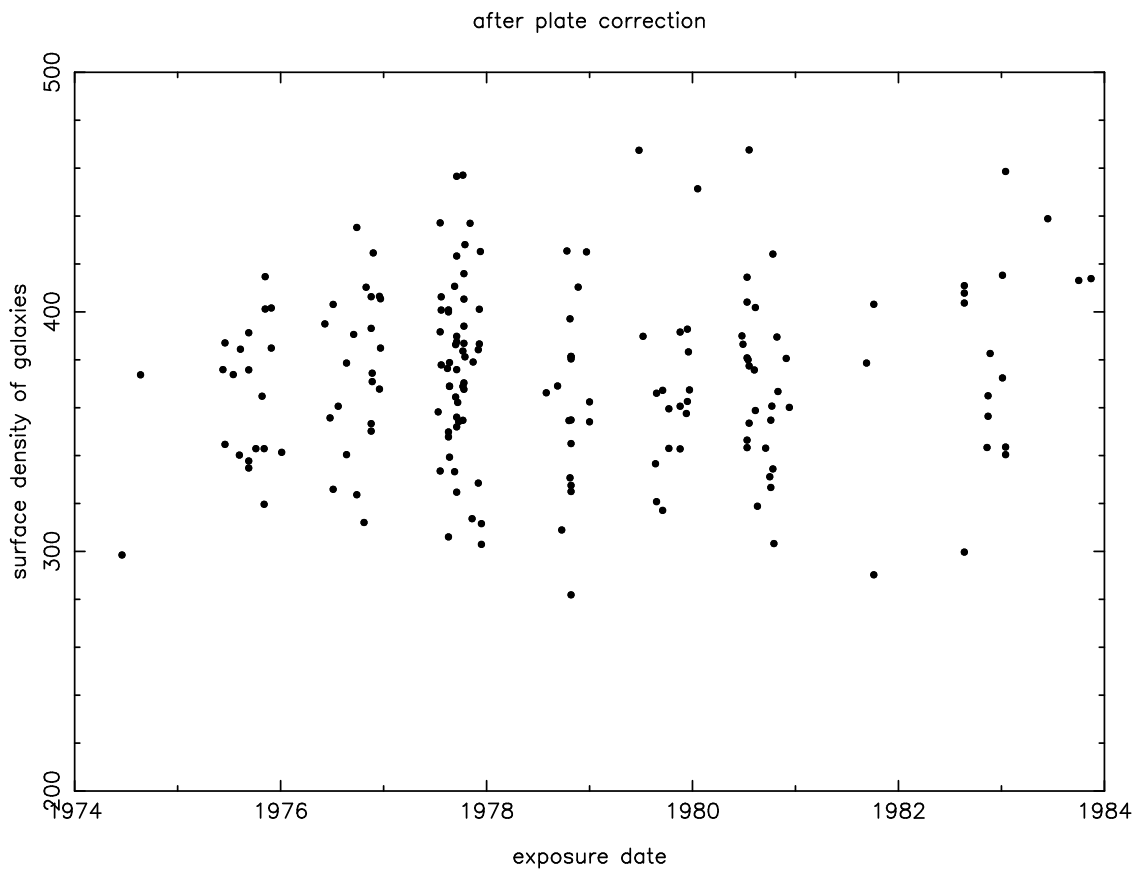


Figure 15. A scatter plot of the surface density of galaxies brighter than $b_J = 20.5$ on each plate in number per square degree plotted against the date of exposure of the Schmidt plate. No significant trends in the number of galaxies are seen.

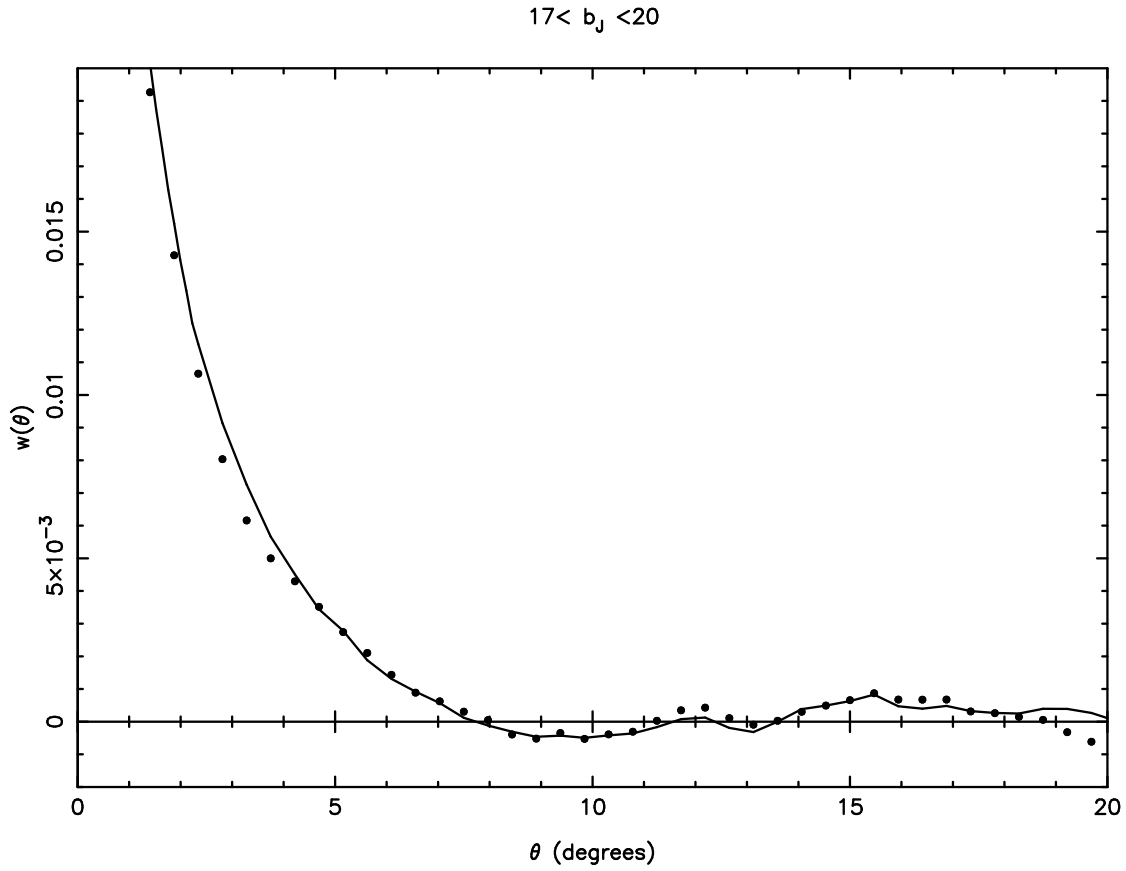


Figure 16. The points show the galaxy autocorrelation function for galaxies $17.5 < b_J < 20.0$ after correcting their magnitudes for the extinction estimated from the IRAS $100\mu m$ flux. The solid line shows the correlation function from the uncorrected map as plotted in Figure 2.

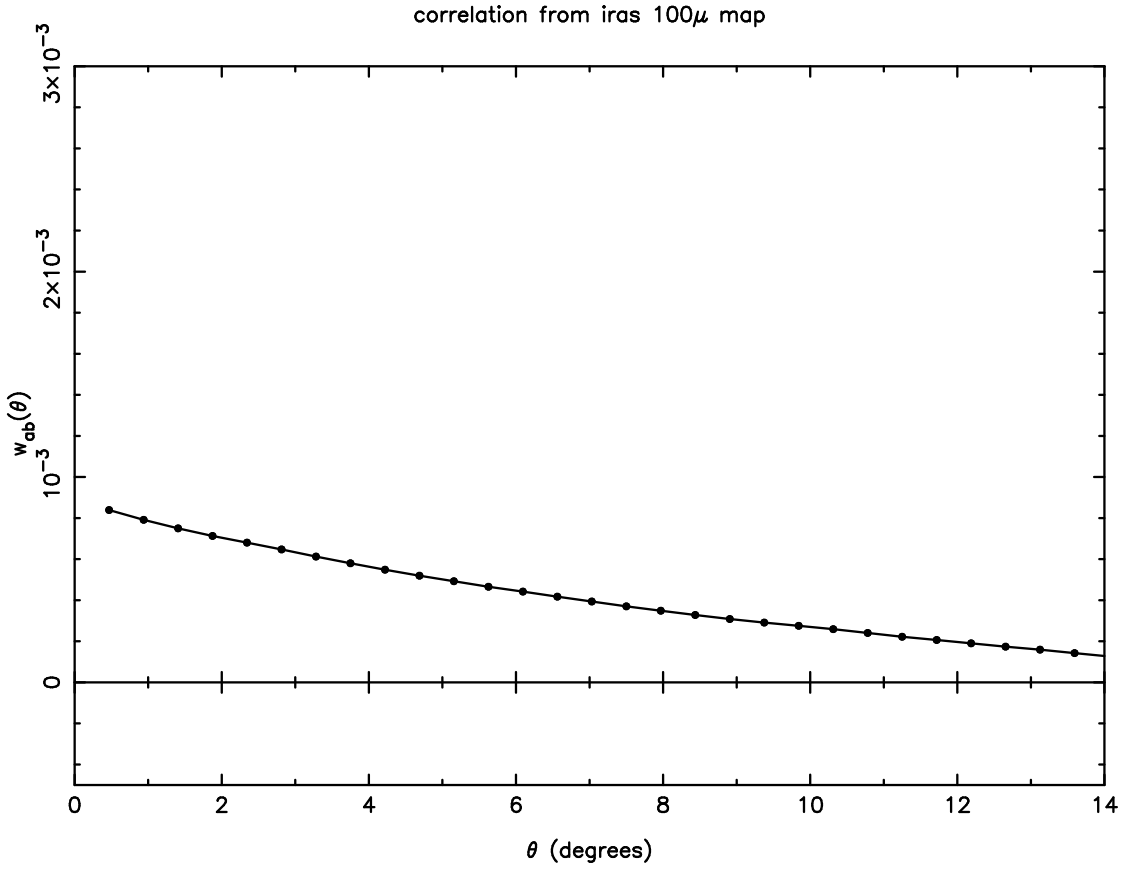


Figure 17. The covariance function of Galactic obscuration over the APM survey area as determined from IRAS maps of 100 μ m emission (see text for further details).

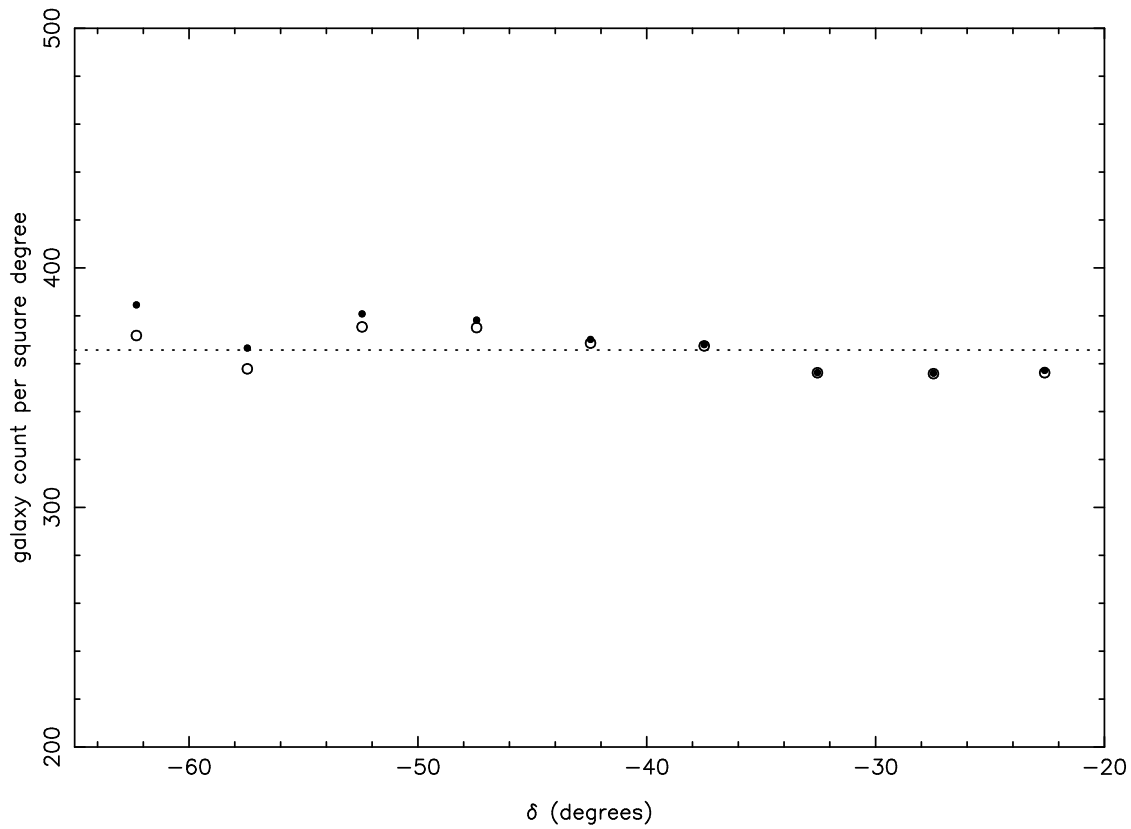


Figure 18. The mean galaxy surface density in the magnitude range $17 \leq b_J \leq 20$ plotted as a function of declination. The open symbols show the density before applying the correction for atmospheric extinction, and the filled symbols show the density after correction. The changes in density are smaller than the variations caused by real structure in the galaxy distribution. The dotted line shows the mean galaxy count averaged over the entire survey.

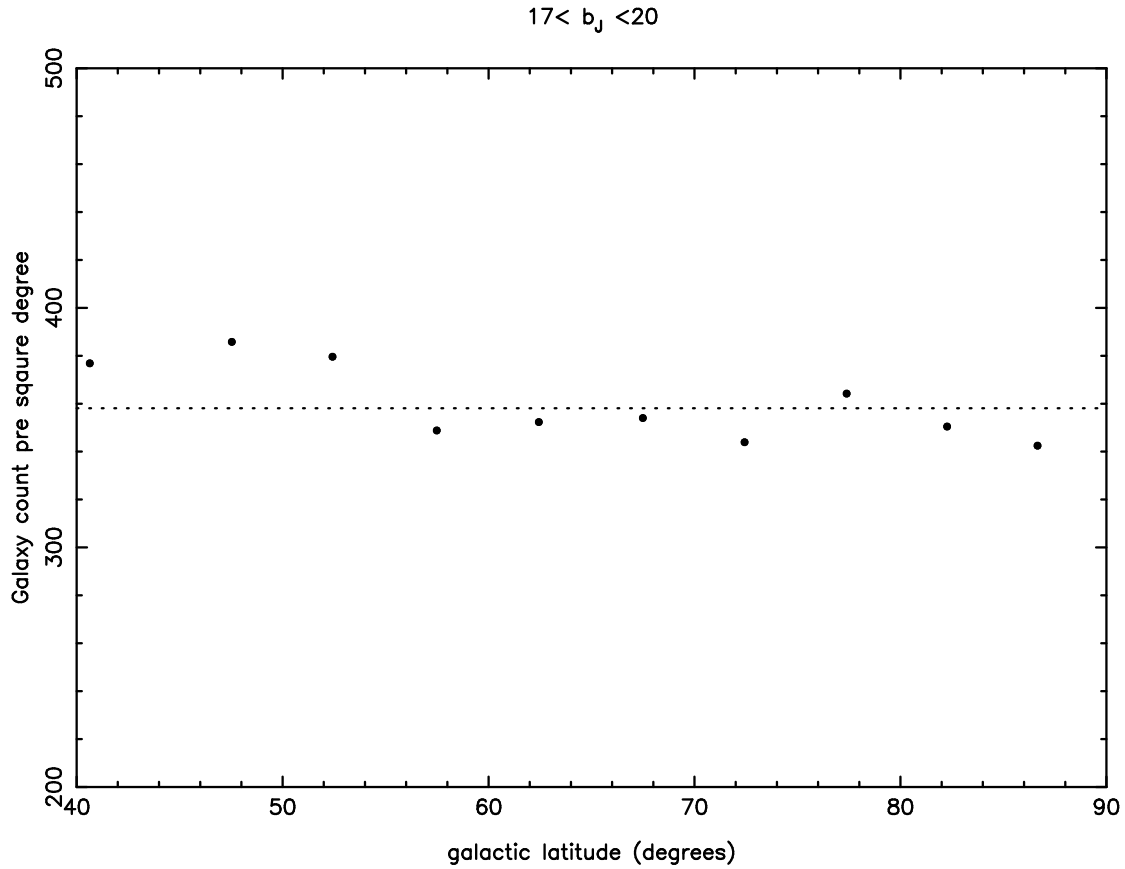


Figure 19. The mean surface density of images in the galaxy sample in the magnitude range $17 \leq b_J \leq 20$ plotted as a function of galactic latitude after correcting for galactic extinction. The dotted line shows the mean surface density. A small gradient can be seen, amounting to about 10% in density from the high to low latitude limits of the survey. This gradient arises because of the increase in the number of stellar blends at low latitudes that are misclassified as galaxies.

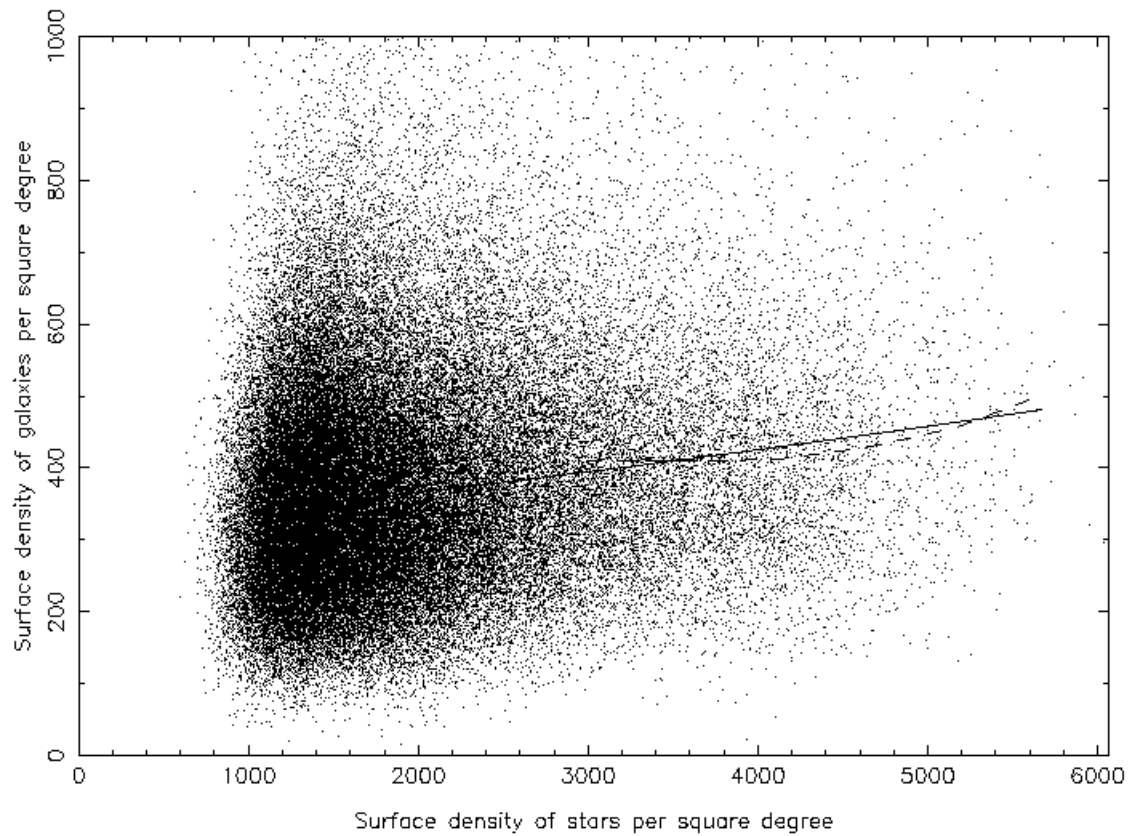


Figure 20. A scatter-plot of the surface density of galaxies with $20.0 > b_J > 17.0$ against the surface density of stars brighter than $b_J = 20.5$. A point has been plotted for each $0.23^\circ \times 0.23^\circ$ cell of equal area maps as described in Section 2.3. The dashed line shows the mean galaxy density binned as a function of the stellar density, and the solid line is the best fit quadratic.

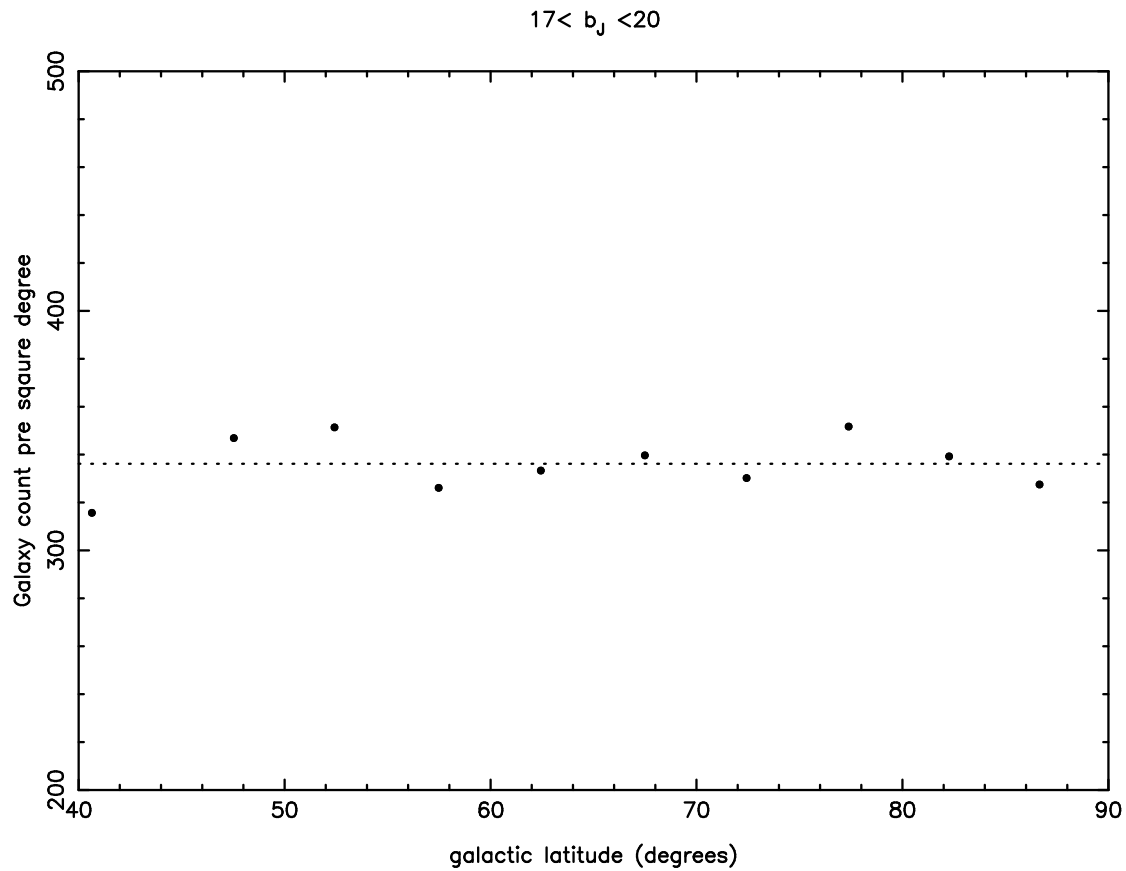


Figure 21. The mean surface density of galaxies as a function of galactic latitude after applying the correction for the variations in contaminating fraction of stellar blends. The dotted line shows the overall mean surface density. There is no significant gradient as a function of galactic latitude.

$17 < b_J < 20$

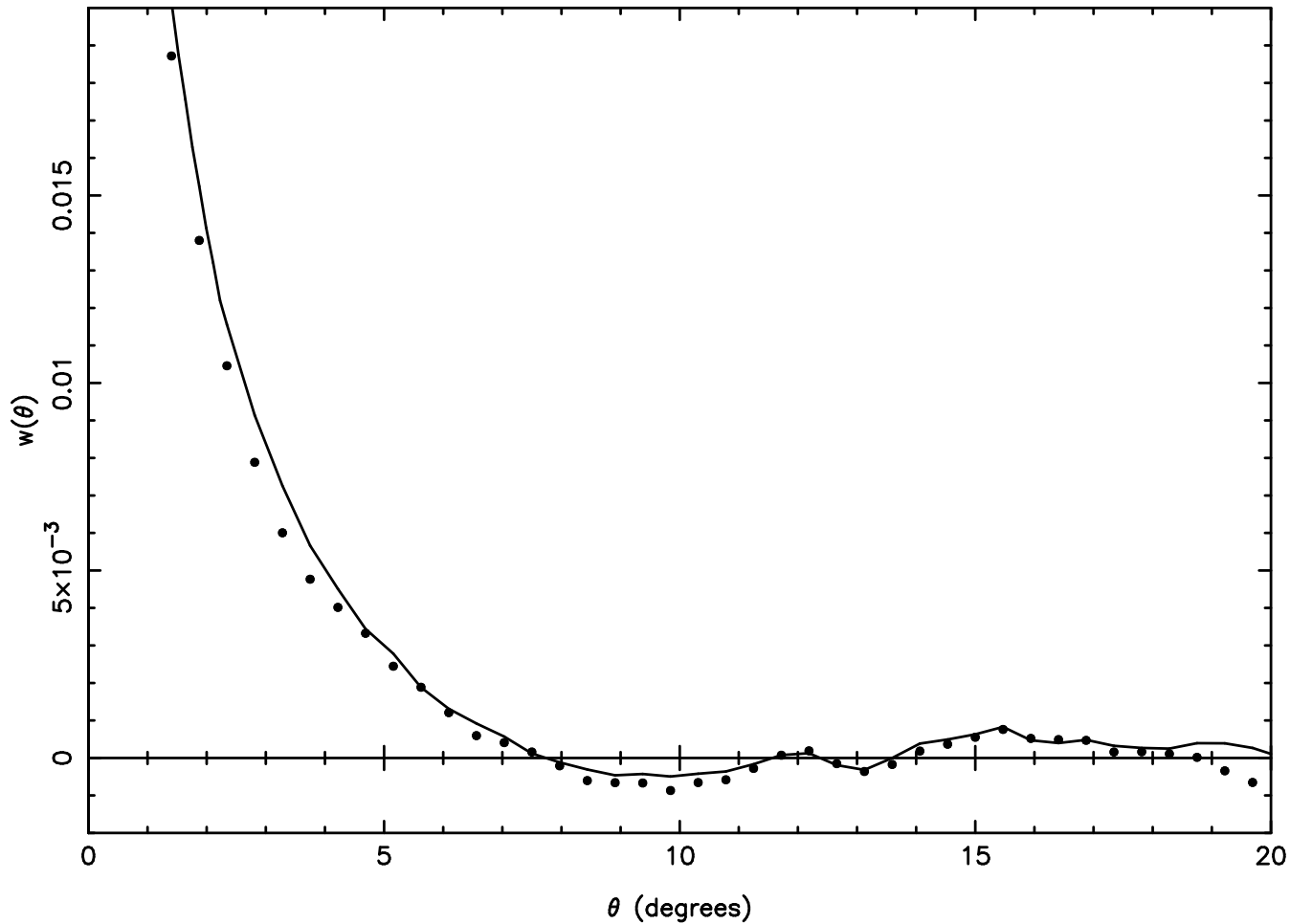


Figure 22. The solid points show $w(\theta)$ estimated from the fully corrected map of galaxies with $17 < b_J < 20$, including corrections for galactic obscuration, atmospheric extinction and variations in the fraction of contaminating images. The solid line is the estimate from the uncorrected galaxy map, as plotted in Figure 2. It can be seen that these corrections have a very small effect.

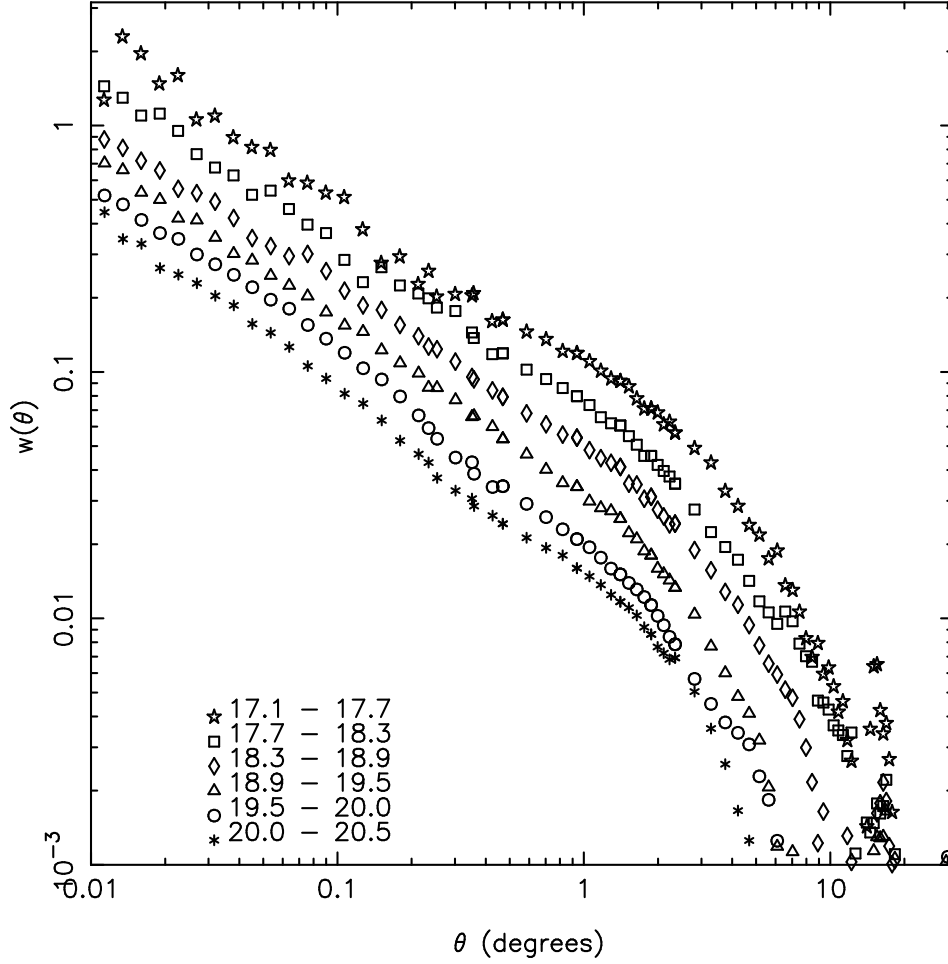


Figure 23. Estimates of $w(\theta)$ for six disjoint magnitude slices in the range $17 < b_J < 20.5$ as in Figure 3 except here we have corrected the estimated of $w(\theta)$ for the various systematic errors described in the text.

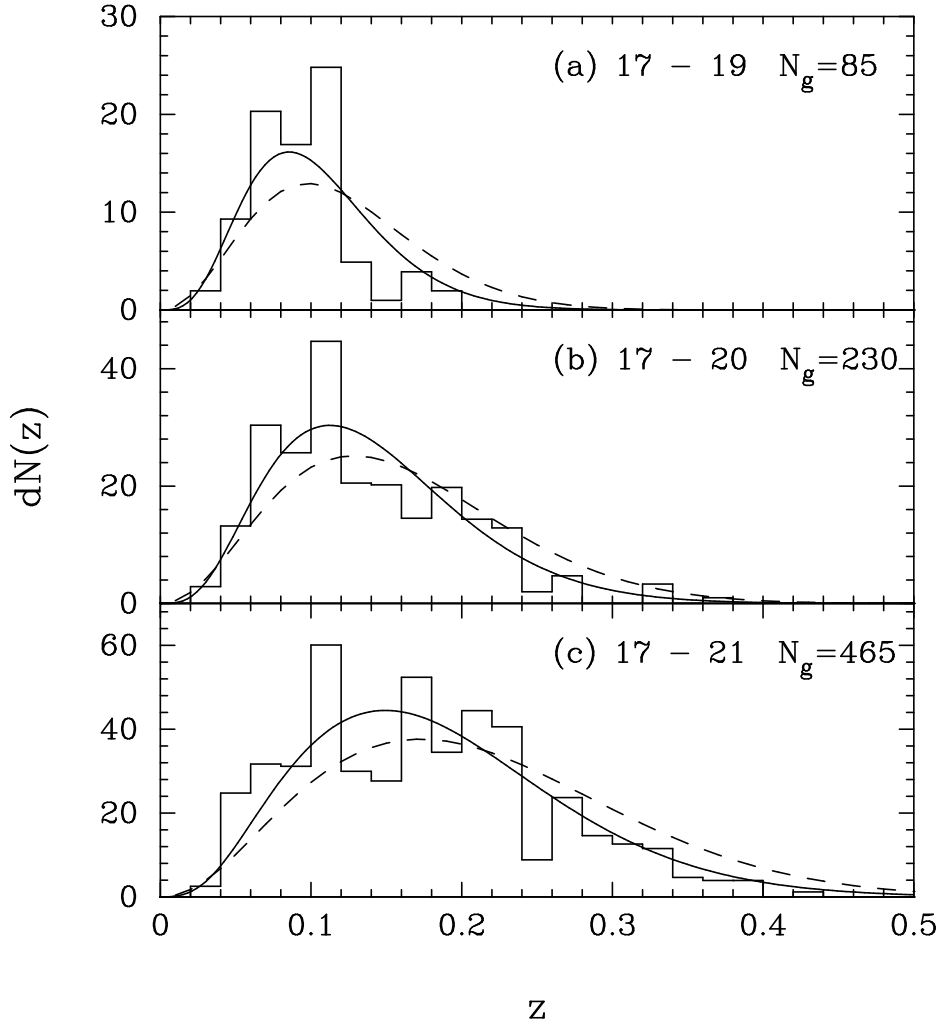


Figure 24. The redshift distributions in three magnitude slices determined from deep redshift surveys. The magnitude ranges and the number of galaxies, N_g , in each histogram are given in each panel. The solid lines show the redshift distributions derived from equations (38) and the dashed lines show the redshift distribution calculated from the model (equation 37) of Maddox *et al.* (1990c).

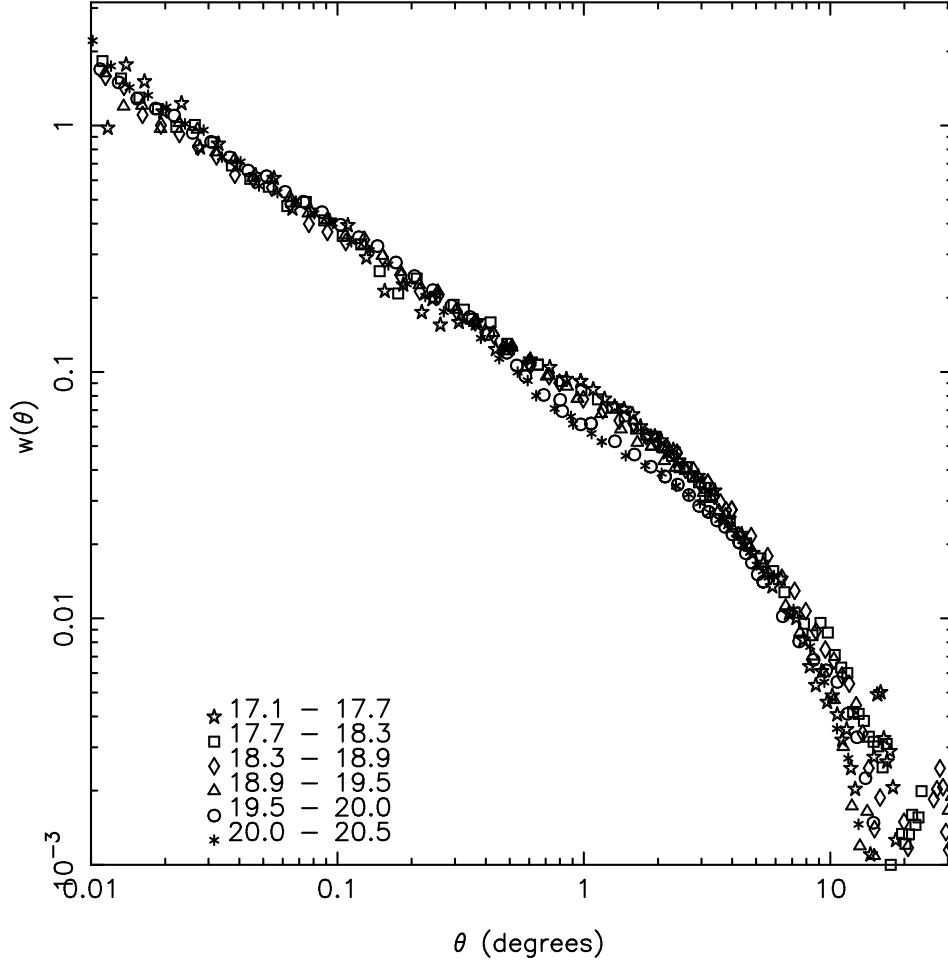


Figure 25. Corrected estimates of $w(\theta)$ for the six disjoint magnitude slices from Figure 23 scaled to a magnitude limit $b_J = 18.4$ (approximately the depth of the Lick catalogue) using the scaling factors given by equation 38 with $\epsilon = 0$ and $\Omega = 1$ (columns 4 and 5 of Table 5).

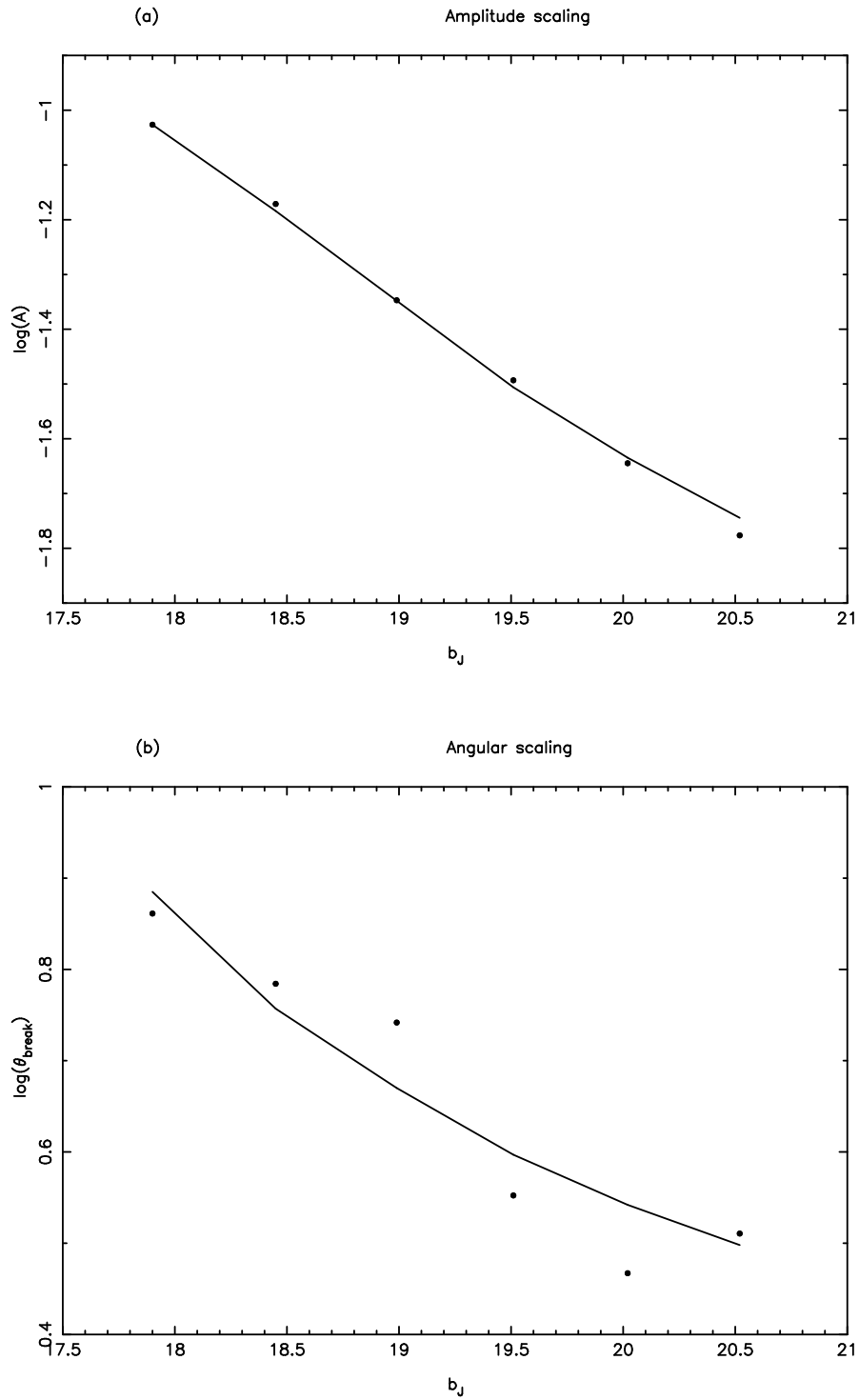


Figure 26. Figure (26a) shows the amplitude of $w(\theta)$ at $\theta = 1^\circ$ plotted as a function of magnitude limit for the six magnitude slices shown in Figure 23. The amplitude A was determined by least squares power law fits as described in the text. Figure (26b) shows the break angle θ_{break} , as defined in the text, plotted against magnitude limit for the six slices. The solid lines show the predictions of the scaling relation based on equation (38) with $\epsilon = 0$ and $\Omega_0 = 1$.

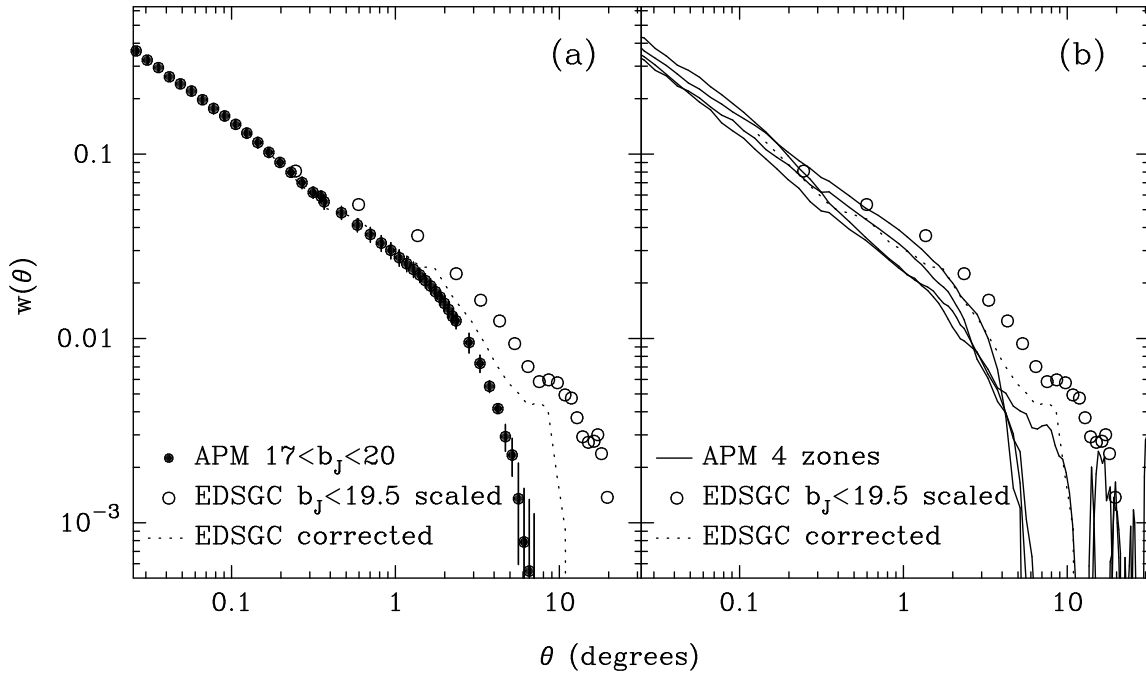


Figure 27. The solid points in Figure (27a) show the APM $w(\theta)$ with 1σ errors for the magnitude slice $17 \leq b_J \leq 20$, as plotted in Figure (2a). The open circles show $w(\theta)$ estimated from the EDSGC limited at $b_J = 19.5$ from Figure 2 of Collins *et al.* (1992) scaled to the APM results as described in the text. The dotted lines show the corrected EDSGC $w(\theta)$ from Figure 7 of Nichol and Collins (1993) scaled to the APM results. In Figure (27b) we plot separately the $w(\theta)$ estimates for the four zones of the APM Survey, each of which has about the same area as the EDSGC.

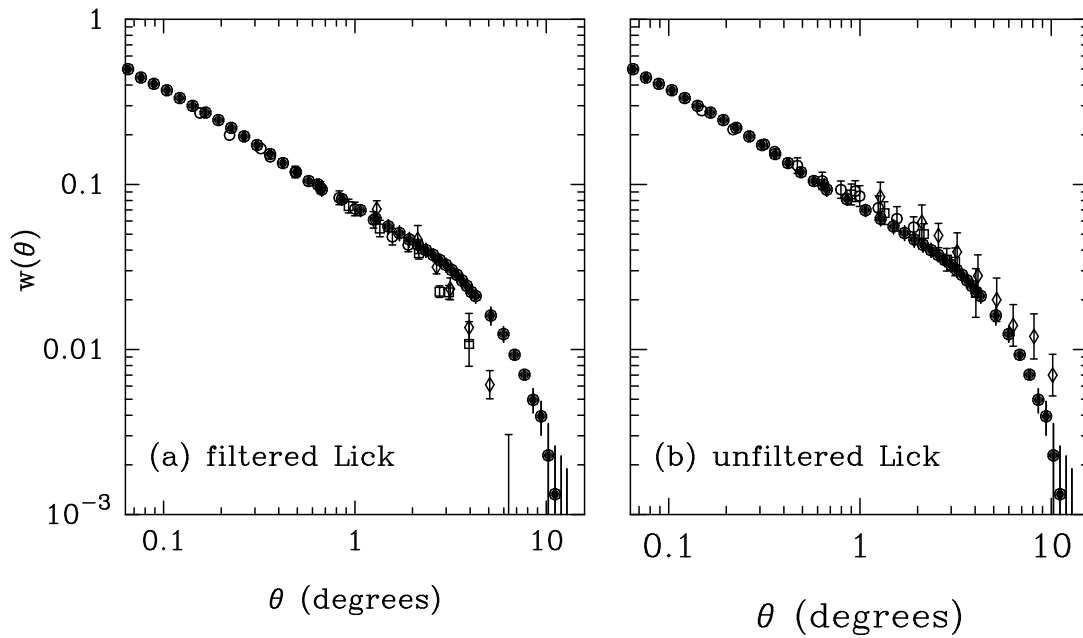


Figure 28. Estimates of $w(\theta)$ (solid points) for APM galaxies in the magnitude slice $17 < b_J < 20$ scaled to the depth of the Lick Survey. The open symbols show the GP77 estimates of $w(\theta)$ for the Lick survey after filtering the Lick counts (Figure 28a) and before filtering (Figure 28b).

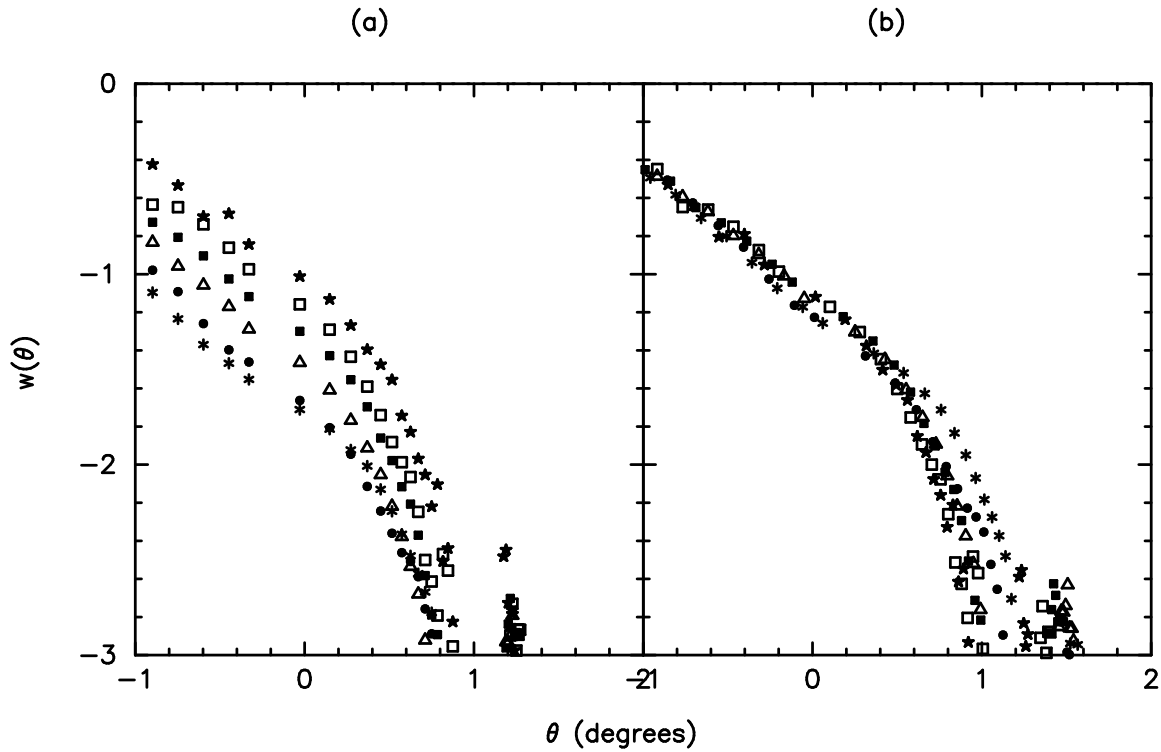


Figure 29. The effect on $w(\theta)$ of filtering the APM maps. For each magnitude slice (shown with the same symbols as in Figures 3 and 23) we fitted a bi-cubic spline to the map of galaxy density and then multiplied by the inverse of the fit before calculating the plotted $w(\theta)$. Figure (29a) shows the angular correlations of the six magnitude slices after filtering. For the brighter slices, the break in $w(\theta)$ is dramatically steepened compared to the unfiltered results plotted in Figure (23). The measurements for the fainter slices are hardly changed by the filtering. Figure (29b) shows the scaling test applied to the filtered estimates of $w(\theta)$, as in Figure 25.

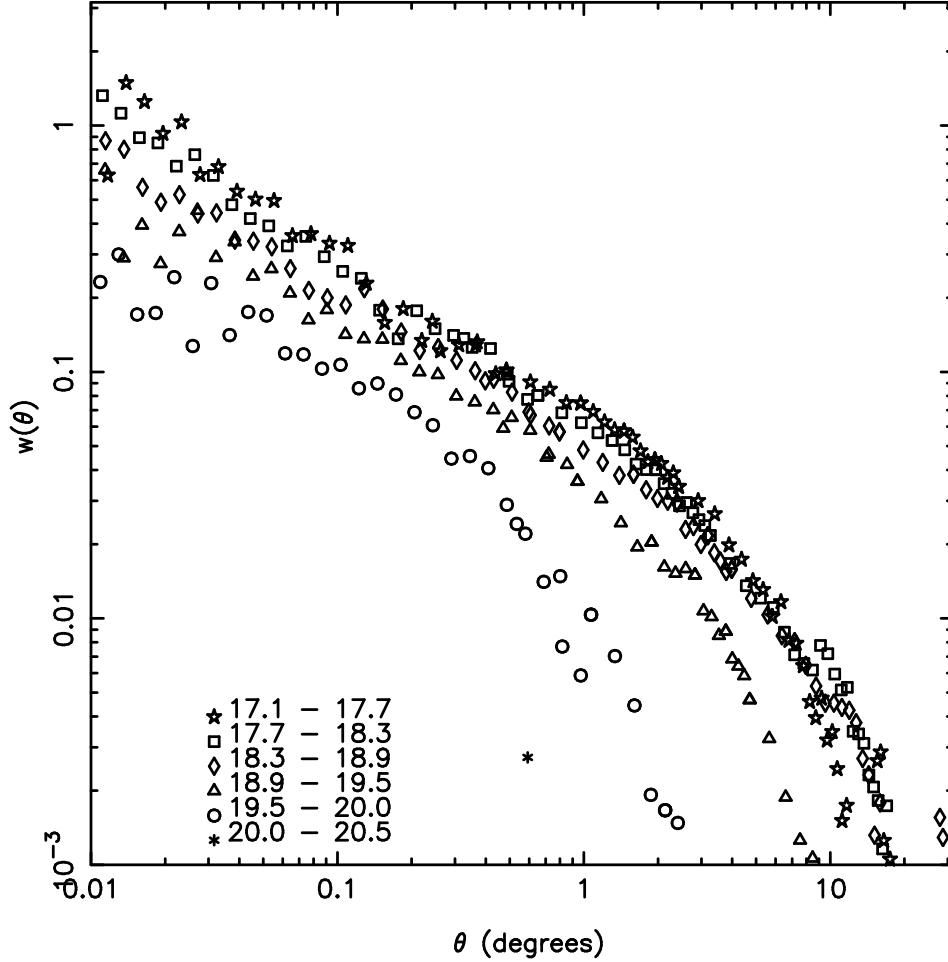


Figure 30. The correlation functions from the five brighter slices after subtracting the correlation function of the faintest slice. The correlation functions have been scaled to a common depth as in Figure 25. This correction provides a gross overestimate of the errors in $w(\theta)$ since it requires that *all* of the observed correlations of the faint galaxies are produced by systematic errors. However, even in this extreme case, the scaled estimates of $w(\theta)$ for the brightest three slices are in reasonable agreement, showing significant clustering between scaled angles of 5° and 10° .

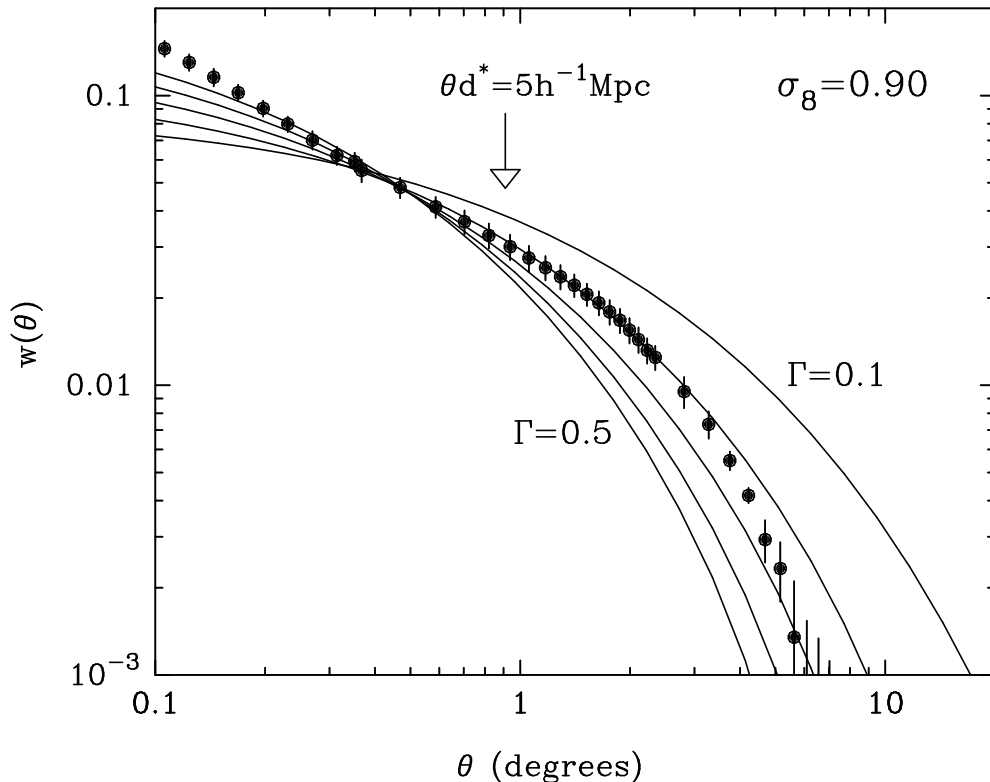


Figure 31. The APM $w(\theta)$ estimates for the magnitude slice $17 < b_J < 20$ compared with the predictions of a family of CDM-like models. The theoretical predictions are computed from the linear theory power spectrum (equation 40), where the parameter $\Gamma = \Omega_0 h$. The power spectra have been normalized so that the *rms* fluctuations in spheres of radius $8 h^{-1} \text{Mpc}$ is $\sigma_8 = 0.9$. We plot curves for $\Gamma = 0.1, 0.2, 0.3, 0.4$ and 0.5 (from top to bottom). The arrow marks the angular scale corresponding to a physical separation of $\approx 5 h^{-1} \text{Mpc}$ at the median depth of the survey.

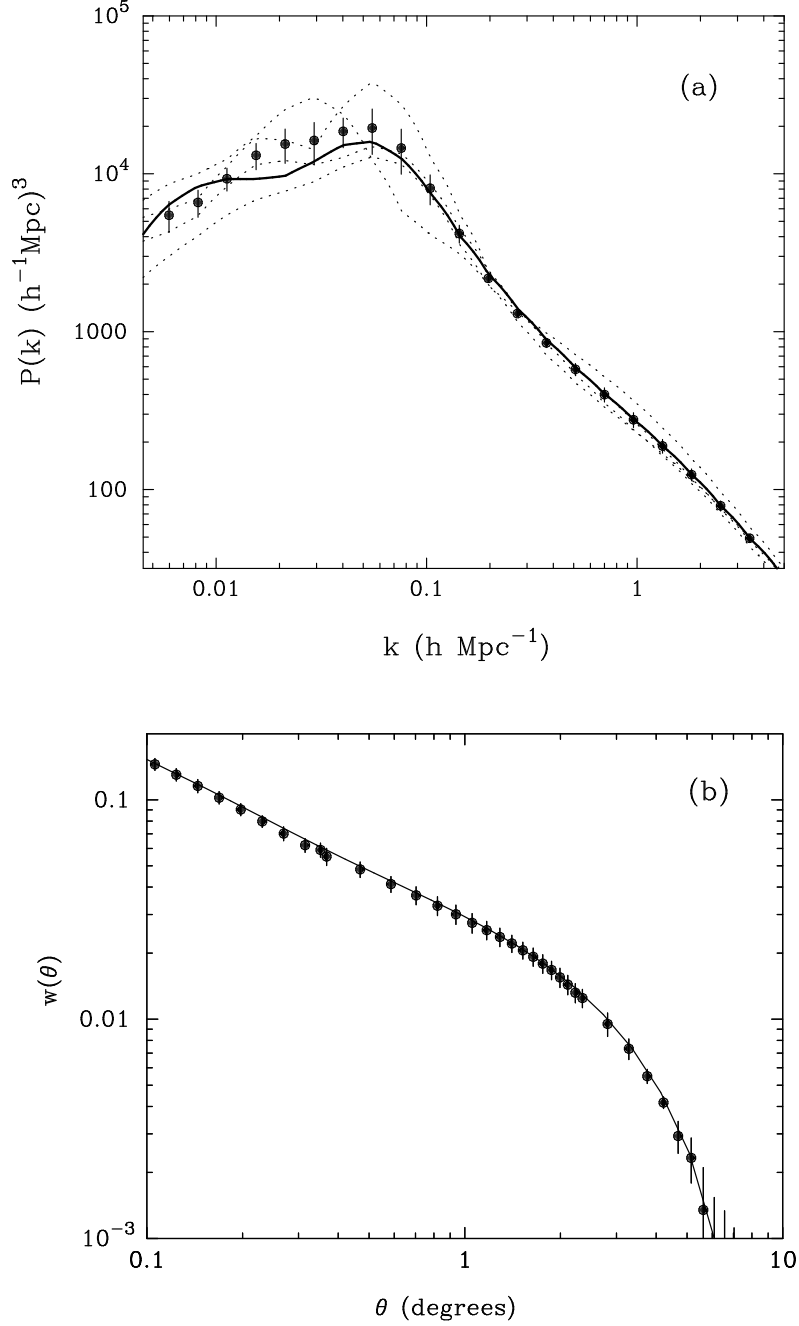


Figure 32. Figure 32a shows the three-dimensional power spectrum derived by inverting the APM angular correlation function as described in the text. The dotted lines show the inversion of $P(k)$ for 4 nearly equal area zones. The filled circles show the means of these estimates together with 1σ error bars. The thick solid line shows the power spectrum by inverting $w(\theta)$ estimated from the full survey area. Figure 32b shows a check of the inversion. The solid line is computed from equation (42a) using the power spectrum plotted as the thick solid line in Figure 32a and reproduces the angular correlation function (shown by the filled symbols) used in the inversion.

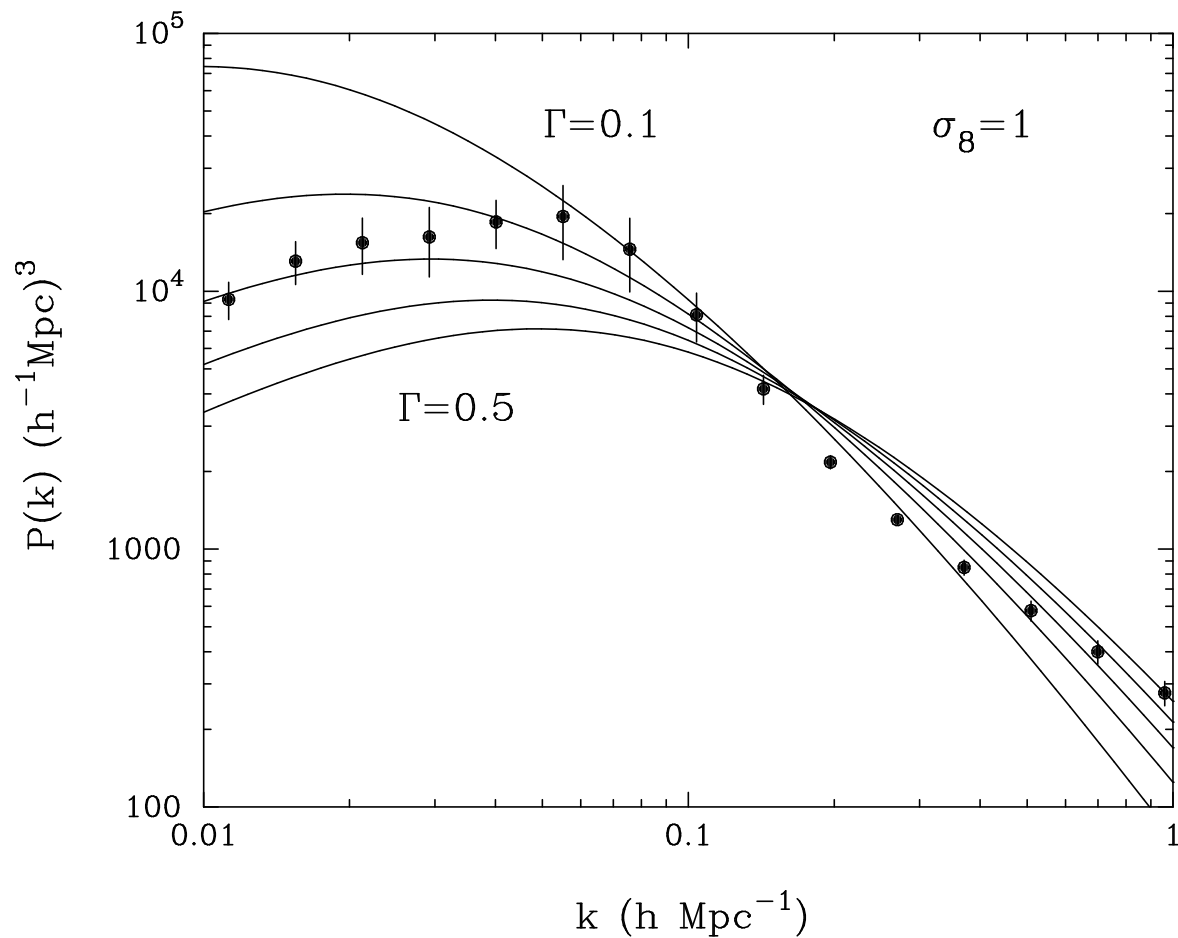


Figure 33. The points show the three-dimensional power spectrum from the APM survey together with 1σ errors, as in Figure 32. The curves show the family of linear theory CDM power spectra (equation 40) with $\Gamma = 0.1, 0.2, 0.3, 0.4$ and 0.5 from top to bottom. The CDM power spectra have been normalized to $\sigma_8 = 1$.

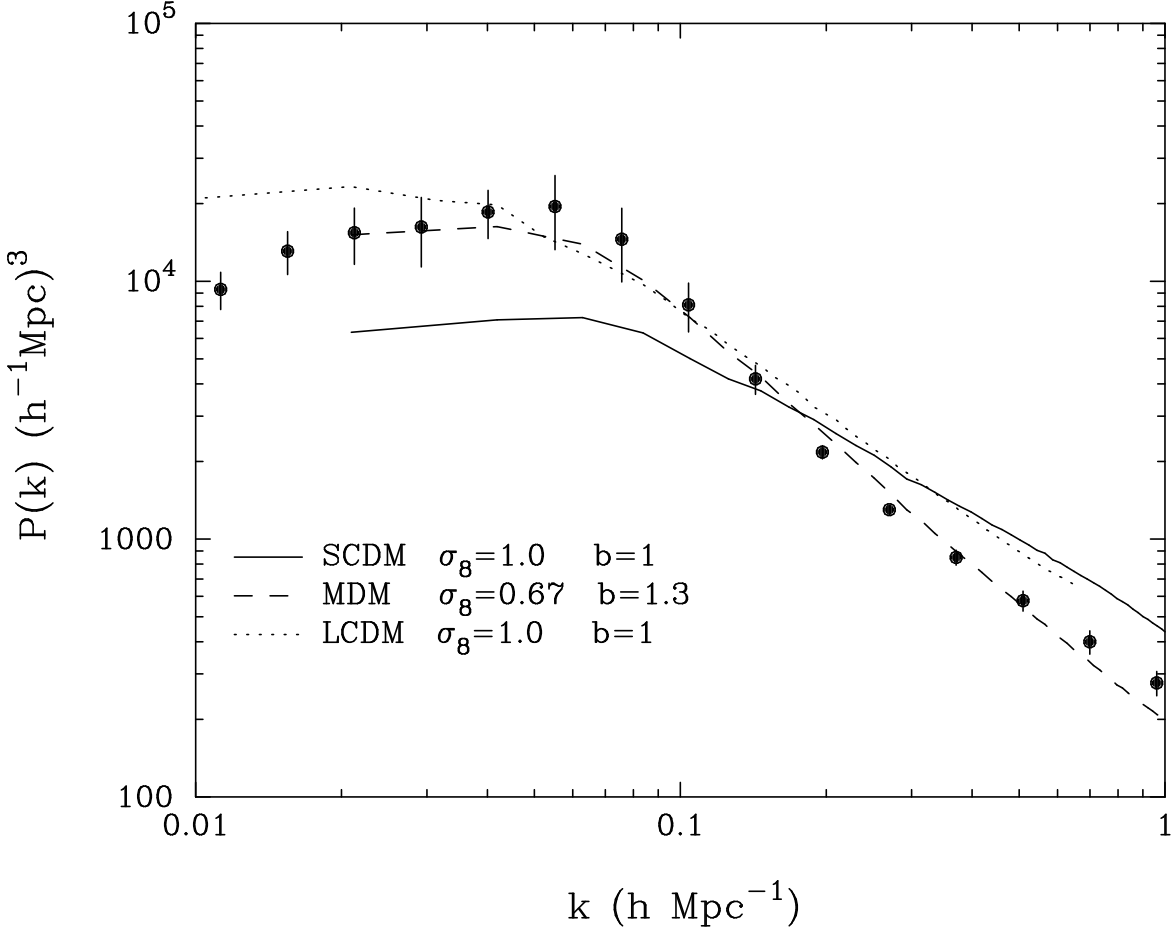


Figure 34. The APM power spectrum compared with the power spectra determined from N-body simulations as described in the text. The simulations are normalized to match approximately the amplitude of the microwave background anistropies detected by COBE; the values of σ_8 for the mass fluctuations in each model are given in the figure. The curves show the power spectra of the mass fluctuations; for the MDM model we have multiplied the power spectrum by a biasing factor b^2 , with $b = 1.3$, to match the observations.

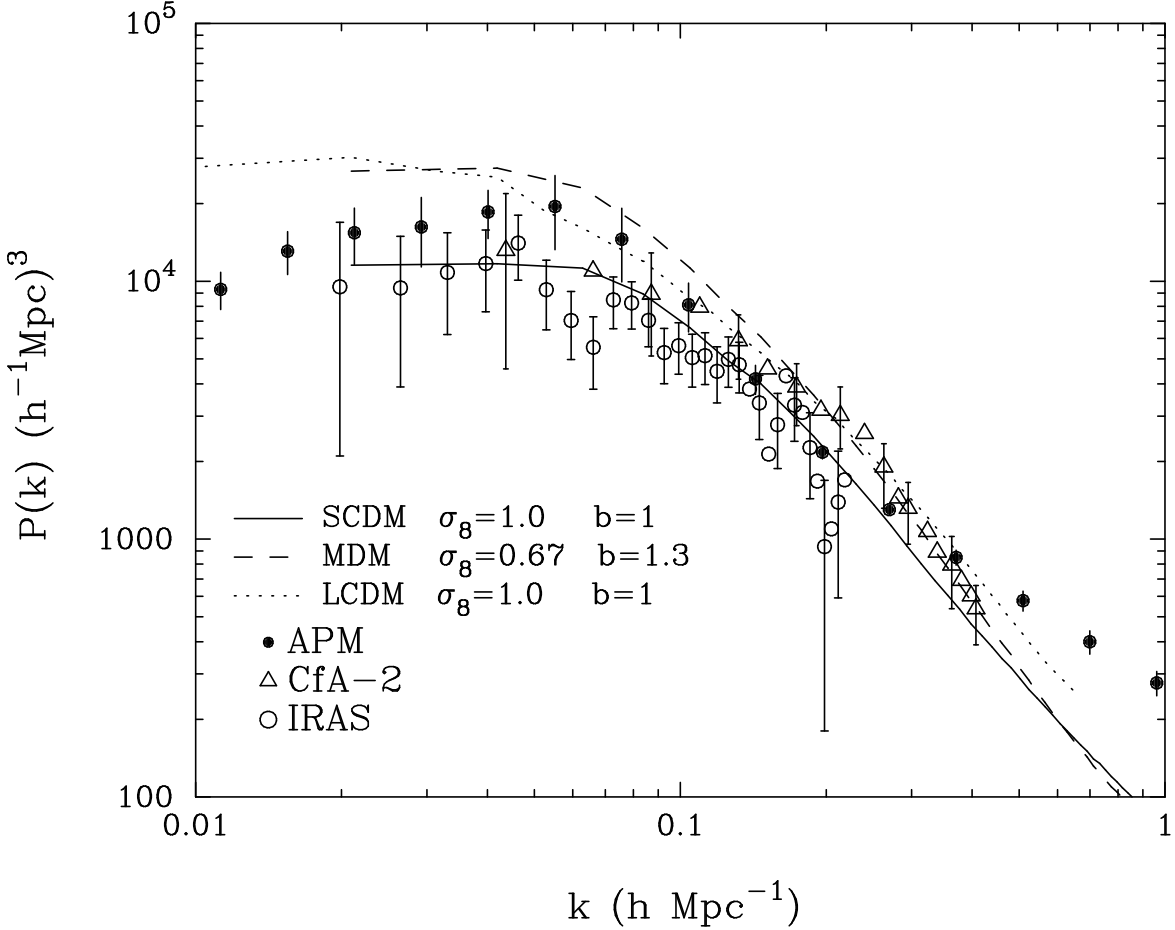


Figure 35. The APM power spectrum compared with the power spectra determined from redshift surveys. The open circles shows the power spectrum of IRAS galaxies, as determined by Tadros & Efstathiou (1995a). The open triangles show the power spectrum of optically selected galaxies determined by Park *et al.* (1994) from a volume limited subset of the CfA-2 survey (see text for details). The error bars on the points show 1σ errors. The curves show the power spectra of the N-body simulations of Figure 33 determined *in redshift space*.

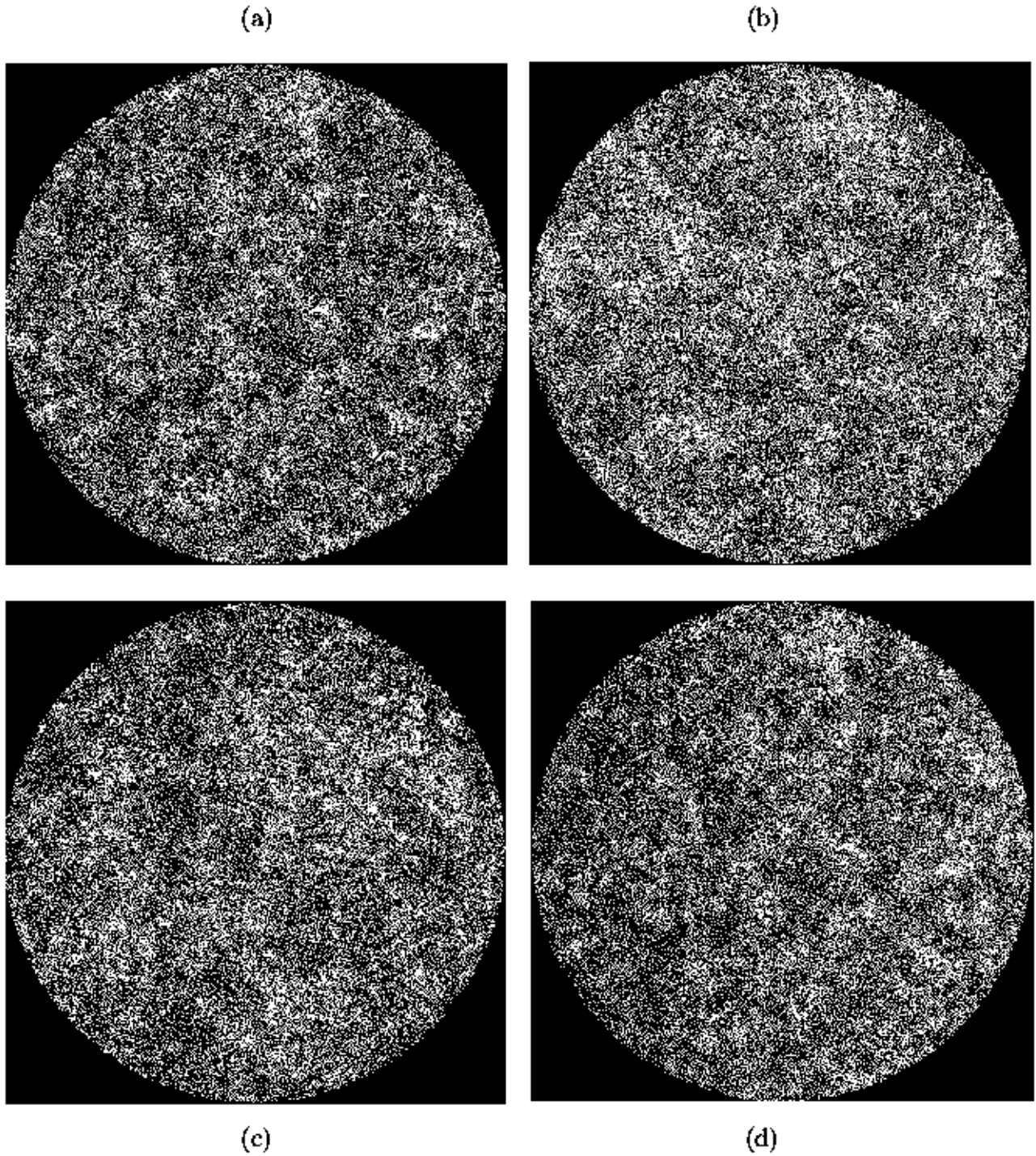


Figure A1. Greyscale maps showing the galaxy density in a variety of simulated galaxy catalogues constructed using the Soneira-Peebles prescription. The simulated cones are 60° in diameter. (a) SP0; (b) SP2; (c) SP4; (d) SPS. Details of the model parameters are given in the text.

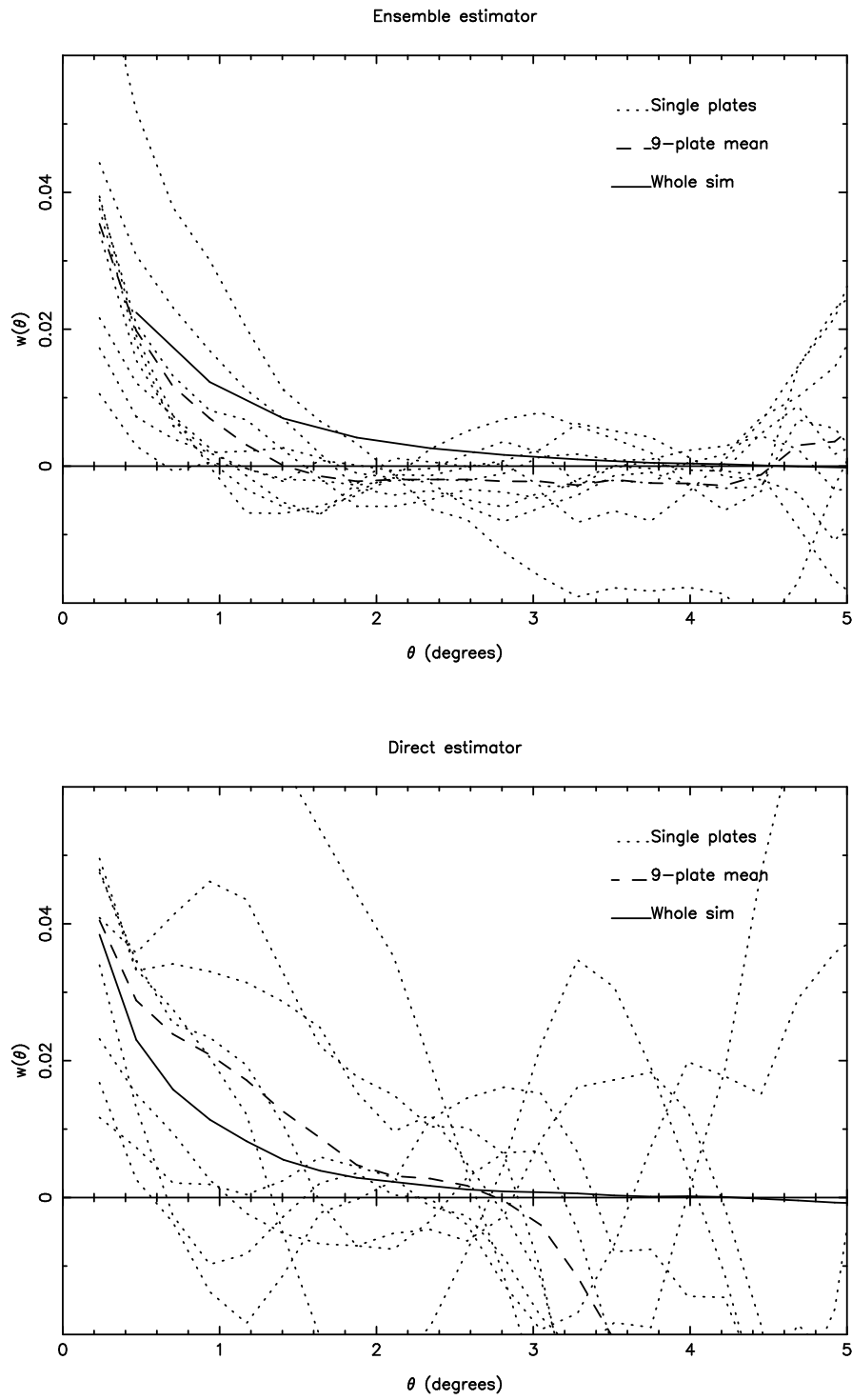


Figure A2. “Single plate estimates” from the SP2 simulations (a) using the ensemble estimator; (b) using the direct estimator.

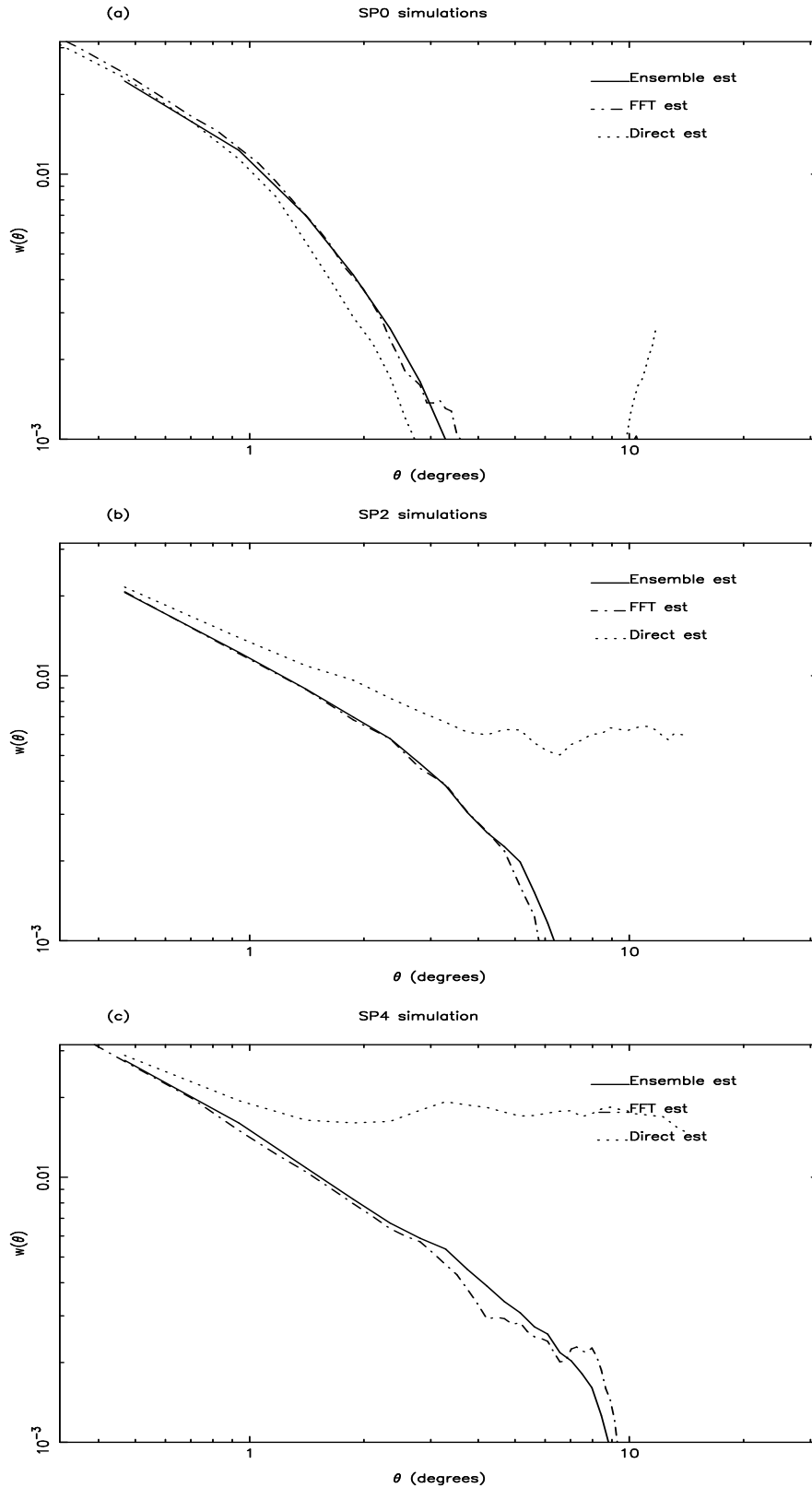


Figure A3. Measurements of $w(\theta)$ using the ensemble estimator, the FFT estimator and the direct estimator for three different types of models (a) SP0; (b) SP2; and (c) SP4. Details of the models are given in the text.

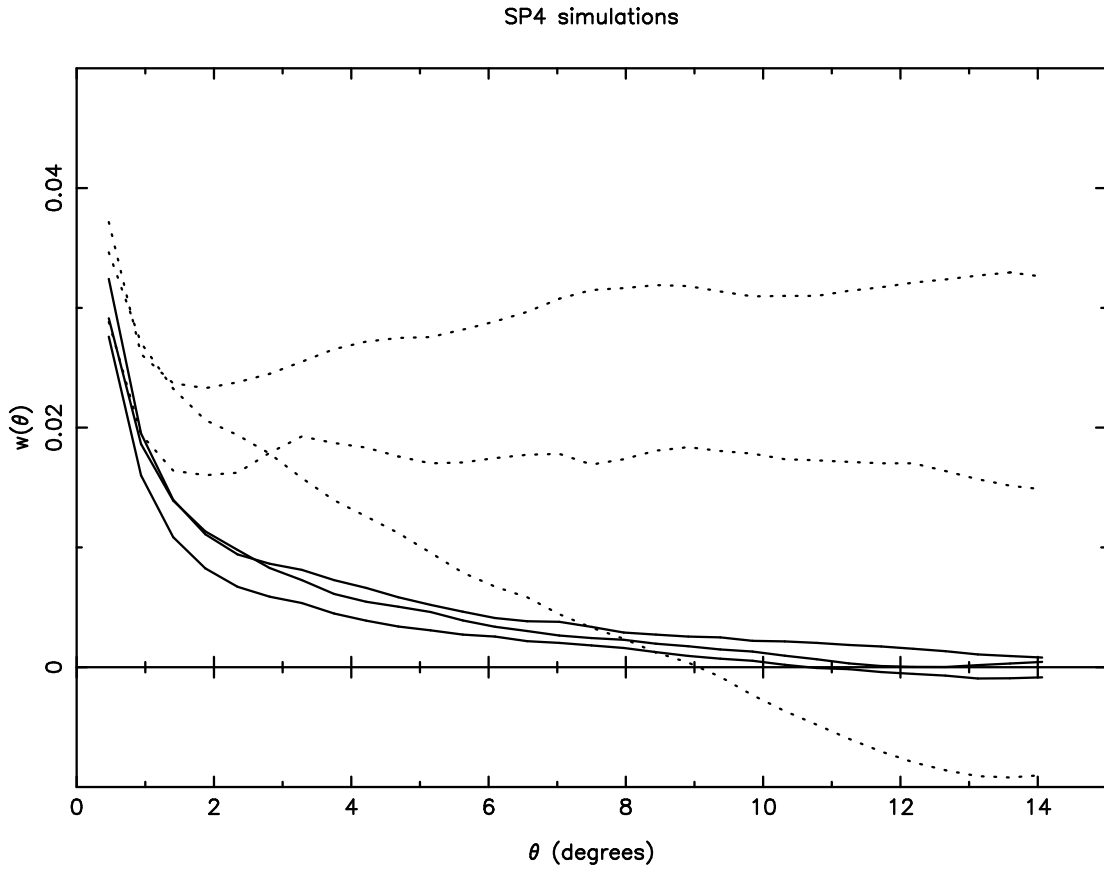


Figure A4. Measurements of $w(\theta)$ from three different SP4 realizations using the direct estimator (dotted lines) and the ensemble estimator (solid lines).

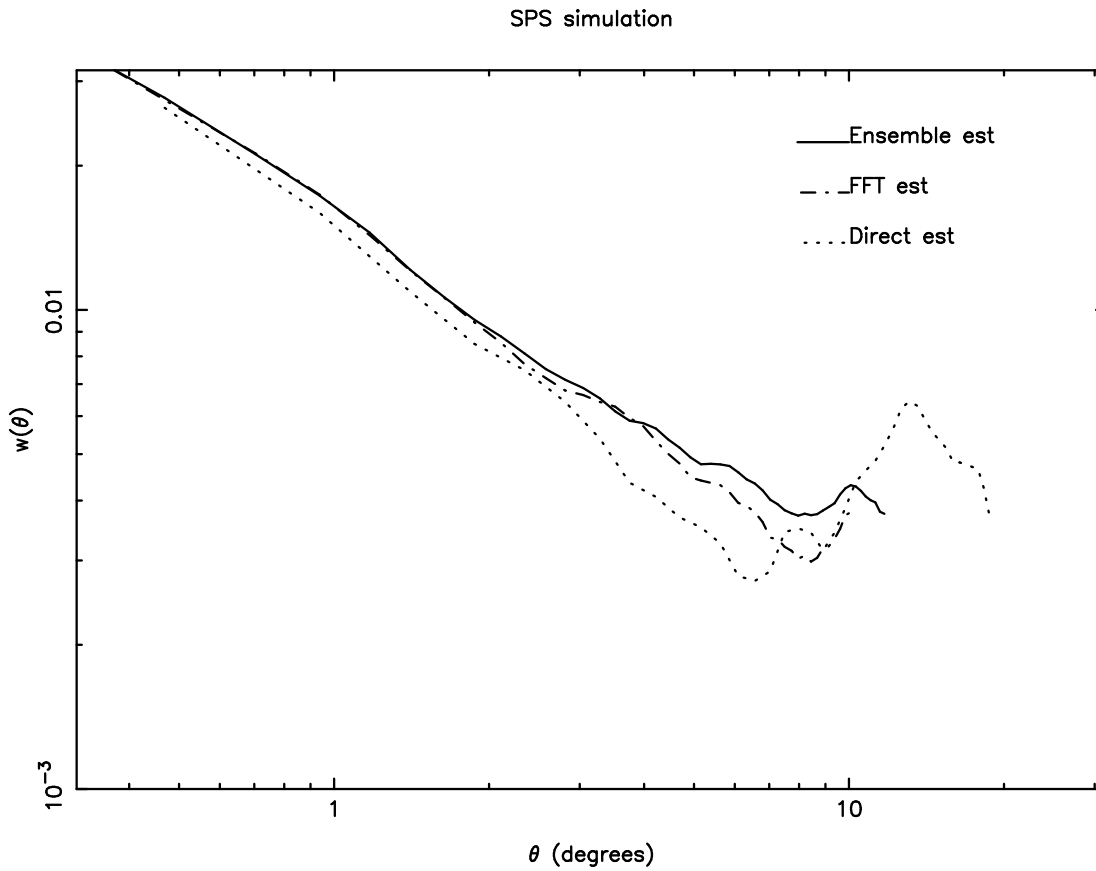


Figure A5. The results of using different estimators for simulations including a linear gradient. The lines show the direct, ensemble, and FFT estimates of $w(\theta)$ from an SPS simulation, as described in the text.

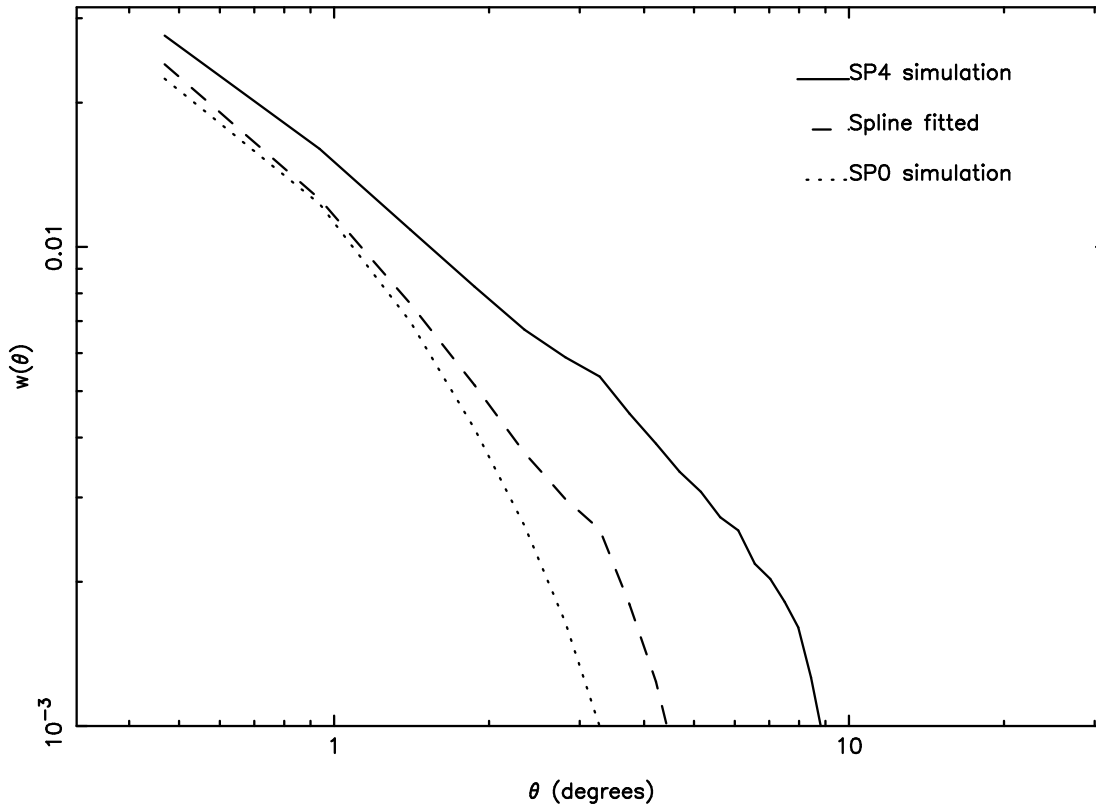


Figure A6. The effects of removing large-scale structure using spline fits. The solid line shows $w(\theta)$ from the SP4 simulation. The dashed line shows $w(\theta)$ from the same simulation after subtracting a bicubic spline fitted to the original simulation. For comparison the dotted line shows $w(\theta)$ for an SP0 simulation.